Current systems associated with Non-Conjugate Aurora

Master Thesis in Space Physics
by
Theresa Rexer

January 20, 2015

Birkeland Center for Space Science
University of Bergen
Norway

Abstract

The main goal of this Thesis is twofold. First, we want to develop a solid method for identifying the field aligned currents related to the specific non-conjugate auroral features identified by *Reistad et al.* [2013] and *Laundal et al.* [2010]. Secondly, by utilizing this method we explore the idea that the non-conjugate aurora can be explained by asymmetries in the field aligned current system in the two hemispheres *Østgaard and Laundal* [2012]. By transforming ground magnetometer measurements from the SuperMAG network in both hemispheres to the coordinate system used by the VIS Earth and WIC cameras on board the Polar and IMAGE satellites, we combine the two datasets. We present four non-conjugate auroral events were a current system associated with the observed aurora and the ground magnetometer measurements can be postulated. For one out of four events we can identify signatures attributed to asymmetric field aligned currents. Three factors stand out as important for the identification of these; the position of the ground magnetometer station in relation to the non-conjugate auroral feature, the spatial extension of the feature, and its intensity compared to surrounding auroral features.

Acknowledgments

I would like to thank my supervisor Nikolai Østgaard for proposing this interesting master project. I am grateful for your guidance and constructive feedback encouraging me to further work. I would also like to thank Jone Peter Reistad for the discussions and great support. Your interest in my work and help has been invaluable and is much appreciated. I thank Karl Magnus Laundal for providing the plotting software for the conjugate images and helping me with the development of the method used in this thesis. My thanks also goes to the rest of the space physics group for making the last year such a good experience. A warm thank you goes to Linn, Marit, Paul and my fellow master students. Your many contributions and friendship have made this a wonderful time I will remember. Thank you, Inga for making proofreading fun. I also want thank my friends Synne and Roger for your patience and encouragement when needed. And also for keeping Hurley company on all those long days. A special thank you goes to Knut Ola and Hurley. I wish to thank all of my wonderful family, especially Jan, Andrea, Mario and Claudia.

For the ground magnetometer data I gratefully acknowledge SuperMAG and all collaborators. I thank S. Mende and the IMAGE FUV team for providing the IMAGE FUV data and J. Sigwarth for providing the Polar VIS Earth data. Also, I thank ACE MAG and SWEPAM teams for IMF and solar wind data and the Space Physics Data Facility CDAWeb for providing the *AE* and *Sym-H* index data.

Theresa Rexer
Bergen, January 2015

Contents

1 Introduction

The Aurora observed in the northern and southern high latitude regions is a striking visible phenomenon related to the coupling of our Earth's atmosphere and space. Plasma from the Sun, enters the Earth's magnetosphere and precipitates down into the ionosphere along the Earth's magnetic field lines. At the footpoint of the magnetic field lines, the plasma collides with particles in the atmosphere as the density increases, and excites the atmospheric species. Auroral lights are produced when the excess energy is released. The aurora can be observed in an oval shaped region fixed in space relative to the Sun and the magnetic poles in the southern and northern hemisphere.

The coupling of the aurora to charged particles originating from the Sun was first suggested by *Kristian Birkeland* in 1908. He proposed horizontal currents coupled to a field aligned current systems flowing in and out of the upper polar atmosphere along the Earth's magnetic field *Birkeland* [1908]. His original figure of the current system associated to aurora is shown in the picture below. However, such a three-

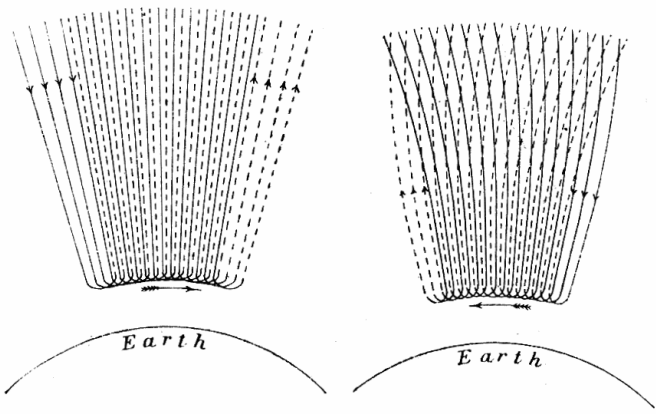

Birkeland's original figure of the current systems related to aurora.

dimensional current system is impossible to determine with ground measurements alone [*Chapman*, 1935; *Fukushima*, 1976] and consequently is was not verified until the first satellite measurements could be made of the field aligned currents [*Zmuda and Armstrong*, 1974a; *Zmuda et al.*, 1967]. Since then, these current systems have been the subject of numerous studies as they play an important role in the coupling of the ionosphere and magnetosphere.

Much of our understanding of the auroral electrodynamics and the coupling to the magnetosphere and space is based on observations from the northern hemisphere only. The assumption was made that the aurora in the southern hemisphere is a mirror image of the aurora in the northern hemisphere. Through simultaneous conjugate imaging of the aurora in both hemispheres, both ground based and airborne, this has changed. Observations have shown that asymmetries in location and intensity exist.Recently, a number of non-conjugate aurora events have been identified from simultaneous imaging of the polar hemispheres by the Polar and IMAGE satellite [*Laundal and Østgaard*, 2009; *Reistad et al.*, 2013]. Based on previous studies *Østgaard and Laundal* [2012] suggested that the auroral asymmetries in the two hemispheres can be related to asymmetric currents. This Thesis aims to further explore this idea by investigating the current systems associated with different auroral displays in the two hemispheres.

Ground based magnetometers have been utilized for the investigation of the currents coupling the ionosphere and magnetosphere for decades. The perturbations measured on the ground of the Earth's magnetic field are related to ionospheric, field aligned and magnetospheric currents as well as currents induced within the Earth. The SuperMAG network combines measurements from more than 400 ground magnetometers world wide and provides these in a unified coordinate system, making it a valuable tool for global studies.

In this Thesis we utilize simultaneous satellite observations of the entire auroral oval in the two hemispheres provided by the IMAGE WIC and Polar VIS Earth cameras. We combine these with measurements of the perturbation to the Earth's magnetic field from ground magnetometers provided by the SuperMAG initiative. With this combination of spaceborne and ground based measurements, we attempt to expand our knowledge about the current systems associated with the non-conjugate auroral features. We present ground magnetometer measurements in the direct vicinity of the non-conjugate auroral features reported by *Reistad et al.* [2013] and interpret these in terms of asymmetric field aligned currents in the two hemispheres. The key objectives in the present thesis are to:

- Develop a method for identifying field aligned currents related to specific auroral features in conjugate areas of the two hemispheres

- Investigate the field aligned current system in both hemispheres, associated with non-conjugate aurora.

The thesis is organized as follows: In Chapter 2, basic concepts in space physics

relevant to this work are presented. Magnetic fields in the Sun-Earth system and basic space plasma theory are introduced in the first section. The Ionosphere and the current systems linking the magnetosphere to it are introduced in the next chapter. The last chapter describes the aurora and the processes that cause this well known phenomenon, and briefly revisits the mechanisms proposed to produce the non-conjugate aurora. Chapter 3 holds a description of the instruments and data used in this thesis. Special emphasis is placed on the description of the SuperMAG network of ground magnetometers and the cameras on board the IMAGE and Polar Satellites. In Chapter 4 we first describe the procedure for the image processing. The next section contains a detailed description of the different magnetic coordinate systems used and the transformation between these. The necessity and accuracy of this will be discussed in this as well as later Chapters. The last section of this chapter is crucial for the analysis of the results as it describes the methodical procedure used to interpret our results. We present the observations in Chapter 5 and each section is dedicated to one event. Data is presented first, followed by our interpretation. In Chapter 6 the observations are discussed and put into the context of our key objectives. Summary and conclusions follow in Chapter 7, while Chapter 8 lists ideas for future work.

2 Background

In this Chapter we give an overview of the theoretical background needed for the topics treated in this thesis. In the first section, basic concepts of space plasma and magnetic fields will be explained, starting at the Sun. Section 2.2 describes the currents in the magnetosphere - ionosphere system and how these are coupled. In the last section the aurora is briefly explained and a definition of non-conjugate aurora is presented.

2.1 Magnetic fields in the Sun - Earth system

To understand electromagnetic phenomena, such as aurora that occurs in the ionosphere surrounding the Earth, we need to understand the processes that cause them. In the following sections the coupling between the Sun, Solar Wind, the Earth's magnetosphere and the Ionosphere will be explained.

2.1.1 The Sun, Solar Wind and Interplanetary Magnetic Field

The Sun located at a distance of 1.5×10^{11} m from the Earth. It has a mass close to 2×10^{30} kg and the core temperature is assumed to be as high as 1.5×10^{7} K. The heat from the core is transported outwards by radiation and convection until it reaches the hottest and outermost part of the Sun, the corona. Here the temperature can be regarded as uniform and close to 10^{6} K. The Suns atmosphere in the corona is fully ionized and so hot that hydrogen and helium can escape its gravitational forces. This forms a continuous outflow of mass called *solar wind* [*Brekke*, 2013].

As a result of the constant illumination, high temperature, and compression and subsequent expansion of the corona, the solar wind is a fully ionized supersonic plasma flow [*Kelley*, 2009]. It is quasi neutral and consists of an equal amount of electrons and protons. The magnetic field of the Sun is structured by convective flow of conducting material on the surface and the magnetic properties are transported outward as the solar wind expands. Its temperature decreases adiabatically while the

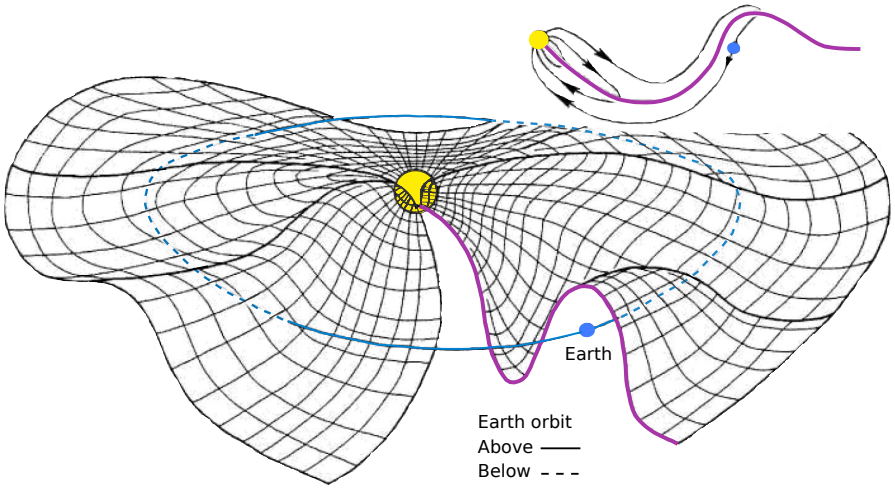

Figure 2.1: A three-dimensional sketch of the solar equatorial current sheet separating the anti-parallel magnetic field lines. The small upper figure is a sideways view, the xz-plane in GSE coordinates, of the larger figure where the magnetic field lines are indicated in black. The purple line indicates the current sheet. Outwards pointing field lines are above the current sheet, indicated by the grid surface, and inward pointing field lines are below the current sheet. The Figure is adopted from *Kelley* [2009].

density decreases with the inverse square of the distance to the Sun [*Baumjohann and Treumann*, 2012]. Figure 2.1 shows a sketch of the Suns magnetic field as it stretches outwards, in the small upper panel. Magnetic field lines are directed outwards above the purple line indicating the solar equatorial current sheet and towards the Sun below. The direction of the Sun's magnetic field reverses with a period of 11 years [*Babcock*, 1961].

The solar equatorial current sheet is a result of the geometry of the magnetic field. Adjacent, anti parallel magnetic field lines must be separated by a current sheet as a consideration of Maxwells equation, $\nabla \times \mathbf{B} = \mu_0 \mathbf{J}$, shows. In the larger panel of Figure 2.1 the solar equatorial current sheet is indicated by the checkered surface. It forms a skirt-like configuration, rotating with a 27 day period. The orbit of the Earth around the Sun is alternately above and below the solar equatorial current sheet, observed as a change in the direction of the magnetic field. The small upper panel of Figure 2.1 shows a cross section, in the plane containing the Earth-Sun line and Z, normal to the Earth's elliptic plane, where the Earth is below the current sheet.

The Solar magnetic field is *frozen in* (see Chapter 2.1.3.2) to the streaming, hot, supersonic, magnetized and collision-less plasma of the solar wind. This is called the Interplanetary Magnetic Field (IMF). The components of the IMF are denoted B_x, B_y and B_z for the *x, y,* and *z* direction, where x is positive toward the Sun on the Sun-Earth line, z is along the dipole-axis of the Earth and y completes the right handed system. The IMF is the dominant parameter coupling the solar wind to the Earth's magnetosphere (see Chapter 2.1.4) [*Dungey*, 1961; *Sonnerup*, 1974]. At a distance of the Earth's orbit, typical value ranges of the solar wind are [*Baumjohann*

and Treumann, 2012]:

Typical Solar Wind values	
Velocity, v	300 - 1500 $\frac{\text{km}}{\text{s}}$
Temperature, T	10^5 K
Density, ρ_e	5 cm^{-3}
Field strength, B_T	3 - 12 nT

2.1.2 Earth's Magnetic field

The Earth's magnetic field has its origin in the interior of the Earth. To first order it can be approximated as a dipole field, tilted relative to the Earth's rotational axis [*Kelley*, 2009]. Currently the magnetic pole in the northern hemisphere is tilted towards North America by an angle $\lambda_{tilt} \approx 11°$. The Earth's magnetic field is affected by the IMF and the interaction between them shapes the *magnetosphere*. The boundary separating the magnetosphere and the interplanetary space dominated by the IMF is called the *magnetopause*. A combination of normal and tangential stresses, like pressure and viscous effects between the two regions, from the solar wind/IMF form the magnetosphere [*Russel*, 1986]. The pressure from the solar wind compresses the dipole field at the magnetopause on the dayside of the Earth. On the nightside the terrestrial field is stretched out anti-sunward, into a long tail-like configuration. This is called the *magnetotail* and stretches far out into space. This configuration of the Earth's magnetic field is sensitive to changes in the IMF and dynamically dependent on the direction of the IMF. This will be discussed further in Chapter 2.1.4.

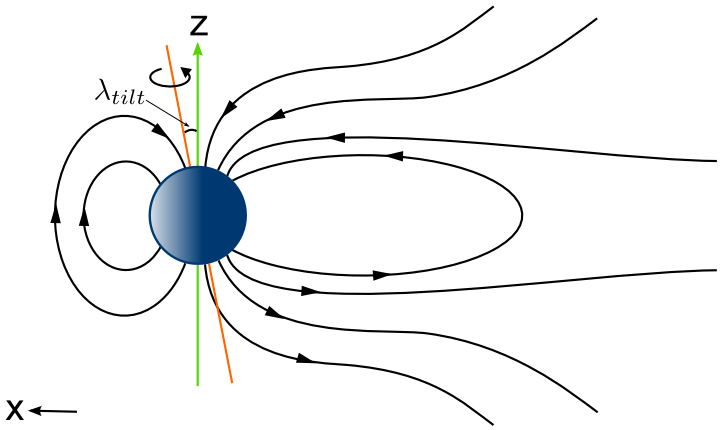

Figure 2.2: A sketch of the Earth's magnetic field. x is in the Sunward direction, z is along the Earth's dipole axis shown in green and y is positive out of the plane. The rotational axis of the Earth is indicated in orange, and as the Earth rotates the green dipole axis will wobble relative to it.

2.1.3 Fluid description of a Plasma

The Earth's magnetic field is affected by the plasma carried in the solar wind, thus the dynamics of this system involves mechanics of the plasma motion. To understand the motion and dynamics of the Earth's magnetic field, we first need to understand the properties of the large scale bulk-motion of the plasma [*Parker*, 2007].

2.1.3.1 Magnetohydrodynamics

A plasma can be described as a fluid if the density is known on a scale where macroscopic variables do not change much. The equations describing the dynamics of a plasma fluid are conservation laws for mass and momentum. The derivation of these is carried out in detail in several textbooks [e.g. *Baumjohann and Treumann*, 2012; *Parker*, 2007]. The equations are as follows:

$$\frac{\partial \rho}{\partial t} + \mathbf{v} \cdot \nabla \rho = 0 \tag{2.1}$$

where $\rho = nm$ and $\nabla \cdot \mathbf{v} = 0$ is assumed. Equation 2.1 is the continuity equation for a plasma fluid and states that in a plasma where no particles are added or subtracted the number density, n, mass, m, and velocity $\mathbf{v}$ are conserved during the motion of the plasma.

$$\rho\left(\frac{\partial v}{\partial t} + \mathbf{v} \cdot \nabla \mathbf{v}\right) = -\nabla \cdot \bar{\mathbf{P}} + \mathbf{j} \times \mathbf{B} \tag{2.2}$$

Equation 2.2 is the momentum density conservation equation of the plasma in motion. It relates the velocity of the plasma fluid and the electromagnetic forces acting on the fluid. The left side of the equation is the net change of momentum density of a fluid element. $\bar{\mathbf{P}}$ is the fluid pressure or plasma pressure tensor, which arises due to the random motion of the particles the mean bulk velocity. The $\mathbf{j} \times \mathbf{B}$ term is the divergence of the Maxwell stress tensor and relates the magnetic pressure and tension forces on the magnetic field lines to the change of momentum density of the plasma fluid volume.

The above equations are called magnetohydrodynamic (MHD) equations. For a plasma, the variables n, m and $\mathbf{v}$ are considered to be some combination of the individual mass, number density and velocity of the ion and electron fluids. In the reference frame of a moving plasma in space and most of the magnetosphere, magnetic fields are conserved while any electric fields that may arise, cancel. The highly mobile electric charges in a moving plasma cancel potential differences rapidly. Because no magnetic monopoles exist, this cancellation does not happen for magnetic fields and thus they are conserved [*Parker*, 2007].

MHD equations describe the evolution of the plasma where time-scales are larger than the inverse plasma frequency and length-scales are much larger than the Debye length. This is the case for most of the magnetosphere and actually the rest of the cosmos with only a few exceptions [*Parker*, 2007]. However, one important example of when MHD breaks down are regions where magnetic reconnection occurs. This is an important concept, and necessary for understanding the plasma circulation in the Earth's magnetosphere and its coupling to the solar wind. The topic will be

discussed in Chapter 2.1.4.

2.1.3.2 Frozen in concept

Electric fields cannot be supported in the moving frame of the plasma. This is true almost everywhere in space, where plasma is collision-less, gravity can be neglected and only the electromagnetic forces act on the plasma. Important exceptions to this, related to the break-down of ideal MHD exist, and will be discussed in Chapter 2.1.4. The non-relativistic Lorenz transformations of the electric and magnetic fields are described by the following equations:

$$\mathbf{E}' = \mathbf{E} + \mathbf{v} \times \mathbf{B} \tag{2.3a}$$

$$\mathbf{B}' = \mathbf{B} - \frac{\mathbf{v} \times \mathbf{E}}{c^2} \tag{2.3b}$$

In the reference frame of the collision-less plasma moving at velocity $\mathbf{v}$, the electric field is $\mathbf{E}' \approx 0$. Equation 2.3a then becomes:

$$\mathbf{E} = -\mathbf{v} \times \mathbf{B} \tag{2.4}$$

This is the electric field observed when considering a plasma fluid volume at velocity $\mathbf{v}$. The physics of electromagnetic fields is the same in all moving frames and Maxwells equations apply. Faradays law for a collision-less plasma of infinite conductivity is one of Maxwells equations and stated as follows:

$$\frac{\partial \mathbf{B}}{\partial t} = -\nabla \times \mathbf{E} \tag{2.5}$$

Inserting Equation 2.4 into this yields:

$$\frac{\partial \mathbf{B}}{\partial t} = \nabla \times (\mathbf{v} \times \mathbf{B}) \tag{2.6}$$

This is the MHD induction equation for an ideal fluid. Its physical implication is that the magnetic field is carried bodily with the plasma. The plasma can not cross magnetic field lines but move along them. This can be shown by examining the time rate of change of a plasma volume bound to a magnetic field line, with cross section $\mathbf{A}$ and magnetic field $\mathbf{B}$. The magnetic flux Φ through this area is

$$\Phi = \int_A \mathbf{B} \cdot d\mathbf{A} \tag{2.7}$$

exist As the magnetic field $\mathbf{B}$ does not change with time, the rate of change of the flux $\frac{\partial \Phi}{\partial t}$ must be zero as well. This is true also when the field line and the plasma are moving through space. A detailed calculation and discussion of the above is given in *Parker* [2007]. This result is known as the *frozen in* theorem of space plasma and is illustrated in Figure 2.3. Initially magnetic field lines are straight, shown in black in the first column. If a patch of plasma is moved, illustrated by the orange arrows, the magnetic field lines will be deformed accordingly, as illustrated in the second and third panel. This is a fundamental concept in the understanding of the dynamic processes in the magnetosphere.

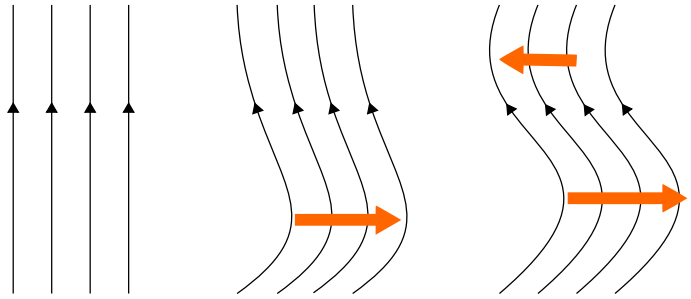

Figure 2.3: The *frozen in* theorem illustrated by magnetic field lines (black) moving with the plasma (orange).

2.1.4 Magnetic Reconnection and the Dungey cycle

In Chapter 2.1.3 we state that the plasma flow can not alwasy be assumed to be collision-less and *frozen in*. In fact, it is the violation of those principles that allows for the interaction between the solar wind and the Earth's magnetosphere [*Strangeway*, 2009]. The most important example of this is magnetic reconnection, namely the process where field lines are cut and reconnect to oppositely directed field lines, thus changing the topology of the magnetic field. This process is rather complex and still an active field of research. In this thesis we will not go into detail, but try to outline the basic concept of the process [*Baumjohann and Treumann*, 2012; *Biskamp*, 2000].

Figure 2.4 illustrates the concept of reconnection. At a time $t = 0$ two domains have stationary magnetic field lines with anti-parallel components (see Figure 2.4a). An example of this is the previously mentioned solar equatorial current sheet, where magnetic field lines point away from the Sun above the current sheet and towards the Sun below the current sheet (see Chapter 2.1.1). However, if the field lines are not stationary but moving towards each other, a magnetic neutral point where the magnetic field is zero can be established. The middle panel of Figure 2.4 illustrates this step, where the red arrows indicate the flow of the plasma. Here the magnetic field is zero at the center of the figure, in the middle of the bent X-like configuration. In a three dimensional space this neutral point or X-point forms a line, often called the neutral line or X-line. In Figure 2.4 it would extend out of the page. The result of this process is illustrated in the right panel of the figure. The field lines and the plasma are transported towards the neutral point. Here the field lines break and the *frozen in* approximation breaks down. This happens first for ions and is indicated by the yellow area in the figure. The green area indicates where the MHD approximation for electrons break. The cut field lines from one domain reconnect with a cut field line from the other and form a new magnetic field line. Due to magnetic tension forces the new field line is then expelled from the neutral point and moves away. With the new field line, a mix of plasma populations from both domains are transported in a direction perpendicular to the original flow, illustrated by the red arrows.

In the case of the Earth's magnetosphere, magnetic reconnection occurs commonly in two areas for certain configurations of the IMF. The first area is at the magnetopause on the dayside of the magnetosphere. If the IMF has a southward (i.e.

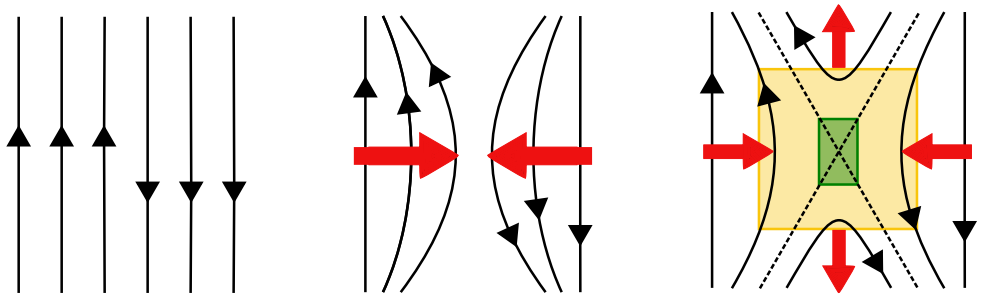

(a) $t = 0$ (b) $t = 1$ (c) $t = 2$

Figure 2.4: Sketch illustrating the evolution of the magnetic field topology during magnetic reconnection of anti-parallel field lines. At time $t = 0$ the field lines are anti-parallel and stationary. When forces act on the plasma frozen to the field lines, the field lines may converge toward each other. This is illustrated in panel *b* at time $t = 1$. At time $t = 2$, the *frozen in* approximation breaks down, first for ions, indicated by the yellow area and then for electrons, indicated by the green area. The red arrows indicate the flow of the plasma.

negative z) component it can reconnect with the closed field lines of the Earth's magnetic field and form open field lines, each with one footpoint in the solar wind and one footpoint on Earth. This is illustrated in Figure 2.5, where the progress of one field line is tracked through the Earth's magnetosphere. The incoming IMF field line numbered *1*, reconnects with the Earth's magnetic field and is now open. Due to the momentum of the solar wind, the open field line is transported anti-sunward, illustrated by the field line at stage *2, 3, 4, 5* and *6*. This process is what forms the magnetotail mentioned in Chapter 2.1.2. The second area of reconnection is on the nightside, where the open field line that was transported from the dayside may reconnect and form new a closed field line. Line number *7* in Figure 2.5 illustrates this in the magnetotail. The new field line, number *8*, will then relax and move towards the Earth, transporting plasma (originally in the solar wind) frozen to the field line. The direction of the plasma transport during this process is illustrated by the yellow and orange arrows. In an equilibrium situation the newly closed field line will convect back to the dayside magnetosphere and close the cycle. This conceptual picture of the plasma circulation was first suggested by *Dungey* [1961] and is now widely known as the *Dungey cycle*.

2.1.4.1 Effects of the IMF B_y and B_x

The two other components of the IMF also affect the Earth's magnetic field, but in a different manner than the B_z component. The B_y and B_x components of the IMF can cause asymmetries of the open magnetic field lines by reconnection on the dayside. A newly opened field line on the dayside is transported tailward, as the IMF acts on the field line, creating magnetic tension. The magnetic tension force is different for the two parts of the newly opened field line. When the field lines have convected to the magnetotail, the two open field lines initially together will not reconnect with each other. Instead, reconnection can occur with other open field lines in the tail. This process is sketched in Figure 2.6. The left panel illustrates the

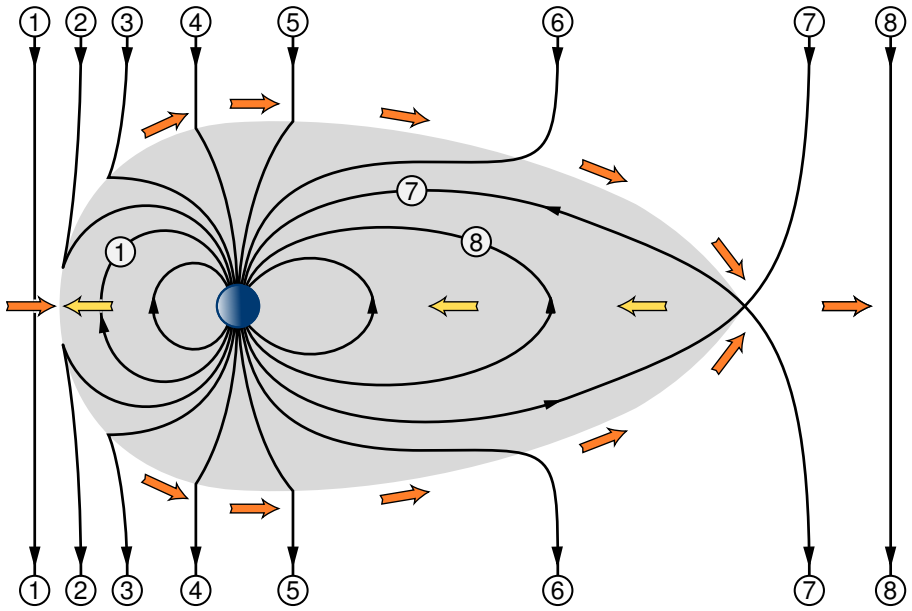

Figure 2.5: The Dungey cycle is the conceptual picture of the plasma circulation driven by the magnetospheric reconnection and convection in the Earth's magnetosphere. The numbered field lines show how the solar wind magnetic field reconnects to the Earth's magnetic field (*1*) and subsequently is transported to the magnetotail (*2,3,4,5,6*) and eventually reconects again in the tail (*7*). Here the flow is reversed and the magnetic field lines and the plasma carried by them is convected towards the dayside (*8*). Figure adopted from *Baumjohann and Treumann* [2012].

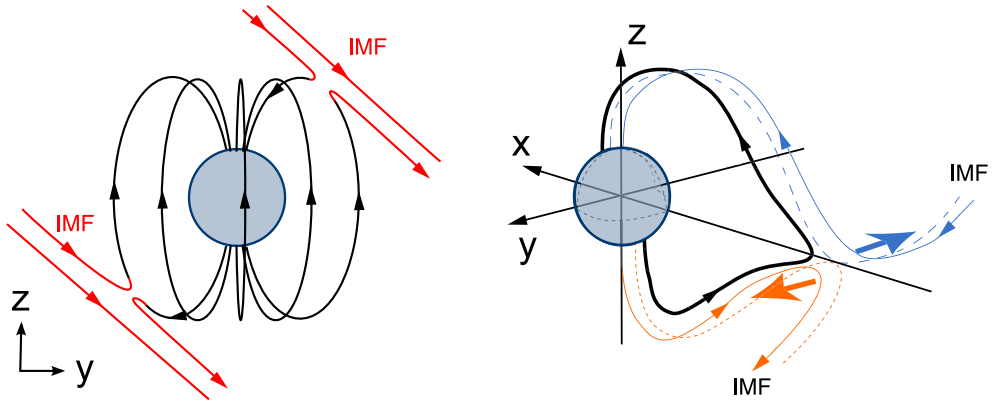

Figure 2.6: A sketch of the different reconnection locations on the dayside for a positive IMF B_y is shown in the left panel. The right panel shows a sketch of the subsequent reconnection in the tail. Field lines with symmetric footpoints in the two hemispheres will not reconnect due to an oppositely directed magnetic tension force, indicated by the large orange and blue arrows. Instead field lines with certain asymmetric footpoints will reconnect and introduce a magnetic field component in the y-direction to the Earth's magnetic field. The figure in the right panel is adopted from *Østgaard et al.* [2004]

different locations at which reconnection can occur on the dayside of the magnetosphere, for a positive IMF B_y component. The magnetic tension force in the bend of the newly open field lines is directed in the opposite direction for the two field lines. The right panel shows the situation subsequent to the convection of the field lines to the nightside and reconnection in the tail. The field lines with symmetric footpoints in the two hemispheres, indicated by the solid orange and blue lines, will not reconnect as they are pulled away from one another. Instead, field lines with asymmetric footpoints in the two hemispheres, indicated by the dashed orange and blue lines, can reconnect. The result is a closed field line with asymmetric footpoints in the two hemispheres in a geomagnetic coordinate system [*Østgaard et al.*, 2004]. The penetration of the IMF B_y component into the Earth's magnetosphere is supported by satellite measurement, reporting a twist in the magnetotail at geosynchronous orbit, in the direction of the IMF B_y [*Lui*, 1984; *Wing et al.*, 1995].

Similarly, the IMF B_x component can affect the Earth's magnetic field. Instead of a dawn-dusk asymmetry this can cause a north-south asymmetry. Magnetic tension on the two parts of the initially closed and now open magnetic field line is different in the two hemispheres. Figure 2.7 illustrates this. After the open field lines have convected to the magnetotail, the tension force differs for the two end of the initially closed field lines. This is suggested to affect the energy conversion from the solar wind to the magnetosphere [*Cowley*, 1981; *Reistad et al.*, 2014].

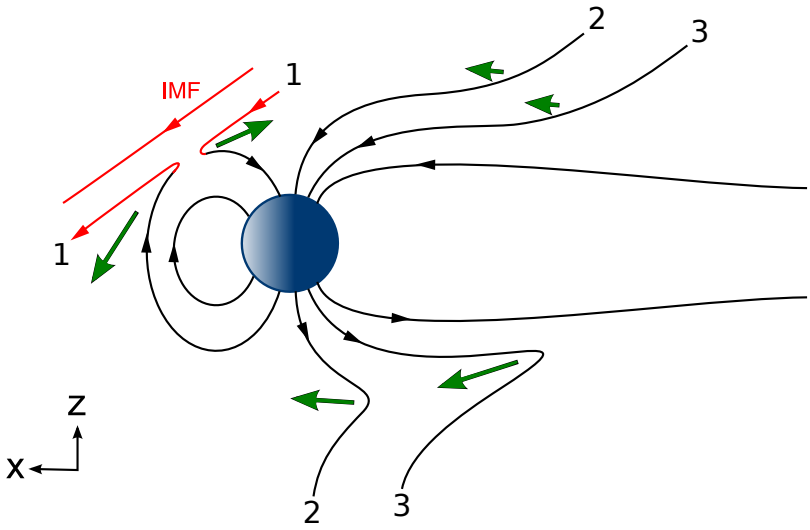

Figure 2.7: A sketch of the reconnection process for a positive IMF B_x and negative IMF B_z component. The tension, indicated by the green arrows, in the northern and southern hemisphere differs. Figure adopted from *Cowley* [1981].

2.1.5 Ionosphere

The ionosphere is the ionized part of the Earth's atmosphere and it is the transition region from the fully ionized magnetospheric plasma to the neutral atmosphere. Solar UV radiation ionizes a fraction of the neutral atmosphere depending on density and chemical composition [*Baumjohann and Treumann*, 2012]. The ionosphere can be viewed as a shell of variable ionization where the ionization is highly altitude dependent [*Brekke*, 2013]. Thus, it consists of several regions. The region with the highest plasma density is called the F-region at an altitude range of 100-500 km, with a peak around 300 km. Below, at an altitude range from 90-150 km, is the E-region with an ionization peak around 110 km. The region below 90 km altitude is termed the D-region, and is only weakly ionized.

Chapter 2.1.4 described the circulation pattern of magnetic field lines in the Earth's magnetoshpere as a result of magnetic reconnection. Reconnection occurs first on the dayside and subsequently the open magnetic field lines are transported towards the nightside due to the solar wind flow, with one footpoint in the solar wind and one footpoint on Earth. Because plasma is *frozen in* to the magnetic field lines, this motion applies to the plasma as well. As the ionosphere is initially at rest, the magnetospheric motion creates a tension force on the magnetic field lines. This perturbation from the bend in the field line propagates downward into the ionosphere. The neutral particles in the atmosphere are not directly affected by electromagnetic forces, while the plasma in the ionosphere is accelerated. This introduces collisions of the plasma species with the neutrals in the ionosphere. As a result the field lines are bent further. The magnetic field continues to bend, until the tension forces balance the frictional forces arising from the collisions of the plasma [*Song and Vasyliunas*, 2011]. The collisional plasma is accelerated by this process and as a result the ionospheric flow pattern matches that of the magnetospheric flow [*Strangeway*, 2009]. Figure 2.8 shows a sketch of the resultant ionospheric flow pattern. Orange

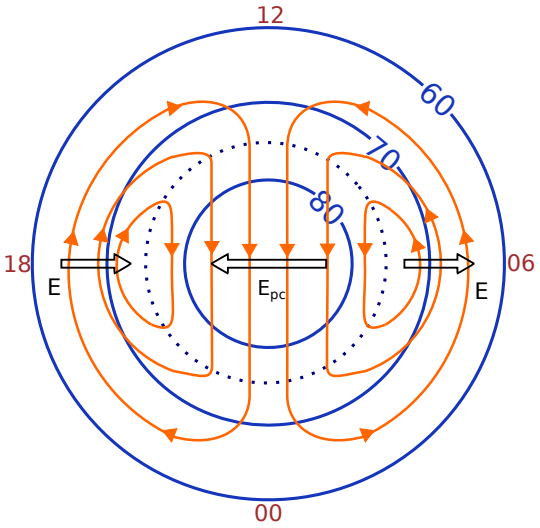

Figure 2.8: Schematic view of the convection pattern in the polar ionosphere. The orange lines indicate the general direction of the flow. Concentric solid blue circles show latitude in degrees, while the dashed blue circle indicates the poleward boundary of the auroral oval. The black arrows indicate the high-latitude electric field caused by the flow of the magnetic field across the polar cap.

lines indicate the convection streamlines of the plasma flow. The black arrows illustrate the ionospheric electric field, as a result of the the stress imposed on the ionosphere by the magnetospheric flow. Figure 2.8 is a simplified sketch of the convection pattern to illustrate this concept. The actual pattern of convective flow is closely linked to the direction and magnitude of the IMF and varies greatly in shape according to it [e.g. *Cowley et al.*, 1991; *Förster et al.*, 2008; *Weimer et al.*, 2010]. In addition, the pattern in the two hemispheres can be very different, particularly during a southward directed IMF and thus enhanced energy input from the solar wind [*Haaland et al.*, 2007].

2.1.6 Two paradigms

The ionospheric processes explained above, are presented in what is known as the **B v** paradigm (where **B** is the magnetic field and **v** the plasma bulk flow). The ionospheric electric fields are explained in terms of the magnetic field and plasma motion. This is in contrast to the **E j** paradigm (**E** is the ionospheric electric field and **j** the electrical current density), where the electric field in the ionosphere is established as the cause for the plasma motion. Several authors argue [e.g. *Parker*, 2007; *Vasyliunas*, 2005; *Vasyliunas and Song*, 2005] that using the premise that the electric field causes the plasma motion hides the fundamental physics and is thereby false. However, in the reference frame of the Earth the **E j** approach is valid and is commonly used in ionospheric physics [*Kelley*, 2009].

2.2 Currents

Currents transport mass, charge, momentum and energy and are crucial to the coupling of the Earth's magnetosphere to the ionosphere. A complicated system of currents exists within the magnetosphere as a result of the distortion from the solar wind flow. The importance of the magnetic field aligned currents, linking the ionosphere and magnetosphere of the Earth, was first suggested by *Birkeland* [1908]. In the following the large scale magnetospheric currents, field aligned and ionospheric currents are described. The last section of this chapter describes how these can be measured.

2.2.1 Magnetospheric currents

Chapter 2.1.2 discusses the Earth's magnetic field and how it is distorted by the continuous flow of the solar wind in space. This distortion of the dipole field is associated with large scale current systems in the Earth's magnetosphere and field aligned currents coupling the magnetosphere and the ionosphere [*Akasofu*, 1983]. Figure 2.9 shows a schematic view of the large scale magnetospheric currents. Associated with the transition region from the IMF to the Earth's magnetic field are the *magnetopause current* in the compression region on the dayside and its corresponding *tail current* on the nightside. Connected to the *tail current* is the *neutral sheet current* flowing across the magnetosphere from dawn to dusk. Some of the *tail current* also connects to the *magnetopause current* [*Strangeway*, 2009]. The *ring current* flows in a westward direction around the Earth at a distance of several Earth radii. These currents flow perpendicular to the Earth's magnetic field. The currents flowing parallel to the magnetic field, shown in red in Figure 2.9, are the large scale *field aligned currents* connecting the magnetospheric currents to the ionospheric currents, closing the system. These currents are affected, and additional currents, like the substorm current wedge (see Chapter 2.3), can be induced by different configurations of the IMF as the magnetosphere opens and magnetic reconnection occurs [*Dungey*, 1961; *Strangeway*, 2009] (see Chapter 2.1.4). Figure 2.9 does not show the complex system of ionospheric currents, which we will discuss in Section 2.2.3.

2.2.2 Field Aligned Currents

Field aligned currents are the link between the magnetosphere and ionosphere, and play a central role in the transfer, conversion and circulation of energy and momentum between the two regions [*Iijima*, 2000]. Kristian Birkeland was the first to suggest that electric currents in the atmosphere (the ionosphere was not discovered at that time) are associated with the aurora and that these currents flow in and out of the upper polar atmosphere along the magnetic field lines of the Earth [*Birkeland*, 1908; *Potemra*, 1985]. Their existence was later confirmed by in situ measurements [*Zmuda and Armstrong*, 1974a,b] and has since been the subject of many studies [e.g. *Iijima*, 2000]. *Iijima and Potemra* [1978] determined the large scale morphology of the the field aligned currents in the Earth's polar ionosphere as shown in Figure 2.10. Currents that flow into the ionosphere on the dawn side and out of the ionosphere on the dusk side at the higher latitudes are referred to as *Region 1 (R1)*

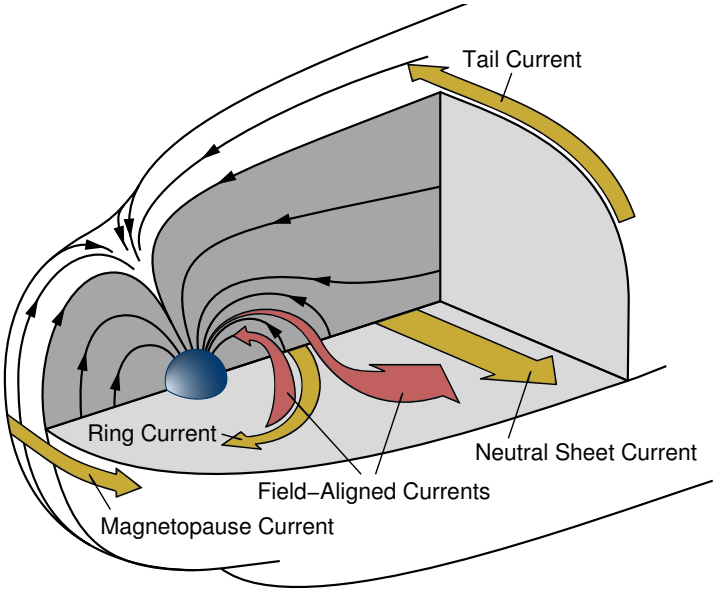

Figure 2.9: Schematic of the magnetospheric currents around the Earth. Currents are shown in yellow, while black arrows indicate the Earth's magnetic field. The large scale field aligned currents are indicated in red. Figure adopted from *Baumjohann and Treumann* [2012].

currents. Currents at the lower latitudes flow in the opposite direction to the *R1* currents and are referred to as *Region 2 (R2)* currents. These current configurations are persistent during a magnetic *substorm*, which is defined as a time interval where the energy dissipated from the magnetosphere into the auroral oval in the ionosphere is increased [*Rostoker et al.*, 1980]. This process was first termed *auroral substorm* and described in detail by *Akasofu* [1964]. Both the *R1* and *R2* currents increase as the magnetic activity increases [*Sugiura and Potemra*, 1976]. *R1* are more intense than *R2* currents and close in different regions in the magnetosphere.

2.2.3 Polar Ionospheric Currents

The ionosphere is generated by the highly altitude dependent ionization of the neutral gas in the Earth's atmosphere. Hence, the conductivity of the different plasma species, entering the ionosphere via the field aligned currents, is altitude dependent. As the plasma enters regions of higher density in the atmosphere it becomes collisional, and the MHD equations specified in Chapter 2.1.3.1 no longer apply. Instead the equations need to be modified to include collisions for each of the plasma species [*Strangeway and Raeder*, 2001]. The difference of mass and cross section of the the plasma species cause collisions to become important at a higher altitude for ions than for electrons. In the presence of an electric field, this leads to a charge separation causing a net current. In a fully ionized plasma with low collision frequencies and infinite conductivity, *Ohm's law* is given by:

$$\mathbf{j} = \sigma(\mathbf{E} - \mathbf{v} \times \mathbf{B}) \tag{2.8}$$

where σ is the plasma conductivity. Accounting for collisions and the different mass and cross-section of the species, which give rise to different gyro and neutral-collision

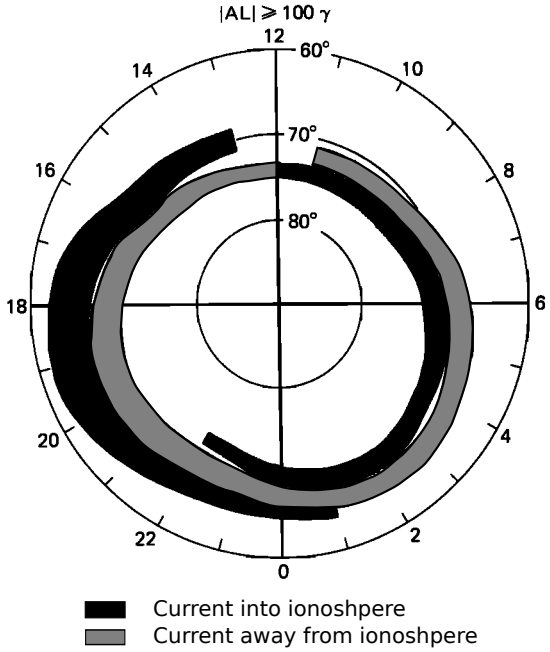

Figure 2.10: Distribution of the large scale field aligned currents in the polar ionosphere, adopted from *Iijima and Potemra* [1978].

frequencies, and decomposing *Ohm's law* states:

$$\mathbf{j} = \sigma_{\parallel}\mathbf{E}_{\parallel} + \sigma_P\mathbf{E}_{\perp} - \frac{\sigma_H(\mathbf{E}\times\mathbf{B})}{B} \tag{2.9}$$

where $\sigma_{\parallel}$ is the *conductivity* parallel to the magnetic field $\mathbf{B}$. This first term on the right hand side is zero as the parallel electric field goes to zero as $\sigma_{\parallel}$ goes to infinity along magnetic field lines. The conductivities denoted by σ_P and σ_H are the *Pedersen* and *Hall conductivities* perpendicular to the Earth's magnetic field, $\mathbf{B}$. The *Pedersen current*, $\mathbf{j}_P = \sigma_P\mathbf{E}_{\perp}$, is carried by the motion of the ions and flows along the present ionospheric electric field (see Chapter 2.1.5) and perpendicular to the magnetic field $\mathbf{B}$ [*Kelley*, 2009]. The *Hall current*, $\mathbf{j}_H = \sigma_H(\mathbf{E}_{\perp}\times\mathbf{B})$, is carried by the electron motion relative to the motion of the ions with the neutrals (due to collisions) and is perpendicular to both the electric field and the magnetic field. As the ionospheric conductivity is highly altitude dependent, the range in which these perpendicular currents can flow is from approximately 90 km to 130 km altitude. The Hall currents flow closest the surface of the Earth, while the Pedersen currents flow above [*Baumjohann and Treumann*, 2012]. The resulting horizontal current pattern in the polar ionosphere is sketched in Figure 2.11. The green circular region indicates the auroral oval. The horizontal eastwards and westward electrojet primarily consisting of the Hall currents are indicated in red. The primary source of σ_H and thus, the Hall currents, is the solar radiation on the dayside and the electron precipitation in the auroral oval maximizing around 00 MLT [*Ahn et al.*, 1999]. As a result, enhanced field aligned currents during magnetic substorm can intensify these substantially. The intense westward electrojet flows in the morning sector and typically extends past 00 MLT along the poleward boundary of the auroral oval, where it then diverges into field aligned currents. This westward component of the

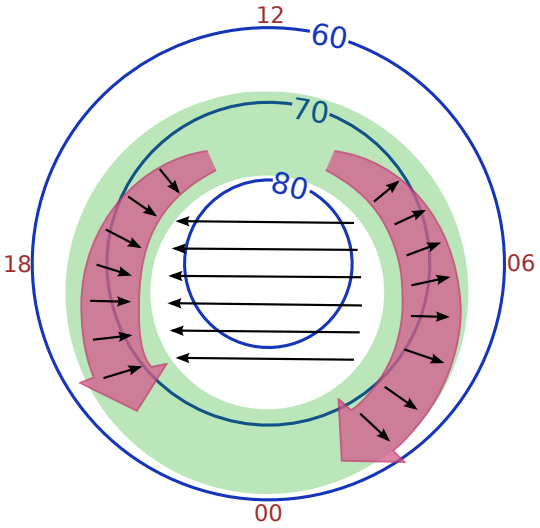

Figure 2.11: A sketch of the horizontal Hall and Pedersen currents in the polar ionosphere. Black arrows indicate the Pedersen currents, while two red arrows indicate the Hall currents. These are also called the eastward (left) and westward (right) electrojets. The green circle is a sketch of the auroral oval.

Hall current, is sometimes enhanced in the midnight sector, due closure of the substorm current wedge (see Chapter 2.2.4) [e.g. *McPherron et al.*, 1973; *Newell and Gjerloev*, 2011]. The black arrows show the horizontal Pedersen currents, peaking at an altitude around 130 km. The Pedersen currents are fed by the field aligned *R1* and *R2* currents (see Figure 2.10). The region spanning from around 21 MLT to 01 MLT is called the *Harrang discontinuity region*. Here, the Pedersen currents overlap and three sheets of field aligned currents exist.

Figure 2.8 and 2.11 are idealized sketches of the convection and currents in the polar ionosphere. As mentioned in Chapter 2.1.5, the pattern of the convection depends greatly on the direction and magnitude of the IMF and reflects the pattern of the plasma convection in the magnetosphere. The same is true for the current system in the ionosphere as it is closely linked to the convection. The solar wind - magnetosphere - ionosphere system is highly dynamic and thus the average convection pattern changes [e.g. *Kelley*, 2009; *Weimer et al.*, 2010]. The auroral electrojets are also affected by the seasonal differences [*Guo et al.*, 2014] and recent studies show that the convection patterns can be very different in the two hemispheres for a given orientation of the IMF [*Haaland et al.*, 2007].

2.2.4 Substorm currents

In Chapter 2.1.4 the concept of magnetic reconnection and the flow of plasma in the Earth's magnetosphere was described. The Dungey cycle does not nessessarily represent an equilibrium state with the same amount of reconnection on the dayside as on the nightside but can be greatly dependent on the orientation of the IMF and the solar wind speed. Magnetic flux transported to the tail of the Earth's magnetic field by the solar wind may build up and reconnect abruptly in the tail. Plasma

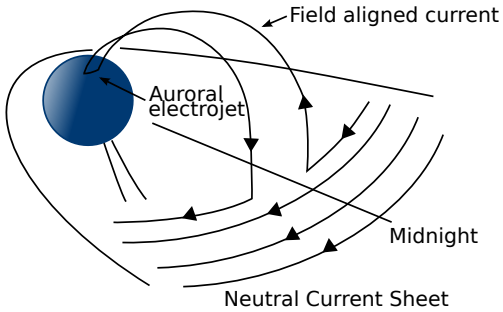

Figure 2.12: Sketch of the disruption in the neutral current sheet forming the substorm current wedge. Downward field aligned currents on the morning side close in the ionosphere and flow upwards and back to the neutral current sheet. Figure adopted from *Mcpherron et al.* [1973].

particles, initially from the solar wind, frozen to the field lines, are accelerated and deposited in the auroral oval of the ionosphere. This interval of sudden increased energy dissipation in the ionosphere is termed *auroral substrom* and has a vivid observable effect in the form of aurora and the horizontal ionospheric currents [*Rostoker et al.*, 1980]. The aurora will be discussed in more detail in Chapter 2.3.

The current pattern during a magnetospheric substorm consists of two components. First, as a result of the increased reconnection and magnetospheric plasma circulation during intervals with a significant southward directed component of the IMF, the plasma circulation in the ionosphere increases. This enhances the Hall currents/electrojets in the auroral oval. Second, a *substorm electrojet* is formed in the ionosphere, as a result of a *substorm current wedge*. These two mechanisms have very different time evolution and intensity [*Kamide et al.*, 1996].

The substorm current wedge (SCW) was introduced by *Mcpherron et al.* [1973]. It is formed when part of the neutral sheet current (see Figure 2.9) diverts through a downward field aligned current into the ionosphere, a westward auroral electrojet and an upward field aligned current on the west side of the wedge. The current in the neutral current sheet is enhanced prior to a substorm [*Kaufmann*, 1987]. Figure 2.12 illustrates this process and highlights how the magnetosphere is directly coupled to the ionosphere.

2.2.5 Measuring ionospheric and field aligned currents

Steady currents generate magnetic fields that are constant in time. This relation is expressed by Biot-Savarts law

$$\mathbf{B}(\mathbf{r}) = \frac{\mu_0}{4\pi} \int \frac{\mathbf{J}(\mathbf{r}') \times \mathbf{r}}{r^3} d\tau' \tag{2.10}$$

where $\mathbf{J}(r') = \mathbf{J}(x', y', z')$ is the current distribution inside a volume $d\tau = dx'dy'dz'$, and $\mathbf{B}(\mathbf{r})$ is the magnetic field induced by the volume current at a point $\mathbf{r} = (x, y, z)$.

Currents in the magnetosphere-ionosphere system generate magnetic fields that can disturb the Earth's magnetic field. In the present thesis, the current generated

magnetic field at ground level is termed ground magnetic perturbation field. The magnetic perturbation fields can be measured with magnetometers in space and on the Earth's surface to study the characteristics of the currents. Ground-based magnetometers determine the magnetic perturbation field along three mutually perpendicular components, usually in the north-south, east-west and vertical direction. The method used for interpreting ground magnetometer data, will be explained in detail in Chapter 4.4, and has been used in numerous studies using observatories at mid- and low-geomagnetic latitudes [e.g. *Akasofu and Meng*, 1969; *Clauer and McPherron*, 1974; *Fukushima and Kamide*, 1973a; *Haaland et al.*, 1999; *Nakano*, 2005]. A number of studies use ground magnetometer data from all stations above mid-latitudes ($< 60°$) during various conditions to determine characteristics of the polar ionosphere , like conductivity distribution, electric field potential, large scale current distribution, the auroral electrojets and field aligned current distribution, of the polar ionosphere [e.g *Friis-Christensen et al.*, 1985; *Guo et al.*, 2014; *Kamide and Kokubun*, 1996; *Kamide et al.*, 1981]. *Gjerloev and Hoffman* [2014] argue that perturbations measured by stations within the polar cap are largely due to field aligned currents flowing into the auroral zone. In this thesis we aim at using ground magnetometer stations at high latitudes and stations in the auroral oval in addition to stations at mid-latitudes simultaneously, to investigate currents associated with the non-conjugate auroral features (see Chapter 4.4).

The geomagnetic field lines at latitude regions of the auroral oval and higher, are close to vertical. For the ideal case of radial field lines in a spherical geometry and uniform conductivity in the ionosphere, the magnetic perturbation from the field aligned currents and the irrotational, spreading horizontal Pedersen currents cancel exactly [*Fukushima*, 1976]. The ground magnetic perturbations observed below the ionosphere are then solely due to the horizontal ionospheric hall currents. This is known as *Fukushimas Theorem*. For realistic, curved field lines and a non-uniform ionospheric conductivity, *Fukushimas Theorem* does not hold [e.g. *Fukushima*, 1994; *Vasyliunas*, 2007]. *Sun et al.* [1985] found the effect of vertical versus non-vertical field lines on the ground magnetic perturbation to differ by 5-20 % at high latitudes around the auroral zone, and 15-35% at mid-latitudes ($< 60°$). It is mathematically impossible to determine the true three-dimensional current distribution solely from ground magnetic perturbation measurements, as they are a superposition of horizontal ionospheric currents, field aligned currents and currents in the distant magnetosphere [e.g. the ring current *Fukushima and Kamide*, 1973a,b].

2.3 The Aurora

The aurora is a signature of the magnetospheric processes and dynamics. It is caused by the energetic electrons and ions precipitating into the polar ionosphere along the magnetic field lines. The radiation is the result of collisions between the constituents of the atmosphere and the precipitating particles. The kinetic energy from precipitating particles causes, in part, the atoms and molecules in the atmosphere to excite. During the relaxation process of the excited atmospheric particles, the excess energy is given of as radiation at characteristic wavelengths determined by the species [*Kivelson and Russel*, 1996]. Part of this light can be

seen from the Earth and space by the naked eye.

2.3.1 Non-conjugate Aurora

For a symmetric dipole field of the Earth, the auroral features at the footpoint of magnetic field lines would be observed at the same geomagnetic coordinates in both hemispheres. However, the Earth's magnetic field is strongly affected by the IMF and the footpoints of magnetic field lines may be displaced in geomagnetic coordinates. An auroral feature appearing in both hemispheres on the same field line is termed *conjugate*, even if the geomagnetic coordinates differ. This is called a location asymmetry and can be explained in terms of the asymmetric forces from the IMF on the magnetosphere, causing field lines that where not originally together, to reconnect in the tail (see Chapter 2.1.4). *Non-conjugate aurora* is defined as aurora on a given field line, appearing in one hemisphere but not the other or significantly brighter in one hemisphere [*Østgaard et al.*, 2004].

Several studies have focused on the aurora in the conjugate regions of the two hemispheres. The fist systematic study was done by *DeWitt* [1962], using All-Sky cameras. Later *Sato et al.* [1998] reported both conjugate and non-conjugate auroral features at the two geomagnetically conjugate stations Syowa (southern hemisphere) and Husafell (northern hemisphere). *Stenbaek-Nielsen and Otto* [1997] reevaluated airborne all-sky camera data, previously presented by *Stenbaek-Nielsen et al.* [1972], and described observations of non-conjugate aurora. Simultaneous satellite imaging of the aurora in both hemispheres was first possible with the Dynamic Explorer 1 (DE1) and Viking satellites [*Craven et al.*, 1991; *Pulkkinen et al.*, 1995]. More recently, a number of conjugate studies have increased our knowledge about the global aurora, using the images provided by the Polar and IMAGE satellites [e.g. *Laundal and Østgaard*, 2009; *Østgaard*, 2005; *Østgaard et al.*, 2004, 2007].

As the aurora is mainly caused by precipitating electrons along the magnetic field lines, upward field aligned currents are associated to auroral features [*Frey et al.*, 2001]. Based on numerous observational studies of non-conjugate aurora *Østgaard and Laundal* [2012] suggest that asymmetries in the auroral location or intensity are related to asymmetric currents and propose three mechanisms for the generation of these. They are described in detail in their paper and the mechanisms will only briefly be summarized here.

1. *Hemispheric differences of the Solar Wind dynamo induced currents*
   The difference in the magnetic tension force on the newly opened field lines with a footpoint in one hemisphere induces currents of different magnitude for the two hemispheres. For a positive IMF B_x this is apparent in Figure 2.7, where the tension force indicated by green arrows is larger in the southern hemisphere on the field lines numbered *3*. In the reference frame of the Earth this is observed as a current opposing the electric field set up by the solar wind. *R1* are believed to partly connect to this part of the magnetosphere, and consequently the ionospheric current closing this system is stronger in the southern hemisphere for $B_x > 0$, possibly introducing auroral asymmetries.

2. *Penetration of the IMF B_y into the closed magnetosphere*
   The penetration of an IMF B_y component into the Earth's magnetosphere is

described and sketched in Chapter 2.1.4.1. From consideration of *Ampere's law* one can argue that a pair of interhemispheric currents are induced mapping to different regions in the two hemispheres.

3. *Conductivity differences in conjugate regions*
   As a result of the angle between the Earth's rotation axis and the dipole axis the two hemishperes are exposed differently to the radiation from the Sun. Figure 2.2 illustrates this. This leads to a difference in ionization in the two hemispheres an consequently a difference in the conductivity. The summer hemisphere will have a larger conductivity than the winter hemisphere. This may lead to a difference in the *R1* currents and non-conjugate aurora in the dusk sector of the hemisphere. Currents from the sunlit hemisphere are believed to close through the winter hemisphere on field lines located in regions having a conducting-gradient, such as the terminator.

Reistad et al. [2013] identified 15 non-conjugate auroral features from a 19 hour data set of conjugate images from Polar and WIC. They categorized the individual observations in terms of these three mechanisms. These identified events of observed non-conjugate aurora form the observational basis of this thesis.

3 Data and Instrumentation

In the following Chapter we give an overview of the instruments used to collect the data utilized in this thesis. The main instruments are two far ultra violet cameras on board the satellites IMAGE and Polar, and the ground based magnetometers part of the SuperMAG network. We also use solar wind data obtained by the Advanced Composition Explorer (ACE) satellite.

3.1 Solar Wind data

Processes in the Earth's magnetosphere are closely linked to the solar wind and the embedded IMF. Thus, monitoring the properties of the solar wind is essential in understanding the solar wind - magnetosphere coupling. In the present thesis, measurements of the IMF from the ACE satellite are utilized through the OMNI database.

ACE was launched August 25, 1997 and is currently orbiting the Earth - Sun liberation point, around 240 R_E sunward of Earth [*Stone et al.*, 1998]. Measurements of the IMF at ACE, are obtained from the MAG instrument consisting of two triaxial fluxgate magnetometers mounted on booms 4.19m off center from the spacecraft [*Smith et al.*, 1998]. Because ACE is located upstream of the magnetosphere in terms of the solar wind, it is necessary to time-shift the data in order to combine the correct IMF data with the measurements obtained at Earth. Several methods exist for calculating the time-shift [e.g. *Weimer*, 2003]. The 1 minute resolution IMF data used in this thesis is time-shifted taking into account the speed of the Earth's orbital motion, the exact position of the spacecraft and solar wind speed[*King and Papitashvili*, 2005]. It is obtained from NASA's Space Physics Data Facility, http://omniweb.gsfc.nasa.gov.

3.2 SuperMAG

The geomagnetic field of the Earth is disturbed by currents flowing in the near Earth space, which are a result of the solar wind - magnetic field - ionosphere coupling. As described in Chapter 2.2, the currents generate magnetic fields, described by Biot-Savarts law (Equation 2.10), that are related perturbations to the Earth's magnetic field. Using ground based magnetometers, it is possible to measure the induced magnetic disturbances by these currents, in the Earth's magnetic field. In the following we introduce the network of ground magnetometer stations and the data product used in the present thesis.

SuperMAG is a collaboration of organizations and agencies operating ground-based magnetometers. The network consists currently of more than 400 magnetometers spread all over Earth. Figure 3.1 shows a geographic map of all SuperMAG magnetometer stations.

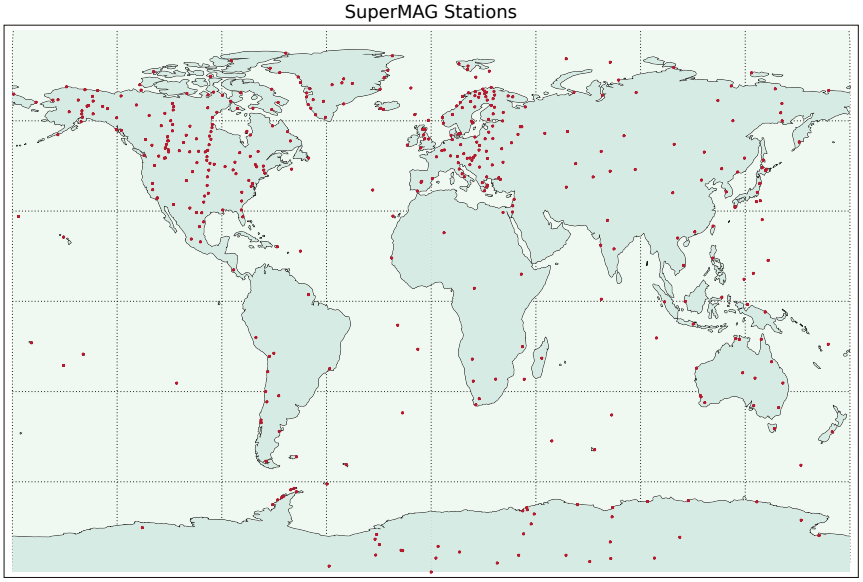

Figure 3.1: Map projection with the position of all SuperMAG stations indicated in geographic coordinates. Each station is indicated by a red dot.

The raw data from the magnetometers come in a variety of formats, coordinate systems, units, sampling rates etc., from the various stations. This is very impractical for global studies. The data used in this thesis is processed extensively by the SuperMAG initiative to provide a more unified data set. The following four steps are a summary of this rather intricate process, outlined in detail by *Gjerloev* [2012]; (1) re-sampling to 1-min time resolution, (2) validation of data, (3) rotation into a common reference system, and (4) subtracting the baseline.

The purpose of subtracting the baseline is to perform a separation of sources so that the perturbations can be studied separately from the general magnetic field of the Earth. As the Earth's field varies, the determination and subtraction of the baseline from the data are performed in three steps from one full year of observations. The

first step is to subtract diurnal variations, the second to remove yearly trends and the third to subtract any known local residual offset from the rotated data set. In this, the baseline subtraction used for the SuperMAG data set differs from the traditional methods of using a Quiet Day Curve (QDC) and as a result avoids all the difficulties associated with identifying the quiet days. *Gjerloev* [2012] argues that there is no objective way to evaluate this method compared to other methods, as there are no observations independent of the processing technique. That is, we do not have a set of truths or facts to compare with. Thus, it is not possible to determine which method is the better or more precise at subtracting the general background magnetic field. The advantage of SuperMAG data is that the background subtraction is performed in the same way for all stations.

The coordinate system used by the SuperMAG initiative is the NEZ local magnetic coordinate system, where N is local magnetic North, E is eastward, perpendicular to north, and Z is towards the Earth's center and completes the right handed system. The definition of this system is explained further in Chapter 4.2.2. Later in this thesis both the Modified Apex coordinate system and the similar AACGM coordinate system will be used to visualize the data. The transformation between the systems is explained in Section 4.2.

3.2.1 Geomagnetic indices

The Auroral Electrojet indices, defined and developed by *Davis and Sugiura* [1966], reflect a measure of the global electrojet activity. Twelve ground magnetometer stations distributed in local time in the auroral oval, are used to calculate the three indices, *AL, AU* and *AE*. The maximum and minimum horizontal magnetic perturbation field at an instant of time give the AU and AL indices, and reflect a measure of the eastward and westward electrojets, respectively. The AE index at any time is defined as the separation between the upper and the lower envelopes (AU and AL) of that instant. In the present study we use the AE index as a measure of the geomagnetic activity.

The *Sym-H* index is derived from six ground magnetometer stations at low latitudes. It is essentially equivalent to the widely used *Dst* (Disturbed storm time) index first introduced by *Sugiura* [1964]. The *Sym-H* index is calculated as the average southward component of the Earth's horizontal magnetic field and is a measure of the large scale behavior the ring current around the Earth with a 1-minute time resolution [*Wanliss*, 2005; *Wanliss and Showalter*, 2006]. In the present thesis the classification by *Gonzalez et al.* [1994] are adopted to place measurements of the *Sym-H* index in context. Thus, for a typical substorm the values of the *Dst*/*Sym-H* index fall between -30nT and -50nT.

Both indices are obtained from NASA's Space Physics Data Facility `http://omniweb.gsfc.nasa.gov`, as for the IMF data from ACE. The data is provided by the World Data Center for Geomagnetism, Kyoto `HTTP://wdc.kugi.kyoto-u.ac.jp/index.html`.

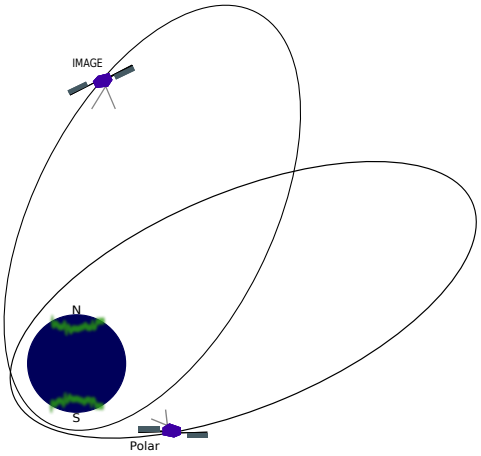

Figure 3.2: IMAGE and Polar spacecraft orbit.

3.3 IMAGE and Polar satellites

The conjugate images of the northern and southern hemispheres used in this thesis are obtained by instruments on two NASA satellites, the Imager for Magnetopause-to-Aurora Global Exploration (IMAGE) satellite and the Polar satellite. The instruments will be described below. During the years 2001 and 2002 their positions were such that simultaneous imaging of both hemispheres was possible. Figure 3.2 shows a sketch illustrating their orbits during those years.

The purpose of the IMAGE mission was to image the Earth's magnetosphere using techniques of ultra violet imaging, neutral atom imaging, and radio plasma imaging [*Burch*, 2000]. During its lifetime it provided data to investigate the global structure and dynamics of the magnetosphere. The satellite was launched in March 2000 in a highly elliptical orbit at 90° inclination with an apogee at an altitude of $7R_E$ and perigee at 1000km [*Burch*, 2000]. IMAGE completed one orbit every 14.2 hours and provided data until December 18th 2005.

The Polar satellite was part of the Global Geospace Science Program (GGS) which is in an element of the International Solar-Terrestrial Physics (ISTP) campaign. In addition to Polar, a second satellite, WIND, was part of the GGS program. The goal of the ISTP program was to improve the current understanding of the energy, mass and momentum transports in the near Earth space [*Acuña et al.*, 1995]. The Polar satellite was spinning at a rate of 10 revolutions per minute. However, most of the instrumentation on board Polar was mounted on a despun platform. It was launched into an elliptic orbit with 90° inclination in February 1996. Apogee of the orbit was at $9R_E$ while the perigee was at $1.8R_E$ [*Acuña et al.*, 1995]. Polar completed one orbit every 17.5 hours and provided data until April 2008.

3.3.1 IMAGE Far Ultraviolet Wideband Camera

On board the IMAGE satellite were three Far Ultraviolet (FUV) instruments. The Wideband Imaging Camera (WIC) [*Mende et al.*, 2000a], the Spectrographic Imager (SI) and the GEO photometer [*Mende et al.*, 2000b]. The SI, a monochromatic im-

ager had filters at two different wavelengths. The SI-13 filter was focused at 135.6 nm for observation of line emissions from atomic oxygen. This emission line is produced mainly by electron precipitation with some contribution from proton precipitation. The SI-12 filter made observations of the Doppler-shifted Lyman-α emissions from hydrogen produced by precipitating protons only. The wavelength pass-band of this filter was from 119-126 nm, but was blocked at 121.566 and 120.0 to only observe the Doppler-shifted emissions from the interaction of the precipitating protons with electrons [*Mende et al.*, 2000c]. The geocoronal photometer consisted of three photometers designed to measure the geocoronal Ly-α surrounding Earth [*Mende et al.*, 2000b].

In this thesis we use the measurements from the WIC imager only. The primary objective of the WIC is to provide broadband ultraviolet images of total terrestrial aurora intensity over the entire polar region [*Mende et al.*, 2000c]. The camera observes a few N-lines in the Lyman-Birge-Hopfield (LBH) emission band of the far ultraviolet aurora with a spectral wavelength range from 140 - 190 nm, with peak response at 150nm [*Mende et al.*, 2000c]. Due to the rotating platform on which the imager is mounted, the Earth sweeps through the FOV of the camera for approximately 10 seconds for every revolution. During this time a set of 300 images is taken, each with an exposure time of 0.033 seconds. The rotating motion causes the images to be slightly distorted. To ensure minimal resolution loss and compensate for the motion of the satellite, every image is distortion-corrected and images are then superimposed on one another. This method of processing the data is called Time Delayed Integration (TDI) and results in one image per revolution of the satellite [*Mende et al.*, 2000a]. As the on board storage and the down link are limited this is done in situ before the final image is transmitted.

To map the downloaded images onto the Earth we use the Fuview software, developed by the FUV team at Space Science Laboratory, Berkeley USA. This software is an IDL based library of routines to map and display data from all three cameras on the IMAGE satellite. As the satellite is most of the time located several R_Es from Earth, even a small inaccuracy in the pointing of the imagers would lead to large errors in the mapping onto Earth. To avoid this, the pointing is determined by adjusting the images such that the stars in the field of view (FOV) of the camera align with the predicted position of those known stars. This calibration was done once for every day of data using this software. During the IMAGE mission several pieces of the Radio Plasma Imager antenna broke of, which resulted in a wobbling motion [*Frey*, 2010]. The error this motion produced was not possible to correct for using the star-alignment method. The data used in this thesis is adjusted as good as possible and the introduced error is not believed to be significant for data used in this thesis [*Laundal*, 2010; *Reistad*, 2012].

3.3.2 Polar VIS Earth Camera

There are three cameras on board the Polar satellite. Two of these are designed to image the nighttime aurora oval at visible wavelengths with high spatial resolution. They share some of the same optics but have different spatial resolution. The primary objective of the third camera was to monitor the other two cameras FOV with respect to the sunlit Earth [*Frank et al.*, 1995]. In this study we will use this

Satellite	**IMAGE**	**Polar**
Perigee	$1000km$	$1.8R_E$
Apogee	$7R_E$	$9R_E$
Orbit time	$14.2h$	$17.5h$
Lifetime	Mar 2000 - Dec 2005	Feb 1996 - Apr 2008
Revolution time	$0.5 \pm 0.01rpm$	$10rpm$
Camera	**WIC**	**VIS Earth**
Wavelength	140 -190nm	124 - 149nm
Cadence	$123s$	$54s$
Integration time	$10s$	$32.5s$
Field of View	$17° \times 17°$	$20° \times 20°$
Resolution	256×256	256×256

Table 3.1: The main characteristics of the satellites and the cameras on board used in this thesis [*Acuña et al.* [1995], *Frank and Sigwarth* [2003], *Frank et al.* [1995], *Mende et al.* [2000a],b,c].

third camera, namely the VIS Earth camera, as it has a large FOV ($20° \times 20°$) and is pointed at the Earth at all times. To achieve this, the camera is mounted on a despun platform. Instead of one image per revolution of the satellite the theoretical rate of images can be as low as 12 seconds [*Frank and Sigwarth*, 2000]. However, for the dataset used in this thesis the nominal cadence was 54 seconds [*Frank and Sigwarth*, 2003]. VIS Earth camera is equipped with a broadband filter with a spectral wavelength range of 124 nm - 149 nm that is in the UV range [*Frank et al.*, 1995]. The wide bandpass encompasses both the atomic oxygen line at 130.4 nm and some of the LBH-band. According to *Frank and Sigwarth* [2003] the atomic oxygen emissions at 130.4 nm are dominant and give 83% of the total response.

The determination of pixel position for the VIS Earth camera is done by observing the emissions from known stars slowly passing through the FOV. The wobble of the spacecraft, induced by the center-of-mass not being at the rotational axis, was corrected for by on board software which shuttered the camera synchronized with the spacecrafts spin [*Frank and Sigwarth*, 2000].

3.3.3 Comparison of Far Ultra Violet cameras

As specified in Chapter 3.3.2 and 3.3.1 the spectral bandpass for the WIC imager and the VIS Earth camera are 140 - 190 nm and 124 - 149 nm, respectively. Furthermore, *Frank and Sigwarth* [2003] state that the response in the VIS Earth camera is dominated by 83% by the emissions from the 130.4 nm OI line, while the remaining 17% are due to the OI emission at 135.6 nm and the N_2 LBH band emissions. This means that the cameras observe different auroral emissions, and the intensity in counts of the images can not be directly compared. Figure 3.3 is adopted from *Frey et al.* [2003] and emphasizes the difference in spectral response of the two cameras. The issue has been addressed by several studies [*Frank and Sigwarth*, 2003; *Frey et al.*, 2003; *Laundal and Østgaard*, 2009; *Reistad et al.*, 2013]. In the following some of the arguments presented in those studies are listed.

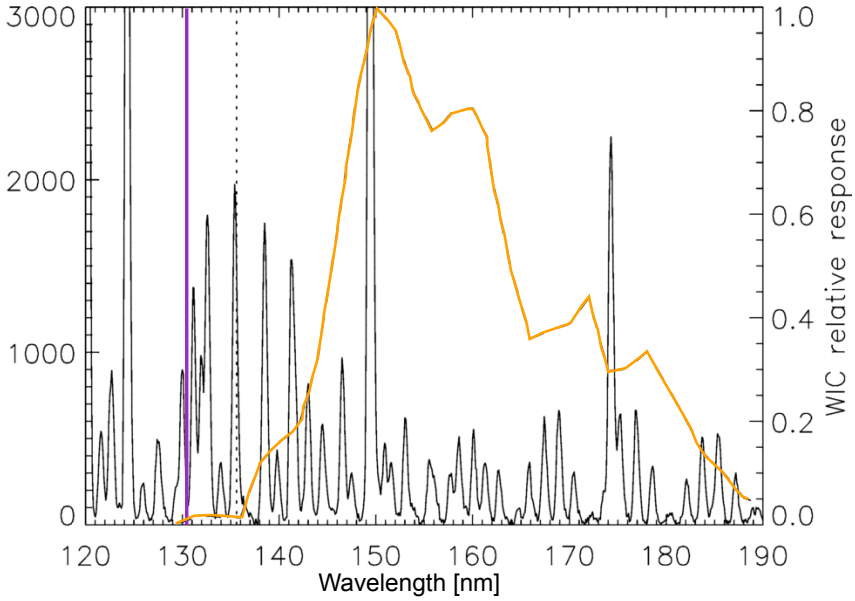

Figure 3.3: Laboratory spectrum of FUV emission from N_2 [*Ajello and Shemansky*, 1985] is shown by the solid black line. WIC relative spectral response is indicated by the orange line and the wavelength, 130.4 nm, where the VIS Earth has 83% of its total response is indicated by the purple line. The dotted black line marks the second OI line at 135.6 nm. Figure adopted from *Frey et al.* [2003].

The FUV Lyman-Birge-Hopfield (LBH) emissions observed by the WIC imager are primarily N_2 lines produced by the direct impact of electrons and two atomic nitrogen lines produced by secondary electrons. Atmospheric oxygen, O_2, is an absorbing agent and can affect the FUV emissions on their way out of the atmosphere, depending on the wavelength. Emissions from high energy electrons from deeper in the atmosphere have a thicker layer of absorbing O_2 to penetrate, above. It is possible to relate the observed intensities to the altitude of the emissions and by that to the energy of the precipitating electrons. The absorption of the emissions by O_2 thus reduces the intensity of the LBH emissions observed by the WIC imager [*Frey et al.*, 2003]. For high energy precipitation, the emissions observed by the WIC imager are more reduced than the atomic oxygen emissions observed by the VIS Earth camera. Another aspect that could introduce further differences between the cameras is the effect of sunlight and the heating of the atmosphere. Heating of the atmosphere affects the scale height of N_2 more than the scale height of O_2, so in illuminated areas the reduction by O_2 is less effective. Hence, the areas illuminated by the Sun are likely to have slightly brighter auroral emissions in the LBH band than the areas in darkness, given the same electron precipitation. As mentioned earlier, molecular O_2 reduces the LBH band more efficiently than the the OI lines, so this effect of the sunlight altering the scale heights of atmospheric constituents is more prominent in the WIC camera.

4 Methodology

4.1 UV image processing

Due to the tilt angle λ_{tilt}, of the Earth relative to the Sun the two hemispheres are exposed to an unequal amount of daylight unless the angle is close to zero, $\lambda_{tilt} \to 0$. Most of the time this is not the case, and the illuminated area in one hemisphere extends further towards the night side than in the other. Especially in the summer hemisphere this daylight contamination is a significant fraction of the total observed intensity and makes comparison difficult.

Since the Earth is approximately spherical, the sunlight induced emissions differ depending on where on the surface they are observed. This means that a geographic area of a certain size close to the equator will have a different amount of daylight contamination than an equally sized area at higher latitudes, depending on the area illuminated by the Sun. An area illuminated by the Sun is always perpendicular to the Sun-Earth line. The size of the area is proportional to the cosine of the solar zenith angle, $\cos\theta_{SZA}$, the angle made by the vertical and the line to the geometric center of the Sun. Similarly, the same area as observed by a pixel from the cameras is dependent on the angle of the vertical and the line to the camera. We call this angle the satellite zenith angle, θ_{DZA}. The intensity observed by each pixel is then proportional to $\frac{1}{\cos\theta_{DZA}}$. Since we are looking at emissions from a volume in the atmosphere, this angle, unless it is zero, results in a larger volume observed by a pixel. This means that the observed emissions from an area is dependent on the size of the observed volume, which in turn is dependent on the solar zenith angle and the satellite zenith angle. Figure 4.1 illustrates this concept, with area S1 and area S2 indicating the differently sized areas as seen from the Sun. The same effect appears for the area as seen from the satellite and is indicated by the red line on the Earth's surface, showing the area observed by one pixel. We see that as θ_{DZA} increases, the pixel extends over a larger area and thus the volume of atmosphere above this area also increases. In addition, the solar zenith angle of pixel 1 is smaller, exposing it to a greater amount of direct solar radiation. Hence, the intensity observed by pixel 1

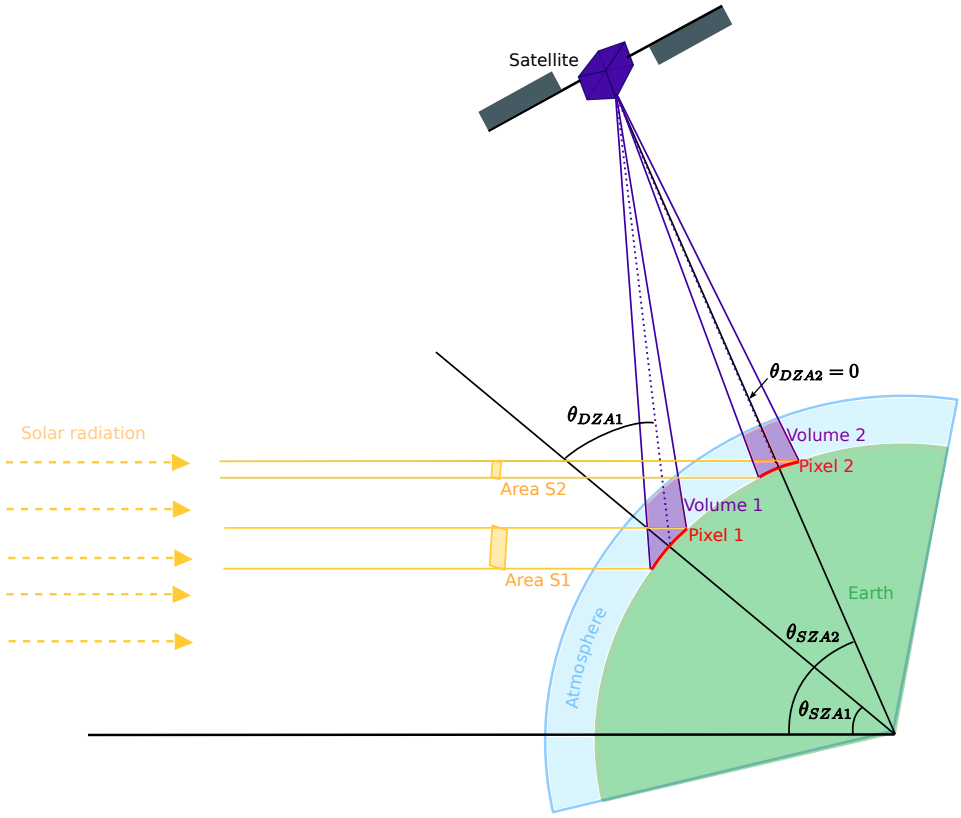

Figure 4.1: The effect of a slant viewing angle from the satellite for two pixels is illustrated. Volume 1 observed by pixel 1 is larger than volume 2 observed by pixel 2 due to the larger satellite zenith angle , $\theta_{DZA1} > \theta_{DZA2}$. Consequently the observed intensity of pixel 1 is affected by a greater amount of dayglow contamination as the solar radiation acts on a larger volume.

(from volume 1), is affected to a greater degree by both direct solar radiation and dayglow emitted inside the volume. Both factors increase the amount of dayglow-contamination in pixel 1 compared to pixel 2.

From this analysis we obtain a relation between the observed intensity of every pixel to the solar zenith angle and the satellite zenith angle, θ_{SZA} and θ_{DZA}. For a given pixel with given θ_{SZA} and θ_{DZA} the observed intensity is:

$$I_{background} = I_0 \frac{cos\theta_{SZA}}{\cos\theta_{DZA}} = I_0 r, \qquad \theta \leq 75^\circ \tag{4.1}$$

where $r = \frac{\cos\theta_{SZA}}{\cos\theta_{DZA}}$.

When making a model for the observed background intensity we take advantage of this relation (Equation 4.1) to some extent. The upper left panel of Figure 4.2, shows the relation of the intensity of selected pixels (with no auroral emissions) relative to the ratio $r = \frac{cos\theta_{SZA}}{\cos\theta_{DZA}}$. For ratios less than zero, the observed background intensity is constant, while for $r \in [0, 3]$ the pixels follow a clear trend. In the calculation of the model, explained in detail in the next section, we try to find an approximation to the observed intensity of every pixel. We will use the examination of the above

relation as a starting point.

To summarize, there are primarily three sources for counts in the images:

1. Auroral emissions
2. Sunlight induced emissions from sunlight illuminating the atmosphere
3. A time-varying instrument noise background affecting all pixels

A significant portion of the total observed intensity comes from the two latter components. To be able to compare larger parts of the image pairs and improve the dynamic range of the aurora imaged, we model this background for every image and subtract it. In the following chapter we describe in detail how we model and subtract the contributions from these.

4.1.1 Dayglow removal technique

The procedure to subtract the dayglow from the images is written in IDL language. First, we select an area in the image well outside the auroral oval. Typically this is from 40° to 52° magnetic latitude and above 80° magnetic latitude. By magnetic latitude we mean Modified Apex coordinates explained in Chapter 4.2.4. For the remaining pixels the ratio of $\frac{cos\theta_{SZA}}{cos\theta_{DZA}}$ is calculated. We plot the intensity of these pixels versus this ratio. The upper left panel of Figure 4.2 shows an example of this. Next, we bin these counts in small ratio bins and calculate the median of every bin, with binsize 0.1. In the next step we interpolate between all calculated median points of each bin, for all ratios of $\frac{cos\theta_{SZA}}{cos\theta_{DZA}}$, including ratios that are inside the auroral oval. By doing this we calculate model-counts for all existing ratios for our image including pixels inside the auroral oval. In the upper left panel of Figure 4.2 this is shown as a red line. Here we also see the uncertainty of our method in the spread of the pixel intensity as a function of the $\frac{cos\theta_{SZA}}{cos\theta_{DZA}}$ ratio. Hence, we have calculated a model-count for the dayglow of every pixel in the image. The upper right panel of Figure 4.2 shows the model-counts plotted in magnetic/MLT coordinates. The original image is shown in the lower left panel of Figure 4.2. Looking at the model (Figure 4.2) we see that most of the dayside is black, meaning that it is saturated. For low ratios ,$r < 0$, the background intensity is constant and is due to the instrument noise. In the upper left panel of Figure 4.2 this is seen in the small blue area centered around 00 MLT, where the only contribution to the signal is from instrument noise. We proceed to subtract the modeled background from the image. The result of this is presented in the lower right panel of Figure 4.2. We are left with only the auroal emissions and some noise, especially towards the dayside. This noise is due to deviations of the model from the actual background. The black line in the images indicate the terminator, i.e. the virtual line across Earth where the solar zenith angle is $\theta_{SZA} = 90°$. However, we note that the contamination of the solar radiation extends further than this as a result of the atmosphere's thickness. As mentioned above, this process removes background emissions induced by the sunlight and by the instrument noise.

A method similar to the one described above is used in *Reistad et al.* [2013] and *Laundal* [2010]. Instead of calculating a median for small bins and interpolation

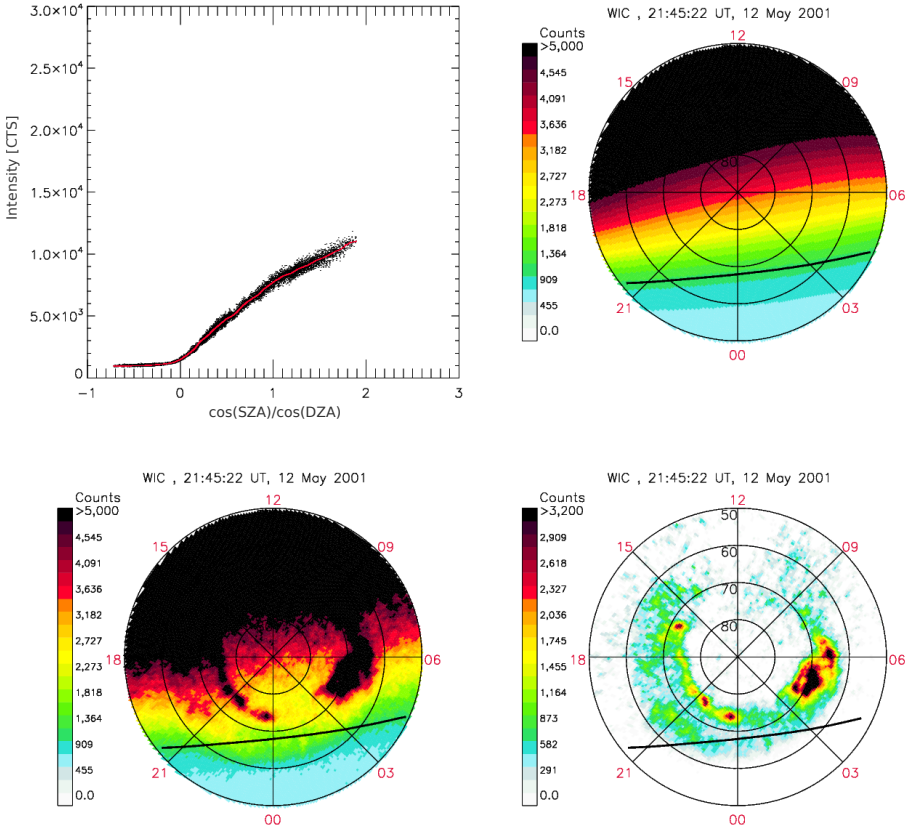

Figure 4.2: Example of the dayglow removal technique applied on all images. The upper left panel shows the intensity in selected background pixels plotted against the ratio $\frac{cos\theta_{SZA}}{cos\theta_{DZA}}$. The red line indicates the modeled background intensity calculated from these pixels. The upper right panel shows the modeled background which we subsequently subtract from the image, shown in the lower left panel, to obtain an image where the auroral emissions are clearly discernible, as shown in the lower right panel.

between them, they use a high order polynomial fitted to the background counts of 30-60 images. By this method, pixels from several images are used simultaneously to calculate the model. Using their method the calculated background is valid for all images used to calculate it, which typically is 60-120 minutes. For the present study we found it difficult to find a good polynomial approximation for all ratios, especially in the area where the selected pixel change from following an apparent constant relation to being more linear. Therefore, we have attempted to improve this method as well as calculate a model for each of the images separately.

4.2 Magnetic Coordinate systems

The structure and dynamics of the ionospheric plasma as well as its motion is a result of the interaction between the solar wind, Earth's magnetic field and the ionosphere. This interaction gives rise to a complex system of electric currents flowing in the magnetosphere-ionosphere system which is highly organized by the Earth's magnetic field. As previously mentioned, currents produce magnetic disturbances that can be

measured on ground. To investigate these perturbations, caused by the ionospheric currents, a frame of reference in which the properties of the magnetic field and the currents can be represented, is needed. In space physics, several coordinate systems can be used to describe the organization of the ionosphere, upper atmosphere and geomagnetic field. Depending on the interest of the study, one coordinate system might be better suitable than the other. Several papers have been published on this topic to give an explanation of the different systems, their derivation and their use, [*Baker and Wing*, 1989; *Emmert et al.*, 2010; *Richmond*, 1995; *VanZandt et al.*, 1972]. For studies of the ionosphere and the horizontally stratified currents associated with aurora the Quasi Dipole coordinates, based on the Apex coordinate system, are useful [*Emmert et al.*, 2010; *Richmond*, 1995]. These will be further explained in Chapter 4.2.4.

The presentation of data is dependent on the reference system used an equal measurements can look very different when displayed in different reference systems. In this thesis we encounter several coordinate systems in which the obtained raw data are presented. As mentioned in Chapter 3.2, the data provided by SuperMAG are in a local magnetic coordinate system, the NEZ-system. Images of aurora from the Polar VIS Earth and IMAGE WIC cameras, are analyzed in Modified Apex coordinates. In this thesis we have transformed the SuperMAG data from NEZ-coordinates to AACGM coordinates, which are very siilar Apex coordinates. Figure 4.3 shows an example of SuperMAG data in NEZ-coordinates and AACGM coordinates, revealing the significance of the reference coordinate system. Another example of how the transformation affects the data set is shown later in Chapter 4.2.6, in Figure 4.10. SuperMAG vectors are displayed in NEZ-coordinates (pink) and AACGM coordinated (blue) on a map in AACGM coordinates. Again the difference is evident.

A detailed description of all coordinate systems used in this thesis is given in Chapter 4.2.
The separate coordinate systems and definitions are explained, as well as the procedure for the transformation between them (Chapter 4.2.6).

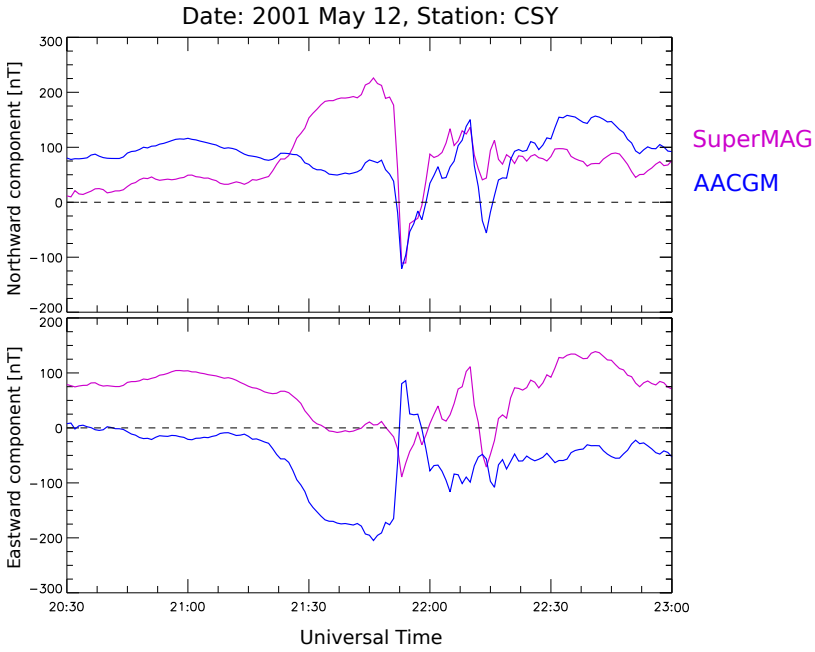

Figure 4.3: Example of data from SuperMAG station CSY plotted in NEZ coordinates (pink) and AACGM coordinates (blue).

4.2.1 Magnetic Local Time

Magnetic Local Time (MLT) is a coordinate which is frequently used in space physics instead of magnetic longitude. It is given as a time and relates the magnetic longitude and the Universal Time (UT) to the point of interest. MLT midnight is where the position P, a magnetic pole (either north or south) and the sun are in the same plane. Figure 4.4 shows a sketch of this.

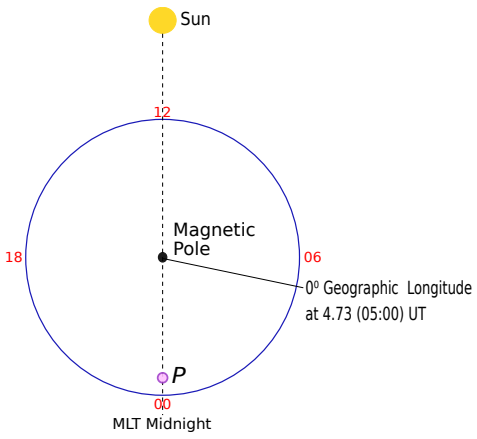

Figure 4.4: Definition of the Magnetic Local Time coordinate.

MLT is defined as

$$\text{MLT} \;=\; \Phi/15 - 4.73 + \text{UT} \tag{4.2}$$

where Φ is the magnetic longitude, UT is universal time given in hours and the constant -4.73 is due to the chosen reference point at magnetic north (0°N, 0°E)

[*Baker and Wing*, 1989]. Then the time is determined in the normal manner where one hour passes for every 15° latitude. Neither seasonal effects nor the variation due to the Earth's position in its orbit around the sun are taken into account in this definition. During the course of a year the sun has an apparent motion along the north-south axis. As a result, the UT and MLT values correspond to different times in the course of a year. Also, due to the eccentricity of Earth's orbit around the Sun, the apparent position of the sun relative to the mean position, varies. As universal time is defined by the mean position of the sun, these variations introduce a possible shift of ±20 minutes over course of a year.

The images from the Polar and IMAGE satellites in this thesis are presented in Modified Apex and MLT coordinates , where we have taken into account the above mentioned variations.

4.2.2 NEZ-coordinates

As mentioned in Chapter 3.2, SuperMAG uses its own local magnetic coordinate system, the NEZ-system. It is defined as follows:

$$\mathbf{B} = (B_N, B_E, B_Z)$$

where N is local magnetic north, E is local magnetic east and Z is towards the center of the Earth. These directions are determined by the data themselves. North is determined to be in the direction of the typical horizontal magnetic field at each station. A 17-day sliding window is used for this, where the local time dependent declination angle is calculated by

$$\theta = \theta(t) = \arctan\left(\frac{B_1}{B_2}\right)$$

where B_1 and B_2 are the horizontal components of the magnetic field in the old coordinate system. The determination of typical values for SuperMAG data is not straight forward and is described in detail by *Gjerloev* [2012]. Using the declination angle θ, the data is rotated such that the typical direction of the magnetic field is in the northward direction. The eastward vector, E, is then defined to be perpendicular to N in an eastward direction. The Z component is defined as positive towards the center of the Earth. Figure 4.5 illustrates this. The original coordinate system is an example and only meant to illustrate this procedure. It is assumed that offsets, due to local magnetic phenomena such as geological variations, are either small or known [*Gjerloev*, 2012].

In this thesis we make the assumption that the N-direction calculated by SuperMAG at the stations is in the direction along the Earth's magnetic field as described by the International Geomagnetic Reference Field model.

4.2.3 International Geomagnetic Reference Field

The International Geomagnetic Reference Field (IGRF) is a mathematical model of the Earth's internal magnetic field in the absence of external influences. The magnetic field of the Earth originates in the Earth's interior and changes over time, with

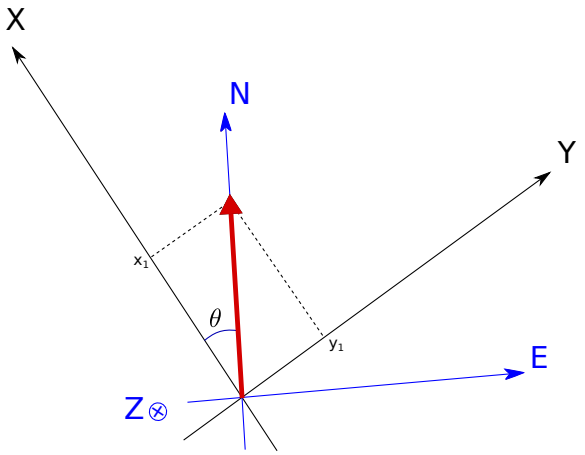

Figure 4.5: Sketch illustrating the determination of the local magnetic coordinate system used by SuperMAG. The red arrow indicates the typical value horizontal vector of a 17-day window, in the XY coordinate system. The local magnetic NEZ-system is defined such that north is in the direction of the typical horizontal field during that time. The NEZ-coordinat system is indicated by the blue grid.

timescales from a few years to decades and more. As a result the IGRF model has to be updated regularly. It is revised usually every five years by the International Association of Geomagnetism and Aeronomy (IAGA).

The field itself roughly resembles that of a dipole. This is a simplification and the IGRF model would be more suitable as it describes the more complex morphology of the field. Several well known features, like the South Atlantic Anomaly, are encompassed by IGRF. *Finlay et al.* [2010] show the declination, inclination and total intensity of the field at Earth's surface in 2010 as the IGRF model describes it. The differing features as compared to a dipolar field become apparent here. Our Figure 4.6 is adapted from their paper to give an indication of the field model and arrangement of the coordinate system aligned with it. In the figure the differences between the field as calculated by the IGRF model and a dipolar magnetic field become clear. The top panel shows the declination, the angle between magnetic north and true north, as given by the model. We see here that instead of two agonic lines (lines where true and magnetic north are on the same line, i.e. the declination is zero), the IGRF model magnetic field has three. One crossing America, one crossing southeast Asia and Australia and one that goes across Africa before looping back over Siberia and going back to the north pole. The inclination, the angle between the magnetic field and the horizontal, is shown in the second panel and the total field intensity is shown at the bottom. The low field intensity in South America is called the South Atlantic Anomaly. In this model the direction of the components are described as follows: X points to geographic north, Y points to geographic east and Z vertically down. In addition the horizontal intensity H, declination D, the inclination I and the field strength F, in nT are;

$$H = \sqrt{X^2 + Y^2} \tag{4.3a}$$

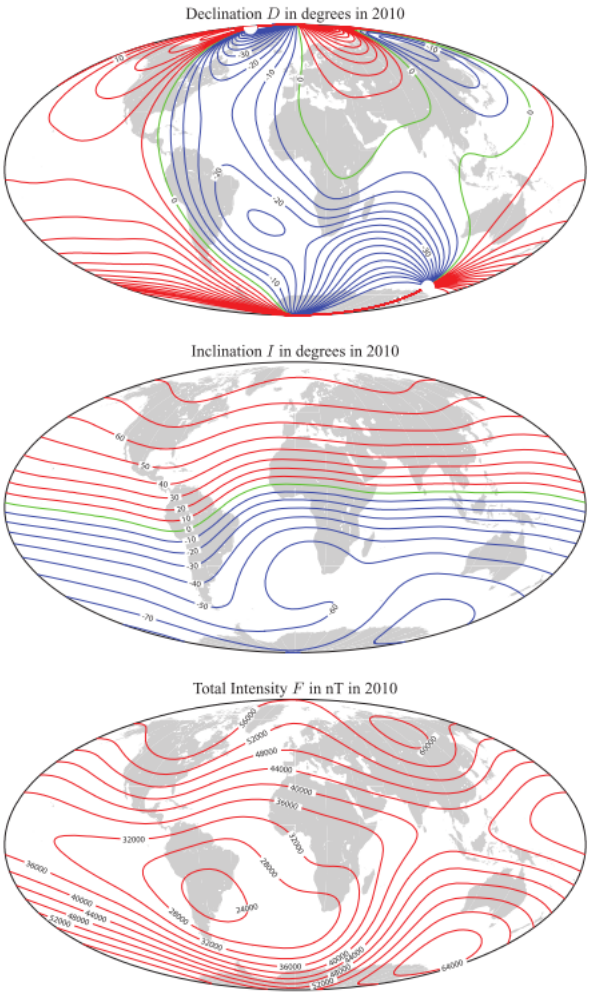

Figure 4.6: Magnetic Field declination, inclination and field strength in 2010, as calculated by the IGRF model. Zero line is shown in green, positive contours in red and negative contours in blue. Figure adapted from *Finlay et al.* [2010].

$$F = \sqrt{X^2 + Y^2 + Z^2} \tag{4.3b}$$

$$D = \arctan(X/Y) \tag{4.3c}$$

$$I = \arctan(Z/H) \tag{4.3d}$$

In general the field can be represented by the scalar potential $\mathbf{B} = -\nabla V$. For IGRF this potential is expressed in terms of a spherical harmonic with Gaussian coefficients:

$$V(r,\theta,\phi,t) = a\sum_{n=1}^{N}\sum_{m=0}^{n}\left(\frac{a}{r}\right)^{n+1}[g_n^m(t)\cos m\phi + h_n^m(t)\sin m\phi] \times P_n^m(\cos\theta) \tag{4.4}$$

where r is the distance from the center of the Earth in km, $a = 6371,2$km is the spherical radius of Earth, θ is the geocentric co-latitude (90° - latitude), and ϕ is longitude going east [*Finlay et al.*, 2010]. $P_n^m(\cos\theta)$ are the Schmidt quasi-normalized associates Legendre functions of degree n and order m. The Gauss coefficients, g_n^m

and h_n^m, are given with a time interval of five years and are based on data. For the years from 2010 to the present, the coefficients are derived using linear interpolation. *Finlay et al.* [2010] describe the model in detail and provide a complete record of the Gauss coefficients from 1900 to 2010 at five year intervals for the main field. For the time span from 2010 to 2015 the predicted coefficients are given in units of $nTyr^{-1}$.

Dr. Nikolai Tsyganenko has developed a set of FORTRAN routines for various models of the Earth's internal and external magnetic field. As a part of this, he has written a library of routines for the transformations between several coordinate systems commonly used in geophysics. He provides these in a software package, GEOPACK, that can be downloaded for free from his homepage [*Tsyganenko*, 2014]. IN GEOPACK there are subroutines to calculate the IGRF magnetic field model at a given geographic position. However, as the code is provided in the FORTRAN syntax we also make use of the Dynamic Link Module, IDL GEOPACK DLM, which enables us access to the GEOPACK in the Interactive Data Language (IDL) [*Korth*, 2014]. This is written and made available by Haje Korth at John Hopkins University, Applied Physics Laboratory. All the calculations of the IGRF magnetic field model in this thesis are done using this software.

4.2.4 Apex, Modified Apex and Quasi Dipole coordinates

For studies of the high-latitude magnetometer data in combination with conjugate studies of the aurora in both hemispheres [e.g. *Laundal and Østgaard*, 2009; *Laundal et al.*, 2010; *Østgaard et al.*, 2007; *Reistad et al.*, 2013], it is essential to have a coordinate system based on a realistic model of the magnetic field, in which the data can be presented. The apex-based, Quasi Dipole coordinate system is well suited for this as it based on the IGRF magnetic field model and specially useful for studies of horizontally stratified phenomena (e.g. auroral electrojets etc.) [*Emmert et al.*, 2010; *Richmond*, 1995]. In Apex, Modified Apex and Quasi Dipole coordinates, a point in space is described by the coordinates in terms of A, the apex radius. The Apex of a field line is the point in space where the field line is at its highest altitude, h_A, above Earth. The distance to this point is the apex radius in units of R_E, and defined as:

$$A = 1 + \frac{h_A}{R_E} \tag{4.5}$$

The latitude, λ_A, and longitude, ϕ_A, are given by:

$$\lambda_A = \pm \arccos(A^{-\frac{1}{2}}) \tag{4.6a}$$

$$\phi_A = \arcsin\left[\frac{\cos\lambda \sin(\phi - \phi_0)}{\cos\lambda_D}\right] \tag{4.6b}$$

where $\lambda_D = \arcsin\left[\ \sin\lambda \sin\lambda_0 + \cos\lambda \cos\lambda_0 \cos(\phi - \phi_0)\ \right]$ is the dipole latitude in terms of λ and ϕ, the geographic latitude and longitude of the apex, and λ_0 and ϕ_0, the geographic latitude and longitude of the north pole of the dipole field [*VanZandt et al.*, 1972]. h_A is the altitude above the surface of the oblate spheroidal Earth with semimajor axis $r_E = 6378.165$ and eccentricity $\epsilon = 1/298.25$. So to find the Apex coordinates of a point at given geographic position at an altitude above Earth, we trace the magnetic field line as given by the IGRF model, described in Chapter 4.2.3, and follow it to its apex. We then follow a virtual dipolar magnetic field-line

back down towards the surface of the Earth. Figure 4.7 illustrates this. From a starting point P_0 we follow the green line indicating the IGRF magnetic field line to the apex. From there we follow the purple dipole field line back to the surface of the Earth. The latitude and longitude are then calculated from the geographic position of this point, P_A. The third coordinate of the system can be chosen as any quantity that varies along a field line [*Richmond*, 1995]. *VanZandt et al.* [1972] suggested the altitude H, whereas *Richmond* [1995] use the magnetic potential V_0.

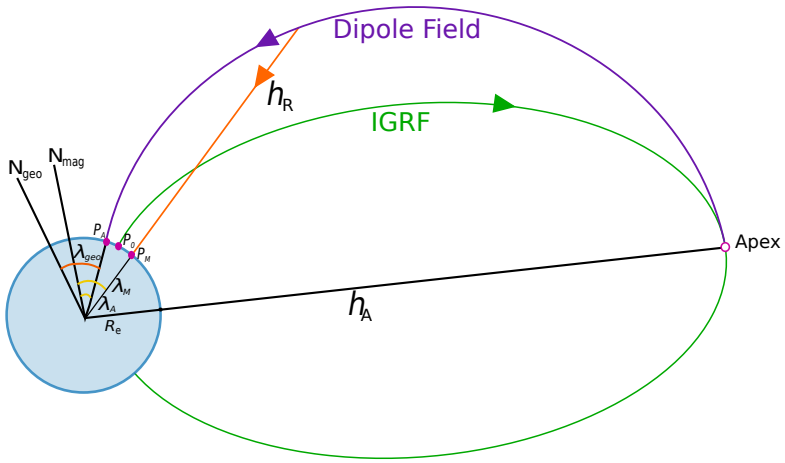

Figure 4.7: Conversion from geographic coordinates is done by tracing the IGRF magnetic field line to its Apex and defining the apex latitude in terms of R_E and h_A as in Equation 4.6a.

From this definition we see that the Apex latitude is a function of the Apex radius only, and therefore all points of equal A have the same latitude. The sign indicates the northern hemisphere for all positive values and the southern hemisphere for all negative values. So for all points on a IGRF field line the apex coordinates, λ_A and ϕ_A, are constant by this definition. Points along a field line with footpoints in both hemispheres would have symmetric coordinates if no external influences where present.

For modified Apex coordinates this is almost identical except for a constant reference altitude h_R, to which the dipolar field line is traced back to instead of the Earth's surface. In Figure 4.7 this is indicated by the orange line. The field line tracing stops at the reference height h_R. From there a vertical line is followed to the point P_M at the surface of the Earth, where the modified apex latitude is calculated. The modified form of the latitude is

$$\lambda_m = \pm \arccos\left(\frac{R}{R_E + h_A}\right)^{\frac{1}{2}} \tag{4.7}$$

where $R = R_E + h_R$, and the subscript m denotes modified apex coordinates.
This is used for the images from WIC and VIS Earth, which are presented in Modified Apex coordinates at a reference height of 130 km.

For these calculations we use a slight modification of the Modified apex coordinate system called Quasi-Dipole Coordinates. It differs from Modified Apex in that there is no reference height associated with it. Instead the altitude h is used as the third coordinate. The coordinates are defined as follows:

$$\lambda_q \equiv \pm \arccos\left(\frac{R_E + h}{R_E + h_A}\right)^{\frac{1}{2}} \tag{4.8}$$

which is identical to equation 4.7 except for h which now is the altitude rather than a reference height h_R and also gives the third coordinate of the system, [*Richmond*, 1995]. The longitude is as before $\phi_q = \phi_A$. With λ_q defined in this manner, lines of constant latitude extend vertically from the surface of the Earth. This implies that λ_q varies along a magnetic field line, unlike in Modified Apex coordinates where λ_m is constant along a field line.

For these coordinates *Richmond* [1995] provides a set of equations for the calculation of the magnetic perturbations on ground, produced by overhead equivalent currents in the ionosphere. The perturbations rotated by 90° are nearly proportional to these currents and so the currents direction and magnitude can be derived from measurements of the magnetic perturbations. We calculate base vectors for this system and apply them in the transformation between the coordinate systems explained in Chapter 4.2.6. The base vectors are given in Equations (6.7), (6.8) and (6.9) by *Richmond* [1995] and are as follows:

$$\boldsymbol{f_1} = -(R_E + h)\boldsymbol{k} \times \nabla\lambda_q \tag{4.9}$$

$$\boldsymbol{f_2} = (R_E + h)\cos\lambda_q \boldsymbol{k} \times \nabla\phi_q \tag{4.10}$$

$$F = \boldsymbol{f_1} \times \boldsymbol{f_2} \cdot \boldsymbol{k} = (R_E + h)^2 \cos\lambda_q \boldsymbol{k} \cdot \nabla\phi_q \times \nabla\lambda_q \tag{4.11}$$

where F is a scaling factor, $\nabla\lambda_q$ is the gradient of the latitude and $\nabla\phi_q$ is the gradient of the longitude. Considering these gradients it becomes apparent that this is a non-orthogonal coordinate system. We will later calculate these gradients using the standard definition of a gradient in spherical coordinates. This is a reasonable assumption if the base vectors $\boldsymbol{f_1}$ and $\boldsymbol{f_2}$ do not vary much over the area where the gradient is calculated. Figure 5 by *Richmond* [1995] shows a plot of $\boldsymbol{f_1}$ and $\boldsymbol{f_2}$ projected on a geographical grid. It illustrates that the spacial variation is indeed small considering a limited area. Our Figure 4.8 is a duplicate of this figure and included here to affirm our assumption.

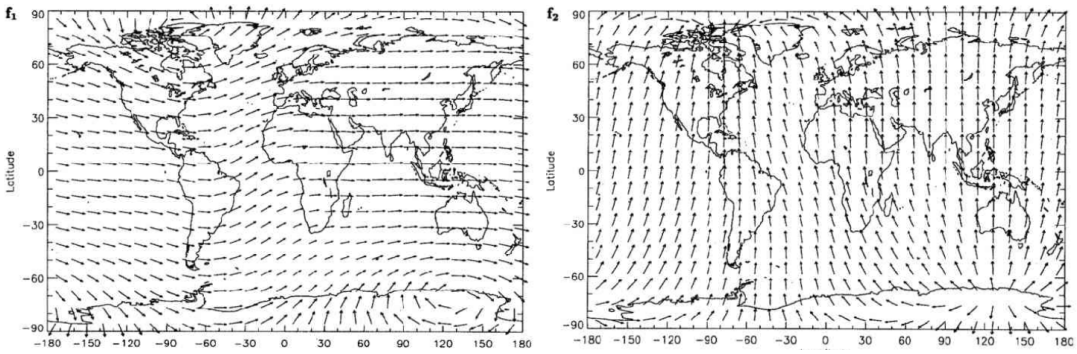

Figure 4.8: Figure adopted from *Richmond* [1995] showing the spatial variation of $\boldsymbol{f_1}$ and $\boldsymbol{f_2}$ at 110 km altitude. An arrow of 10° in longitude (x-axis) corresponds to unit length.

Having a coordinate system based on the IGRF magnetic field model enables us to better compare the magnetic perturbations measured by SuperMAG, in the two hemispheres.

As a result of the non-orthogonality of this system, the calculation of field components is somewhat more complex. The calculation is not carried out here, but results from *Richmond* [1995] for the horizontal components of the magnetic perturbation, are used. They are then given by:

$$\Delta B_{q\phi} = \frac{\boldsymbol{f_1} \cdot \Delta B}{F} \tag{4.12}$$

$$\Delta B_{q\lambda} = \frac{\boldsymbol{f_2} \cdot \Delta B}{F} \tag{4.13}$$

where ΔB is the measured magnetic perturbation in geographic coordinates and F is a scaling factor which arises due to the non-orthogonality .

4.2.5 Altitude Adjusted Corrected Geomagnetic coordinates

The last coordinate system we will use in this thesis is the Altitude Adjusted Corrected Geomagnetic Coordinates (AACGM). It is closely related to the apex-based coordinate systems but differs slightly in the tracing of the field lines. Instead of following the field line to the apex, the highest point above Earth, one traces the field line to where it crosses the geomagnetic dipole equatorial plane. From this point one again follows a virtual purely dipolar magnetic field line towards the surface of the Earth, before calculating the geomagnetic latitude and longitude [*Weimer*, 2005, *Appendix A*].
Figure 4.9, adopted from *Laundal* [2010], shows Apex, red, and AACGM, black, coordinates mapped onto a geographic grid. Here we see that the two systems are indeed very similar. In fact the difference between the two is less than the uncertainty introduced when mapping the images from the WIC and Polar Earth camera [*Laundal*, 2010]. Consequently we assume them to be equally good in this thesis. Also, this figure nicely displays the non-uniform nature of the Earth's magnetic field. Conjugate cells (boxed by latitudinal and longitudinal lines) in the two hemispheres are differently sized depending on the magnetic field strength in the two areas. This

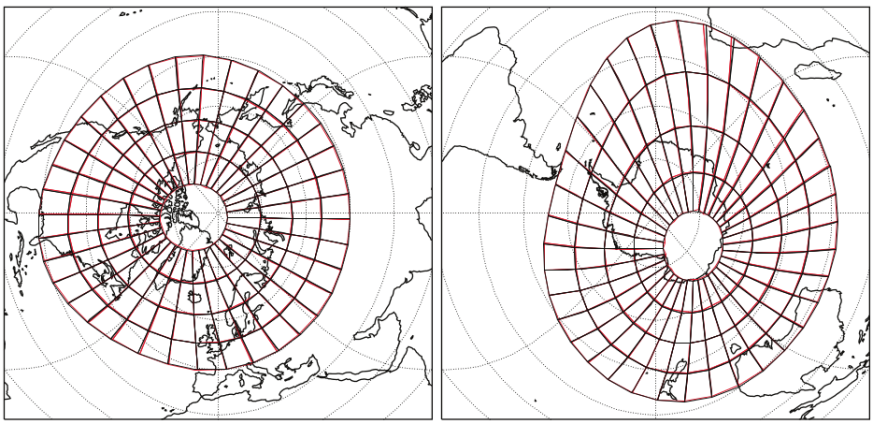

Figure 4.9: Apex and AACGM coordinate systems are mapped onto a geographic grid. Apex coordinates are shown in red and AACGM coordinates in black. Figure adopted from *Laundal* [2010].

is most apparent towards the South Atlantic Anomaly as one would expect since we use the IGRF field model (see Figure 4.6) for the calculation of the coordinates.

The small deviation between the apex-based Quasi Dipole coordinate system and the AACGM system allows us to use IDL routines for AACGM coordinates in our calculations. Routines are written by R.J. Barnes at the Johns Hopkins University, Applied Physics Laboratory for calculations between coordinate systems [*Barnes*, 2013]. In this thesis we use this software to calculate AACGM coordinates and MLT values. The calculations for AACGM coordinates and MLT calculations in this thesis are done using this software.

4.2.6 Coordinate transformation procedure

In Chapter 4.2.2 we described the NEZ-coordinates used by SuperMAG to present their data. The images from the satellites are presented in modified apex coordinates. To be able to compare and combine these measurements we made two assumptions:

1. We assumed that the N-coordinate of the SuperMAG system is along the IGRF field model. By doing this we can use the IDL routines for converting between magnetic coordinates and geographic coordinates provided by the GEOPACK library.

2. We assumed that the deviation between the apex-based Quasi Dipole coordinates at ground level ($h = 0$), modified Apex coordinates at the height of auroral emissions ($h_A = 130$km), and AACGM coordinates is so small that we can consider them as equal for our purposes. This is a reasonable assumption for auroral latitudes, as explained by *Weimer* [2005] *Apendix A*.

The procedure for calculating and transforming the magnetic perturbation vectors from the SuperMAG data and plotting them on the aurora images from the two satellites consists of the following steps:

At the geographic position P of a magnetometer, we calculate the angel α between the horizontal vectors of the IGRF model magnetic field at that time, and the Geographic north direction, using the GEOPACK library routine for IDL [*Tsyganenko*, 2014]. We then use these to compose base vectors, $\hat{\boldsymbol{x}}_{geo} = [\cos\alpha, -\sin\alpha]$ and $\hat{\boldsymbol{y}}_{geo} = [\sin\alpha, \cos\alpha]$, to transform the measured SuperMAG vectors, $B_N = B_x^{sm}$ and $B_E = B_y^{sm}$, from the NEZ-coordinate system to geographic coordinates as follows.

$$B_x^{geo} = \hat{\boldsymbol{x}}_{\boldsymbol{geo}} \cdot \boldsymbol{B^{sm}} = \cos\alpha \cdot B_x^{sm} - \sin\alpha \cdot B_y^{sm} \tag{4.14}$$

$$B_y^{geo} = \hat{\boldsymbol{y}}_{\boldsymbol{geo}} \cdot \boldsymbol{B^{sm}} = \sin\alpha \cdot B_x^{sm} + \cos\alpha \cdot B_y^{sm} \tag{4.15}$$

The next step is the transformation to Quasi Dipole/AACGM coordinates. This is done by multiplication with base vectors for this coordinate system, $\boldsymbol{f_1}$ and $\boldsymbol{f_2}$. These base vectors are dependent on the gradients of λ_q and ϕ_q (see Equations 4.9 and 4.10). We find them by projecting one small, strictly north-south vector and one small, strictly east-west vector in geographic coordinates to AACGM coordinates. This is done using the conversion routine provided in the AACGM IDL library by *Barnes* [2013]. The vector projections are then used to find the gradients of λ_q and ϕ_q, which we calculate using the standard definition of a gradient in spherical coordinates. The accuracy of this is discussed at the end of Chapter 4.2.4.

Having found the gradients, we use Equations 4.9, 4.10 and 4.11 to find base vectors for the AACGM coordinate system. Having found $\boldsymbol{f_1}$ and $\boldsymbol{f_2}$ we can use Equation 4.13, 4.12 and applying the scaling factor F suggested by *Richmond* [1995], to calculate the measured magnetic disturbance in AACGM coordinates. The magnetic disturbance in the north direction, B_x^{AACGM}, and in the east direction, B_y^{AACGM}, are given by the following:

$$B_x^{AACGM} = \frac{\boldsymbol{f_1} \cdot B_x^{geo}}{F} \tag{4.16}$$

$$B_y^{AACGM} = \frac{\boldsymbol{f_2} \cdot B_y^{geo}}{F} \tag{4.17}$$

Finally, we find the direction of the equivalent current from the magnetic disturbances by rotating the total horizontal field vector $\boldsymbol{B^{AACGM}} = [B_x^{AACGM}, B_y^{AACGM}]$, clockwise by 90°.

An example of the result of this procedure is shown in Figure 4.10, where the total horizontal field vector as measured by SuperMAG (pink) rotated clockwise by 90°, is shown, as well as the calculated and likewise rotated $\boldsymbol{B^{AACGM}}$ (blue). Strictly speaking it is not entirely correct to plot $\boldsymbol{B^{sm}}$ on this image, as it is in AACGM coordinates. But doing so illustrates how the transformation effects the vectors. Also, this example illustrates the non-orthogonality of the coordinate system as the individual vectors are affected differently depending on their position.

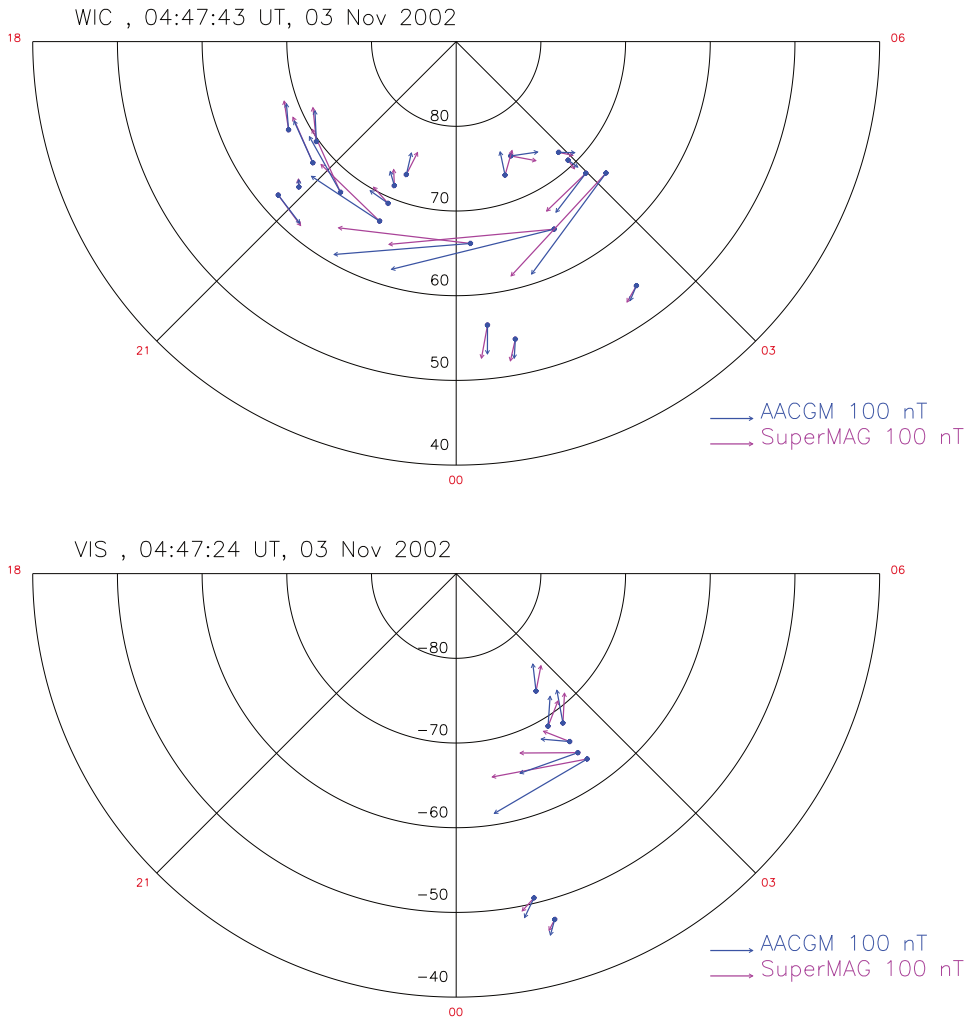

Figure 4.10: Example of the effect of transforming horizontal components of the measured disturbances of the magnetic field.

Figure 4.10 also illustrates how the data in this thesis will be presented. If not otherwise stated the images will show counts with the associated colorbar on the left, vectors indicating the direction of the equivalent current but keeping the magnitude of the measured magnetic disturbance in nT, and date and time in UT of the image and measurement at the bottom. The dot at the beginning of each of the vectors indicate the position of the ground magnetometer in AACGM coordinates. The MLT is shown at the edge of the outer semicircle in steps of three hours.

4.3 Determination and identification of non-conjugacy and ΔMLT

Three of the non-conjugate aurora events presented in this thesis were identified by *Reistad et al.* [2013] from a 19 hour conjugate image pair dataset. The last event included in this thesis, from May 12th 2001, is identified and presented by *Laundal*

and Østgaard [2009].

The determination of non-conjugate auroral features is challenging due to the difference in camera sensitivity (see Chapter 3.3.3) and a direct comparison of the intensities from the cameras is not straight forward. To compensate for this, *Reistad et al.* [2013] developed a fairly robust method to scale the intensity of the two cameras so that non-conjugate aurora could be identified. This was done by comparing the intensity distributions of an intensity profile along a reference MLT-slice that is located well outside the suspected asymmetric auroral features in the conjugate images and has count rates well above noise level. A conjugate image pair are images within 60 seconds of one another. The intensities from the VIS Earth camera are then scaled compared to the WIC images, from the intensity relation found by these profiles. This is reflected in the color scale of the conjugate image pairs, given in corrected counts. Subsequently the non-conjugate features are tested by an MLT-slice test to determine if they indeed are non-conjugate. The slice-test is a plot of the pixel counts of a slice along the MLT where we see unequal auroral features, versus the latitude along the slice. By comparing the intensity distribution of these plots, *Reistad et al.* [2013] identified the non-conjugate auroral features. To be classified as a non-conjugate feature, the intensity in one hemisphere must be twice the intensity in the conjugate region in the other hemisphere when the mentioned scaling is used. Figure 4.11 shows an example of a typical conjugate image pair, where the intensity of the VIS image is scaled so that its color should reflect an approximate equal brightness in the WIC image. The color bar, in corrected counts for each image, is shown on the left. The center of exposure time is obtained is indicated at the top of each image, while the time of the SuperMAG measurements is indicated in red in the lower left corner. In the rest of this Thesis we refer to the time of the SuperMAG measurements when referring to conjugate images pairs, as this will be equal for VIS and WIC images.

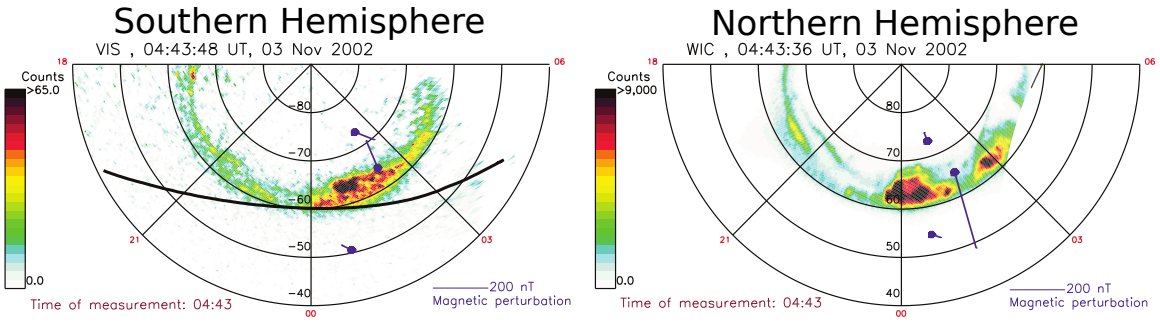

Figure 4.11: Example of a conjugate image pair. Images are obtained at 04:43 UT on November 3rd 2002 as indicated above the images. A color bar of the corrected counts is shown left of the images. The solid black line indicated the terminator, where $SZA = 90°$. Magnetic perturbation measurements at SuperMAG stations are indicated by purple dots and lines. The time at which SuperMAG measurements are obtained is indicated in red in the bottom left corner, and a reference length vector in purple in the lower right corner.

The B_y and B_x components of the IMF can introduce latitudinal and longitudinal

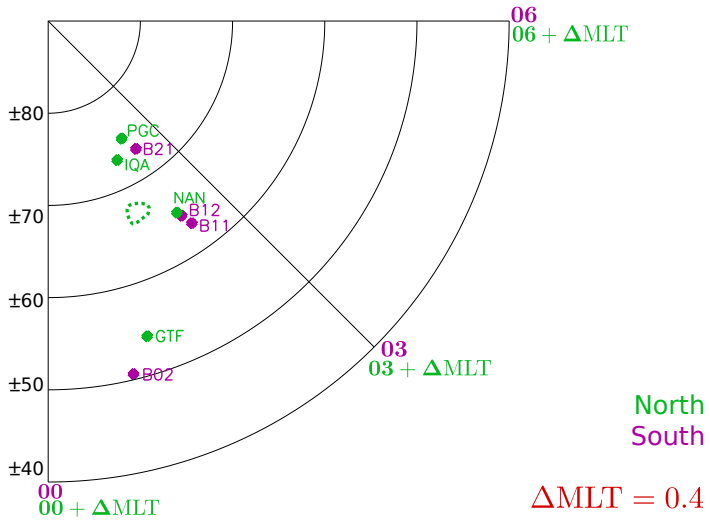

Figure 4.12: Example of a map in AACGM coordinates where the northern hemisphere is shifted such that conjugate regions are in the same position. Stations and MLT+ΔMLT coordinates in the Northern Hemisphere are shown in green while stations and MLT coordinates in the Southern Hemisphere are shown in pink.

displacement of conjugate points in the different hemispheres with respect to the IGRF model [*Cowley et al.*, 1991]. For the identification of true conjugate regions being on the same field line, *Reistad et al.* [2013] perform a correlation test of the conjugate image pairs after the intensity relation is found. The images are mapped on a rectangular grid and shifted in 0.1 MLT steps for ±2 hours. For each step a correlation coefficient is calculated. The MLT shift giving the largest correlation is then defined to be the displacement of conjugate regions expressed as ΔMLT. The images from the northern hemisphere are shifted dawnward for positive ΔMLT and duskward for negative ΔMLT.

In the present thesis we use ΔMLT in a similar manner, as calculated *Reistad et al.* [2013], to shift the northern hemisphere. In Chapter 5 we present a map for each event, in AACGM coordinates at the time of the observed asymmetry, where the SuperMAG stations used, in northern and southern hemisphere are projected on top of each other. The stations are indicated in different colors for each hemisphere. Here we have shifted the northern hemisphere by ΔMLT so that conjugate regions are at the same position on the map. The indicated stations are shifted as well. Inspection of these maps lets us determine which stations are approximately in conjugate regions. We will refer to these stations as *conjugate stations* in this thesis. Figure 4.12 shows an example of this. Stations in the Northern Hemisphere are shown in pink while stations from the Southern Hemisphere are shown in green. Also, a dotted circle or shape is drawn on every map, intended to give the reader an idea of the approximate position of the asymmetry of the particular event. The coloring is based on which hemisphere the asymmetry is observed in. The concentric circles indicate the magnetic latitude for both hemispheres (positive for the northern hemisphere and negative for the southern hemisphere). At the end of every radial line the MLT and shifted MLT for the respective hemisphere are indicated.

4.4 Analyses

In order to study the currents associated with the observed non-conjugate aurora, we investigate the ground magnetic perturbations to the Earth's magnetic field. The aurora is created by particles precipitating along the geomagnetic field. It typically occurs in regions dominated by electron precipitation and hence an upward field aligned current is associated with auroral activity (see Chapter 2.3). In the following we will describe how we search for signatures of the upward field aligned currents expected to be associated with the intense non-conjugate aurora observed.

4.4.1 Duration of non-conjugate aurora intervals

We first need to determine the duration of the observed non-conjugate aurora. This will be a crucial step as we look for magnetic perturbation signatures that occur simultaneous and thus can be associated to the observed non-conjugacy. It is done by visual inspection of the conjugate images prior and after the time at which *Reistad et al.* [2013] identified clear non-conjugate auroral features. We plot a time series of conjugate image pairs centered at this time, using the same intensity scaling on all image pairs. We then look for the non-conjugate feature of the initial image pair identified by *Reistad et al.* [2013], in the image pairs obtained before and after. Doing this we identify the first image pair in which the non-conjugate feature is clearly visible and the last. The time at which these two image pairs are obtained are now defined as the interval of the non-conjugate auroral feature. When presenting our results in Chapter 5 we include a figure of the 5-6 conjugate image pairs centered around the time of the initial image pair where the non-conjugacy is most clearly seen, and including the identified start and end time of the non-conjugate auroral feature. In the presented magnetometer data, we indicate these two times by vertical solid red lines in each plot.

4.4.2 Magnetic perturbation analyses

Biot-Savarts law (Equation 2.10) gives the magnetic field $\mathbf{B}(\mathbf{r})$, at a point $\mathbf{r}$, in terms of an integral over the volume current density $\mathbf{J}$. Using this relation, the expected magnetic perturbations to a field aligned current at mid-latitudes are in the eastward or westward direction, depending on the direction of the field aligned current and the hemisphere in which it is observed (see Figure 4.13)[*Sun et al.*, 1984]. In this thesis we make use of this mid-latitude signature of a field aligned current, as has been done by numerous studies investigating the Magnetosphere-ionosphere coupling [*Akasofu and Meng*, 1969; *Clauer and McPherron*, 1974; *Fukushima and Kamide*, 1973a; *Haaland et al.*, 1999; *Iyemori*, 1990; *Kamide et al.*, 1996; *Nakano*, 2005]. In addition to this well established interpretation of the ground magnetic perturbations at mid-latitudes, we attempt to use the same approach at higher latitudes inside the auroral oval and well poleward of the asymmetric aurora that we investigate. One might expect these signatures to be less pronounced due to the bending of the geomagnetic field. Nevertheless, it has been suggested [*Gjerloev and Hoffman*, 2014] that ground magnetometers well within the polar cap experience signatures of field aligned currents. Thus, it is of interest to explore this possibility in this study.

We define three regions of interest from which we study the ground magnetometer data. The poleward region is, as the name implies, poleward of the non-conjugate aurora and outside the auroral oval. Stations within this region are referred to as poleward stations regardless of the hemisphere. Likewise, the equatorward region is defined as the region towards the equator of the non-conjugate aurora, well outside the auroral oval at mid-latitudes above 30° magnetic latitude to avoid effects from the field aligned currents in the other hemisphere [*Fukushima and Kamide*, 1973a; *Nakano*, 2005].Stations are referred to as equatorwards stations in this thesis. The last region of interest is the region within the auroral oval and in the vicinity of the non-conjugate aurora. This is a very general definition of regions and the distance to the stations within these can vary greatly. We will consider the position of all stations in relation to the observed auroral features, separately for all events presented.

When investigating the ground magnetic perturbation measurements (see Chapter 5), special attention is given to the direction of the perturbations. The same arguments as for the mid-latitude ground magnetometer stations are used in the poleward region to determine the expected direction of the generated magnetic perturbation field from field aligned currents. The direction of the field, from Biot-Savart law (Equation 2.10), is given as a right-handed system. For a simplified situation of a single upward field aligned current in the northern hemisphere, we therefore expect a magnetic perturbation field on the ground, in an anti-clockwise direction around the current as we look from space. In the poleward region this implies an eastward perturbation, while we expect a westward magnetic perturbation field in the equatorwards region. The sketch in Figure 4.13 is intended to give a simple picture of the expected directions of the magnetic perturbation fields for a simplified field aligned current in both hemispheres.

The left panel of Figure 4.13 shows a field aligned current, J_{FAC}, directed away from the Earth in the northern and southern hemisphere as indicated by the blue arrows. The generated torodial magnetic perturbation field, B_p, is indicated by the black arrow and the direction by the two circles. Small, red houses represent poleward and equatorward ground magnetometer stations. From the simple sketch in the left panel of Figure 4.13 we discern the expected ground magnetic perturbations direction at each station. At the poleward station in the northern hemisphere and the equatorward station in the southern hemisphere we expect the direction of B_p from an upward field aligned current to be westward. At the equatorward station in the northern hemisphere and the poleward station in the southern hemisphere we expect B_p from an upward field aligned current to be eastward [*Nakano*, 2005]. It is clear from the left panel of Figure 4.13 that a given field aligned current generates equal but opposite horizontal magnetic perturbation fields in the two hemispheres.

The right panel of Figure 4.13 shows a similar sketch to that of the left panel. The blue circles indicate the horizontal westward electrojet, J_{WEJ}, in both hemispheres with the respective generated perturbation magnetic field ,B_p, shown in black. Figure 4.13 (right) illustrates the response of a horizontal current in the ionosphere at the ground magnetometer stations in the different regions in both hemispheres. The poleward and equatorward stations experience a vertical magnetic field perturba-

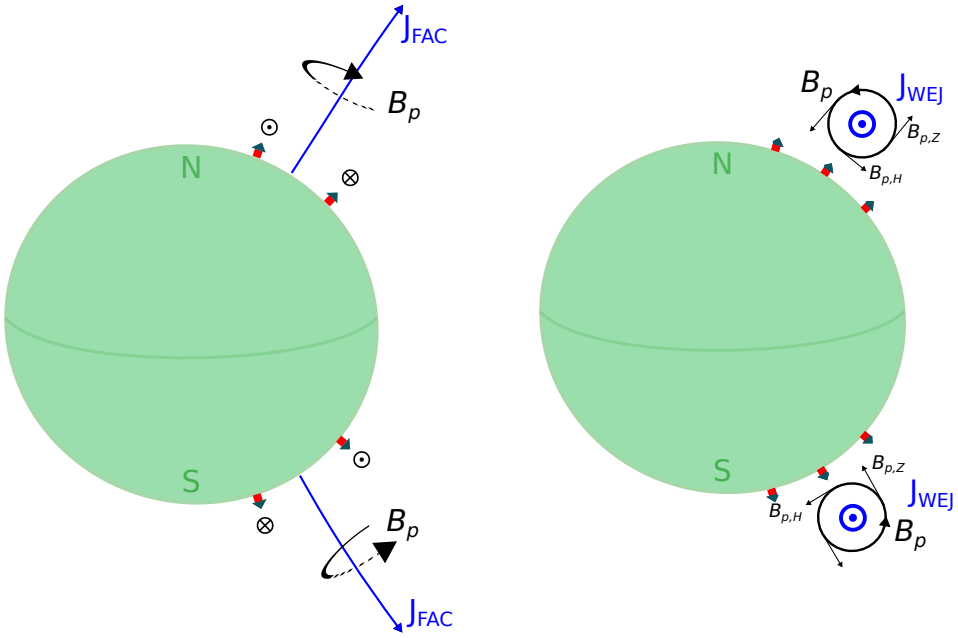

Figure 4.13: Expected ground magnetic perturbation direction of a simple upward field aligned current at poleward and equatorward stations in both hemispheres (left panel). Expected vertical and horizontal ground magnetic perturbation field at poleward-, oval-, and equatorward stations in both hemispheres (right panel).

tion, B_{pZ}, where the direction is dependent on the location of the current relative to the ground magnetometer station. A perturbation towards the Earth's center is defined to be in the positive Z direction, while a radially outwards perturbation is negative. The magnitude of B_{pZ} is dependent on the distance to the horizontal generating current, indicated as J_{WEJ}, as the field falls of by $\frac{1}{r}$ according to Equation 2.10. At conjugate stations in the two hemispheres the vertical component is equal but oppositely directed for a given horizontal current.

As described in Chapter 2.2.5, field aligned currents produce no ground magnetic perturbation directly underneath the ionosphere. Thus, for a ground magnetometer station directly below the auroral oval the observed ground magnetic perturbations are mainly a result of the ionospheric Hall current/electrojets [*Fukushima*, 1994]. The right panel of Figure 4.13 illustrates this and shows the expected direction of the ground magnetic perturbation field in the auroral oval region, below the westward electrojet. In both hemispheres we expect a strong southward perturbation at the stations in this region.

5 Observations

In this chapter a total number of 4 non-conjugate auroral events are presented. Images of both hemispheres obtained by the Polar VIS and IMAGE WIC cameras in combination with ground magnetic perturbation measurements from ground magnetometer stations, part of the SuperMAG network, are the basis of this study. In the following analyses we pay special attention to the observed magnetic perturbations magnitude and direction simultaneous to the observed non-conjugate auroral features.

5.1 Non-conjugate auroral events and corresponding SuperMAG measurements

The non-conjugate auroral events presented in the following section are not in chronological order as there are only four. Instead we present events ordered from the event with the best data coverage, first, to the event with less than optimal data coverage, last. Each event is presented in a separate section, with the satellite images and ground magnetometer data first, followed by our interpretation of the data. Eight figures are shown for each event, with the exception of the first event, where we show nine. A large figure of the conjugate image pair where the non-conjugate auroral feature is most clearly seen is presented first, followed by a plot of the IMF and geomagnetic activity during the event. Five or six conjugate image pairs for the interval of the non-conjugate event are presented in panels in the next figure. A map of the conjugate station pairs and the measurements from these stations are presented next, followed by three plots of the ground magnetometer perturbation in the three regions of interest. The last figure presented for every event, is an illustration of our interpretation of the data in terms of currents and magnetic perturbation. For the first event, we also show a plot of the *Sym-H* index in the second section.

5.1.1 Event of May 12th 2001

5.1.1.1 Observations

The first event we analyze occurred on May 12th 2001 and has been the subject of previous studies [*Laundal and Østgaard*, 2009; *Laundal et al.*, 2010]. It occurred during a large substorm in the evening sector. This is the most geomagnetically active event presented in this thesis. In Figure 5.1 we present images, in a AACGM coordinates, from Image WIC (upper) and Polar VIS Earth (lower) at 21:45 UT on May 12th 2001 when the observed asymmetry is most clearly visible in the morning sector. Each image has a colorbar to its left displaying the colorscale of the intensity in corrected counts. The concentric circles indicate the latitude (AACGM) from $\pm 40^\circ$ to $\pm 80^\circ$ with negative values for the southern hemisphere. Radial lines are drawn for every 3 hours of MLT with midnight at the bottom. The black line across the images show the position of the terminator at 90° SZA. This reveals the seasonal difference of the two hemispheres. A substorm occurred in both hemispheres with onset at 21:20 UT around 22-23 MLT [*Laundal and Østgaard*, 2009]. In the southern hemisphere the aurora is most dominant in the dusk sector and located further towards the pole than in the northern hemisphere. However, we will focus on a transient spot in the northern hemisphere dawn sector appearing twice, at 21:39 UT lasting until 21:53 UT, and at 22:11 UT lasting til 22:18 UT. In Figure 5.1 the blue ring indicates the recurrent non-conjugate feature, while the dashed blue ring shows the conjugate area in the southern hemisphere. *Laundal and Østgaard* [2009]; *Laundal et al.* [2010] suggested the conductivity difference effect to be the cause of this non-conjugate feature (see Chapter 2.3.1). Purple dots and lines indicate the position and magnetic perturbation vector at the time of the image. The direction and length of the vectors indicate the measured direction and magnitude of the total horizontal magnetic perturbation field in AACGM coordinates. The exact time of the measurements and the length of the unit vector for the SuperMAG measurements are shown at the bottom of each image. It is apparent from Figure 5.1 that the equatorward stations are far from the substorm onset location and the main auroral activity in the dusk sector.

The general geomagnetic and IMF conditions of the event that occurred on May 12th 2001 are shown in Figure 5.2. The dashed vertical blue line shows the time of substorm onset. Two solid vertical red lines, indicate the time of the first and last image where we clearly see the non-conjugate auroral feature. Two dashed vertical red lines indicate the second appearance of the non-conjugate auroral feature. In the time span from 21:00 UT to 23:00 UT the IMF was dominated by a positive B_x around 9nT, indicated in orange. The B_y component of the IMF, shown in green, was stable around 0nT until 21:50 UT where it increased slightly up to a maximum value of 5nT around 22:30 UT. B_z, shown in pink, fluctuated between -3nT and -6nT during this time interval. The AE index indicated by the black line and the right y-axis, experienced a maximum value 1100nT at 21:40 UT and then decreased to a minimum value of 620nT at 22:15 UT.

Figure 5.3 shows six conjugate image pairs in the time span from 21:35 UT to 21:53 UT covering the first appearance of the non-conjugate auroral feature in the morning sector of the northern hemisphere. Images of the southern hemisphere are shown

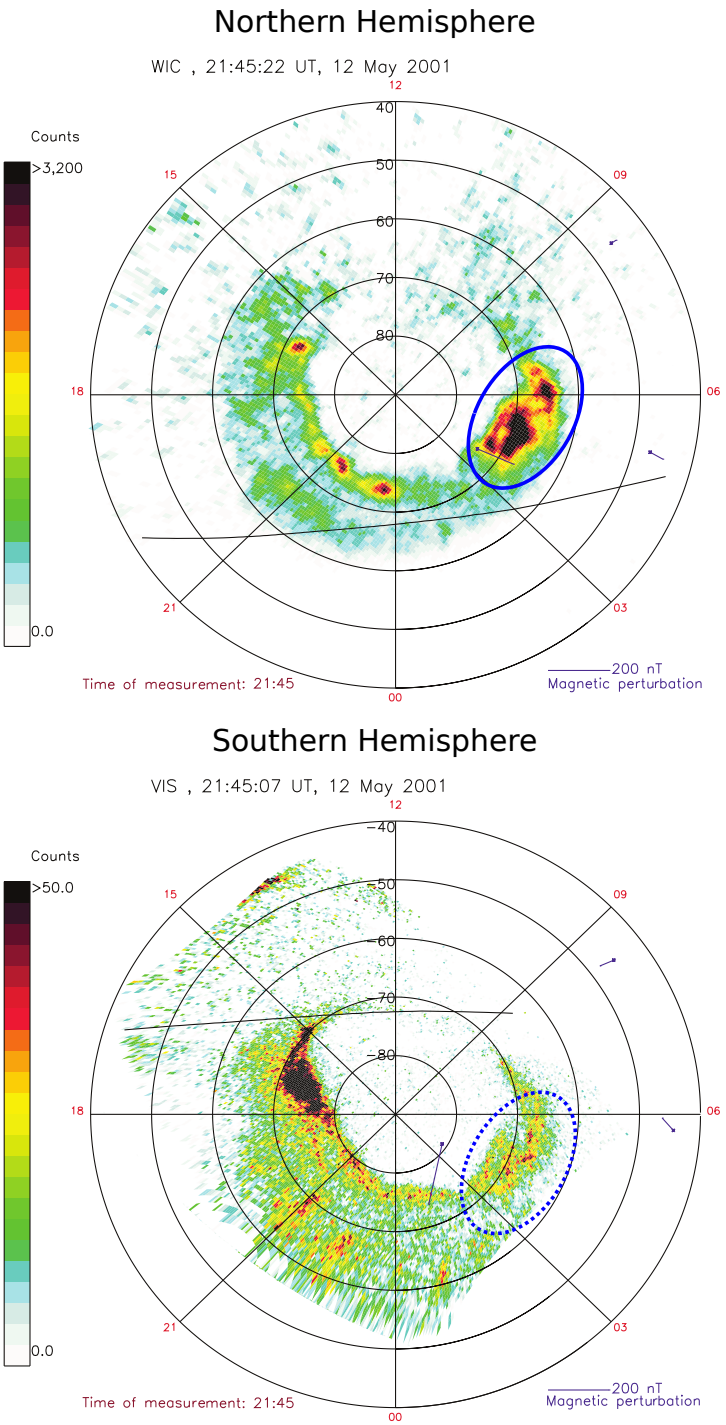

Figure 5.1: Conjugate image pair from IMAGE WIC (upper) and Polar VIS Earth (lower) obtained at 21:45 UT on May 12th 2001. The blue circle indicates the non-conjugate auroral feature in the northern hemisphere, the dashed circle the conjugate area in the southern hemisphere. Purple lines show the SuperMAG magnetic perturbation field vector at the time of the image. The exact time of the exposure of the images is shown at the top of each image while the exact time of the magnetic measurement is shown in the lower left corner of the figure. A unit vector is shown in the lower right corner of each image.

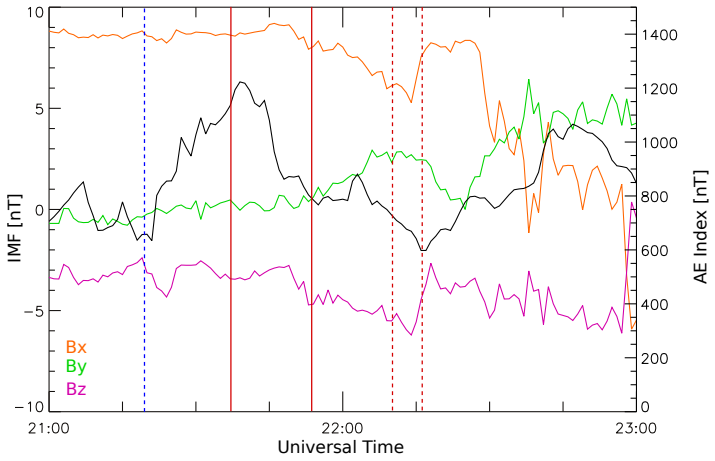

Figure 5.2: IMF and geomagnetic conditions on May 12th 2001. The dashed blue line indicates the time of substorm onset, solid red lines indicate the first appearance and disappearance of the non-conjugate auroral feature, while the dashed red lines indicate the second appearance of the non-conjugate feature. The x, y and z components of the IMF are shown in orange, green and pink, respectively. The black line shows the AE index with the scale indicated on the right axis.

in the left column, while images of the northern hemisphere are shown in the right column. In the rest of this thesis we refer to the time of the obtained SuperMAG magnetometer measurements, indicated in red in the left corner of every image, when referring to the individual conjugate image pairs. The non-conjugate feature observed in the morning sector on May 12th 2001 is first clearly observed in the WIC images at 21:39 UT and lasts until 21:53 UT. The first panel of Figure 5.3 is obtained at 21:35 UT 15 minutes after substorm onset. The non-conjugate feature is not yet evident. However, the large spatial extent of the substorm in the evening sector is clear. The second panel shows the conjugate image pair obtained at 21:39 UT, and is the first where the non-conjugate feature in the morning sector is visible. Also, the difference in the location of the polar cap boundary found by *Laundal and Østgaard* [2009] is apparent in the evening sector. The second, third and fourth panel show the spatial evolution towards the pole, of the non-conjugate auroral feature in the morning sector of the northern hemisphere. *Laundal and Østgaard* [2009] report a poleward leap as large as 10° latitude by 21:53 UT. In the fourth panel the non-conjugate auroral feature has expanded northward of the poleward station VIZ. A small an weak auroral feature directly equatorward of CSY, the poleward station in the southern hemisphere becomes visible in the fifth panel. This will be discussed in more detail in Section 5.1.1.2. The bottom panel shows the last conjugate image pair where the non-conjugate feature in the morning sector of the northern hemisphere is visible during its first appearance. From this image series we identify the interval of the first appearance of the non-conjugate auroral feature to be from 21:39 UT to 21:53 UT, while the second appearance is observed from 22:11 UT to 22:18 UT (see Chapter 4.4.1).

Figure 5.4 shows a map in AACGM coordinates, identical to those used in the satellite images. The northern hemisphere is rotated by $\Delta MLT = -0.2$, and projected onto the map of the southern hemisphere, such that the used SuperMAG

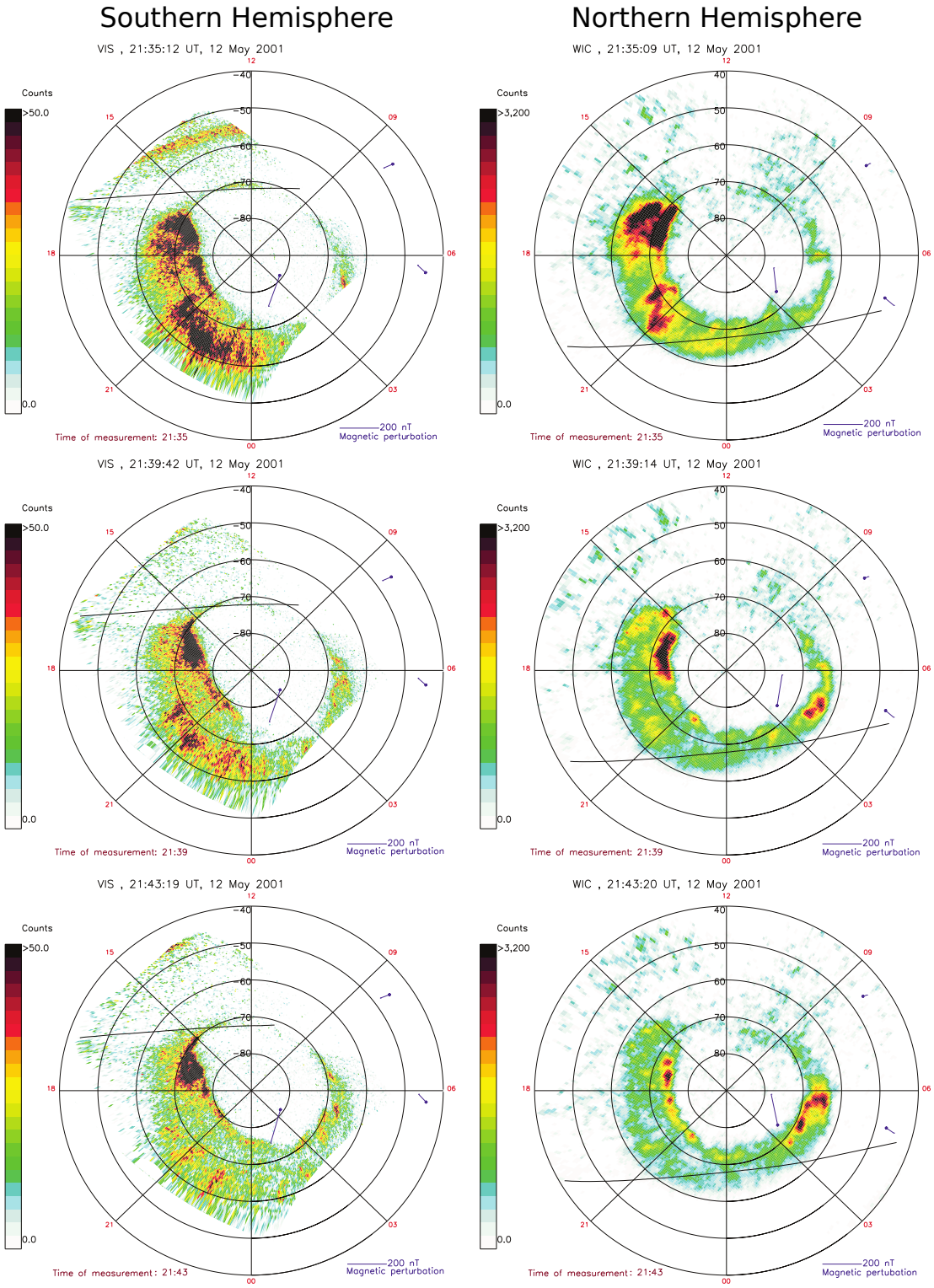
Southern Hemisphere
Northern Hemisphere
VIS , 21:35:12 UT, 12 May 2001
WIC , 21:35:09 UT, 12 May 2001
VIS , 21:39:42 UT, 12 May 2001
WIC , 21:39:14 UT, 12 May 2001
VIS , 21:43:19 UT, 12 May 2001
WIC , 21:43:20 UT, 12 May 2001
Counts
>50.0
>3,200
0.0
Time of measurement: 21:35
Time of measurement: 21:39
Time of measurement: 21:43
200 nT
Magnetic perturbation

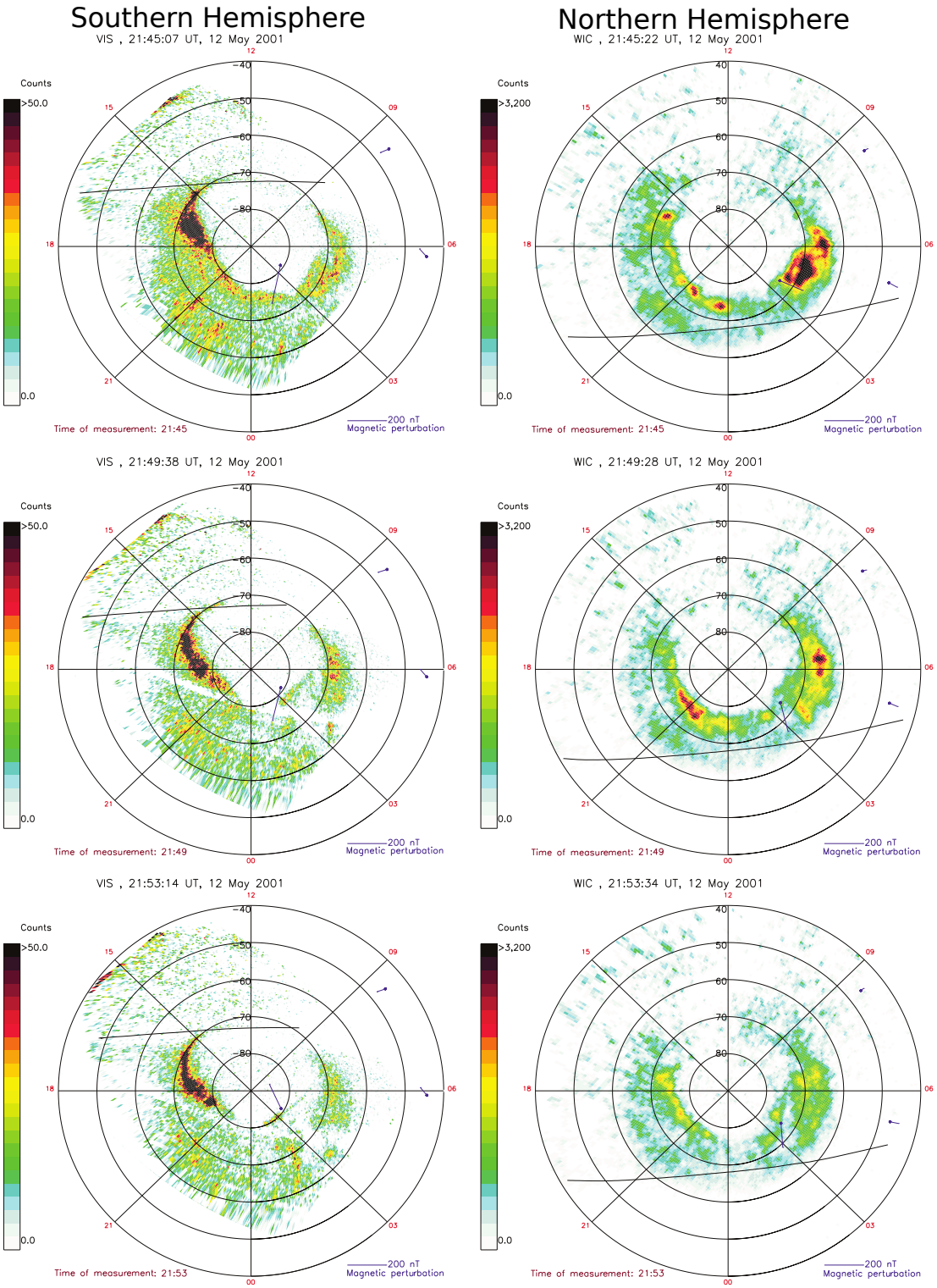

Figure 5.3: Conjugate image pairs from Polar VIS Earth (left) and IMAGE WIC (right) obtained at 21:32 UT, 21:39 UT and 21:43 UT on May 12th 2001. Purple lines show the SuperMAG magnetic perturbation field vector at the time of the image.

magnetometer stations line up to the expected footpoint of the conjugate field lines. The ΔMLT calculated by *Reistad* [2012] and used here is ΔMLT = −0.2. Pink dots indicate the position of the SuperMAG magnetometer stations in the southern hemisphere, while green dots mark stations in the northern hemisphere. The MLT is given for both hemispheres, green for north and pink for south. The dashed green shape is a sketch of the observed non-conjugate aurora in the northern hemisphere to give an impression of the approximate position in relation to the conjugate SuperMAG ground magnetometer stations. From Figure 5.4 it is apparent that no conjugate station pairs are in the auroral oval region for this event. However, there are two pairs of conjugate stations in the equatorward region of the asymmetric feature. The first pair, IRT and GNA, is in the dawn sector and the second pair, PTK and CNB, is in the early morning sector. The conjugate stations pairs for this event are defined as:

Poleward region : VIZ and CSY

Equatorward region 1 : IRT and GNA

Equatorward region 2 : PTK and CNB

In the following presentation of the ground magnetic perturbation measurements for each of the three regions, we will pay special attention to any signature starting around 21:20 UT, at substorm onset and any signature corresponding to the appearances and duration of the non-conjugate auroral feature. However, we note that substorm onset is around 22-23 MLT and far from our equatorward station pairs. Thus, we expect any signature of substorm onset, if any is observed, to be weak.

Polewards stations CSY and VIZ

Figure 5.5 shows the measured magnetic perturbation field at the poleward stations, VIZ and CSY, in the northern and southern hemisphere. The top panel shows the northward component of each station, again green indicates the northern hemisphere while pink shows measurements from the southern hemisphere. Measurements are shown with nano Tesla (nT) on the y-axis and universal time (UT) on the x-axis. The middle and bottom panel of Figure 5.5 are similar but show the eastward and vertical component, respectively. The scale of the y-axis varies depending on the measured values and varies greatly for the three panels of this event. The time of substorm onset, at 22-23 MLT, is indicated by the dashed blue line, the solid red lines indicate the first appearance and disappearance of the non-conjugate auroral feature in the morning sector of the northern hemisphere, while the dashed red lines indicate the second. At CSY, the poleward station in the southern hemisphere, the northward component is steady around 100nT until 21:51 UT where a sudden decrease to a minimum value of −100nT is apparent. VIZ station, the conjugate station in the northern hemisphere, has a steady northward component around 100nT before a rapid southward turning to −200nT, starting at 21:43 UT. An increase to almost 0nT is observed at 21:46 UT before a gradual decrease to -250nT at 21:54 UT and a subsequent more rapid decrease to -600nT at 22:18 UT. The eastward component at both stations (middle panel) shows a clear response to the substorm

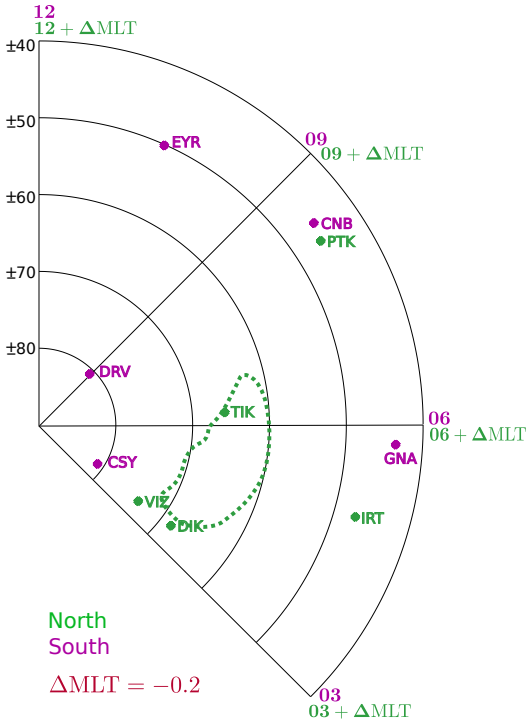

Figure 5.4: Map of the Southern Hemisphere in magnetic AACGM coordinates at 21:45 UT on May 12th 2001, indicating relevant SuperMAG stations used for this event. Stations in the northern hemisphere, shown in green, are projected onto the map and rotated by $\Delta\text{MLT} = -0.2$ [*Reistad et al.*, 2013]. The stations in the southern hemisphere are shown in pink. Each concentric circle indicates the magnetic latitude for the northern hemisphere (positive values) and the southern hemisphere (negative values). MLT values are shown for both hemispheres, green for north and pink for south. Conjugate station pairs for this event are GNA and IRT, CSY and VIZ, and CNB and PTK. The green dotted line shows an approximate outline of the non-conjugate aurora observed in the northern hemisphere to give an impression of its position in relation to the stations used.

onset occurring at 21:20 UT in the distant 22-23 MLT region. At VIZ (north) we see a sudden increase from approximately −75nT to +150nT in the time span from onset to 21:38 UT, followed by a decrease to −100nT. The sudden westward turning at VIZ coincides with the appearance of the transient non-conjugate auroral feature. Before 21:43 UT the total direction of the magnetic perturbation field in the northern hemisphere is consistent with an upward field aligned current. At this time the non-conjugate spot has been visible in the images for 4 minutes, although not as intense as at this time. In right panel of Figure 5.3 we see an increase in the intensity and spatial extent of the non-conjugate auroral feature in the morning sector. The fourth panel of Figure 5.3 reveals that VIZ station in the northern hemisphere, is just at the edge of the non-conjugate auroral feature and eventually beneath the transient feature. In both the Polar VIS images and the ground magnetometer measurements it is clear that VIZ is in the region of the transient feature after the poleward expansion of the non-conjugate auroral feature at 21:43 UT. Consequently, after 21:43 UT the signature at VIZ is consistent with an overhead westward horizontal current. From this point VIZ is no longer comparable to the poleward station in the southern hemisphere within the method defined in Chapter 4. Compared to VIZ, the conjugate station in the southern hemisphere, CSY, is located further towards the pole (see Figure 5.4) and shows a gradual decrease of 200nT in the time span from 21:20 UT to 21:46 UT. At 22:11 UT, the time the non-conjugate feature appears for the second time, the eastward component in both hemispheres, which have had a comparable magnitude and direction for about ten minutes, show opposite evolution for about five minutes. At CSY the eastward component of the magnetic perturbation field shows a small eastward turning of about 50nT while a westward turning of the same magnitude is observed in the northern hemisphere. Consistent with the arguments presented in Chapter 4.4, no response related to the time span where we observe the non-conjugate auroral feature the first time in the northern hemisphere, is visible at CSY in the southern hemisphere. However, we see a sharp increase from −150nT to 100nT at 21:52 UT corresponding to an eastward turning at CSY.

The vertical component at VIZ, shown in green in the bottom panel of Figure 5.5, is positive shows a gradual increase starting at substorm onset. This suggests that the observed overhead horizontal westward current is centered equatorward of the station. At CSY, in the southern hemisphere, we first see an increase of about 100nT before the vertical component decreases to fluctuate around −300nT, starting around 21:40 UT, the time of the appearance of the non-conjugate auroral feature. In the time from 22:11 UT to 22:18 UT an increase and subsequent decrease from -300nT to -100nT is observed at CSY.

Equatorward stations IRT and GNA

The equatorward stations IRT and GNA in the northern and southern hemisphere are located at a magnetic latitudes of 47.4° and −44.4°, respectively. Measurements of the ground magnetic perturbation field from these stations are shown in Figure 5.6. Again, we will pay special attention to signatures starting at substorm onset at 21:20 UT, and any signature during the periods of the non-conjugate auroral feature. The northward components at IRT and GNA, shown in the upper panel,

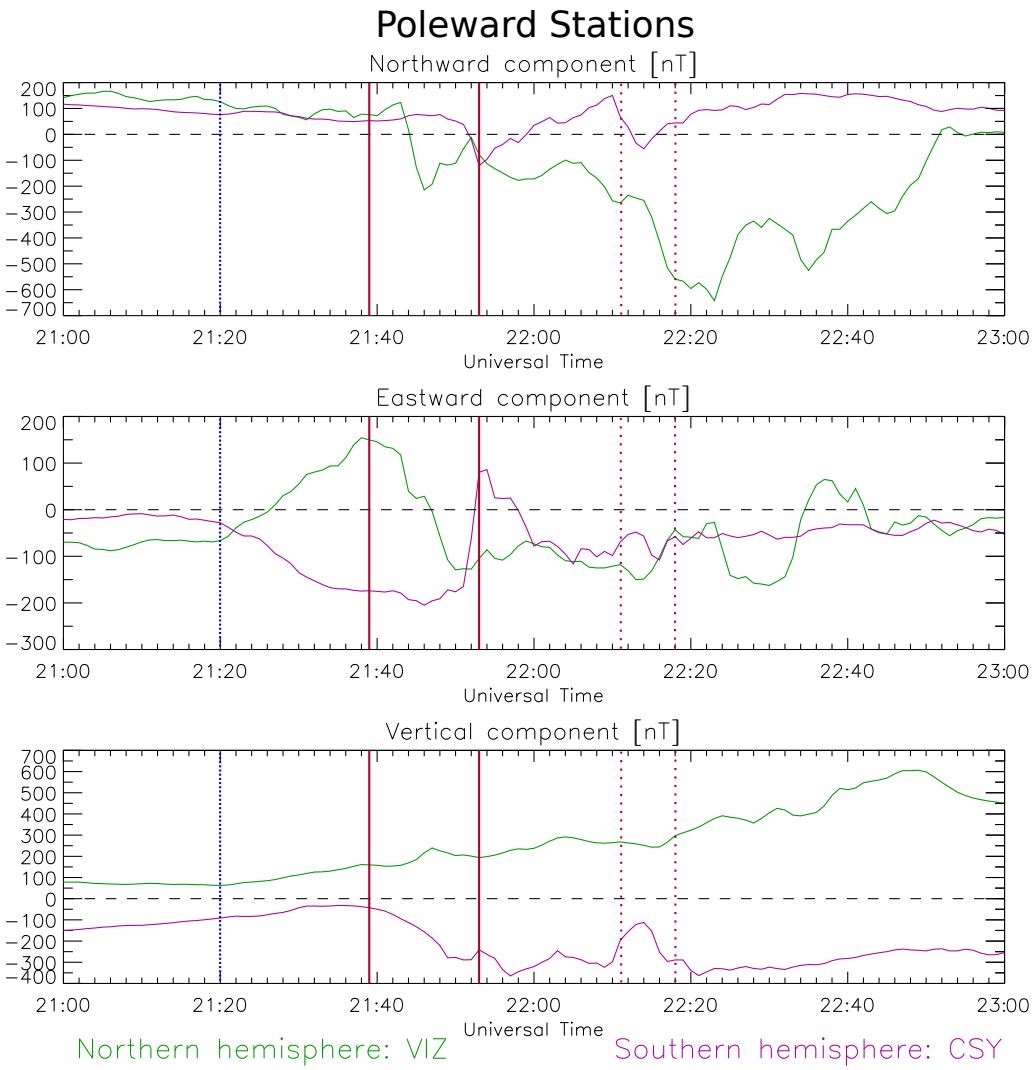

Figure 5.5: Conjugate stations CSY in the southern hemisphere (pink) and VIZ in the northern hemisphere (green) positioned poleward of the auroral oval on May 12th 2001. The dashed blue line indicates the time of substorm onset, solid red lines indicate the first appearance and disappearance of the non-conjugate auroral feature, while the dashed red lines indicate the second appearance of the non-conjugate feature. After 21:43 UT, VIZ station in the northern hemisphere, is beneath the transient non-conjugate auroral feature.

are very similar. Both show a gradual decrease of about 25nT starting at substorm onset followed by an increase to a maximum of 0nT at 22:20 UT. The eastward component at both stations, shown in the middle panel, shows a sudden change starting at substorm onset at 21:20 UT. At IRT, in the northern hemisphere, a decrease from 10nT to a minimum of −25nT takes place, while at GNA, in the southern hemisphere, we see an increase from 10nT to a maximum of 40nT. For the duration of the non-conjugate auroral feature in the northern hemisphere, indicated by the two solid and dashed red line pairs in each plot, we do not see any clear signatures in any of the components at GNA, in the southern hemisphere. At IRT in the northern hemisphere, an increase of the eastward component from negative 25nT to 0nT starting at 21:36 UT is observed. This indicates a small change of direction for the total direction of the magnetic perturbation field from being somewhat westward to being mostly southward. The expected direction at this position in the northern hemisphere is eastward, considering the arguments from Chapter 4.4.

The vertical component at IRT, displayed in the bottom panel of Figure 5.6 shows a very stable evolution around 0nT. In the southern hemisphere we observe an increase from 10nT to 25nT in the measurements from the southern hemisphere at the time of substorm onset.

Equatorward stations PTK and CNB

Figure 5.7 shows ground magnetic perturbation field measurements at the two conjugate stations in the morning sector of the equatorward region of the second conjugate station pair. We expect the same signatures in this area, as for the two stations in the early morning sector. However, PTK and CNB are relatively far from the main auroral activity and therefore only very small variations are detected in the ground magnetic perturbation field measurements of these two stations. A signature of substorm onset is observed, in the northward component at both stations, in the form of a gradual decrease of 25nT starting at 21:20 UT. The measured magnitude of the northward component at the stations are separated by an offset of 20nT, with the largest absolute value seen in the southern hemisphere. The eastward component at PTK is steady around 0nT for the duration of the substorm and the first appearance of the non-conjugate auroral feature. In the southern hemisphere we detect only minor fluctuations of the eastward component around 15nT until 22:11 UT. At 22:11 UT the eastward component of both stations experiences an equal but opposite change. In the southern hemisphere this is observed as a eastward turning of about 25nT while we see a westward turning of the same magnitude in the northern hemisphere. In the southern hemisphere the total direction of the magnetic perturbation field is consistent with that of a downward field aligned current for the duration of the substorm and both appearances of the non-conjugate feature. In the northern hemisphere we only see a weak signature of a downward field aligned current for the duration of the last appearance of the non-conjugate feature.

The vertical component at PTK, in the northern hemisphere, is steady around 5nT for the duration of the non-conjugate auroral feature. However, no signatures directly related to the duration of the non-conjugate auroral feature are detectable. In the southern hemisphere the vertical component is steady around -13nT indicating a steady horizontal current in this hemisphere.

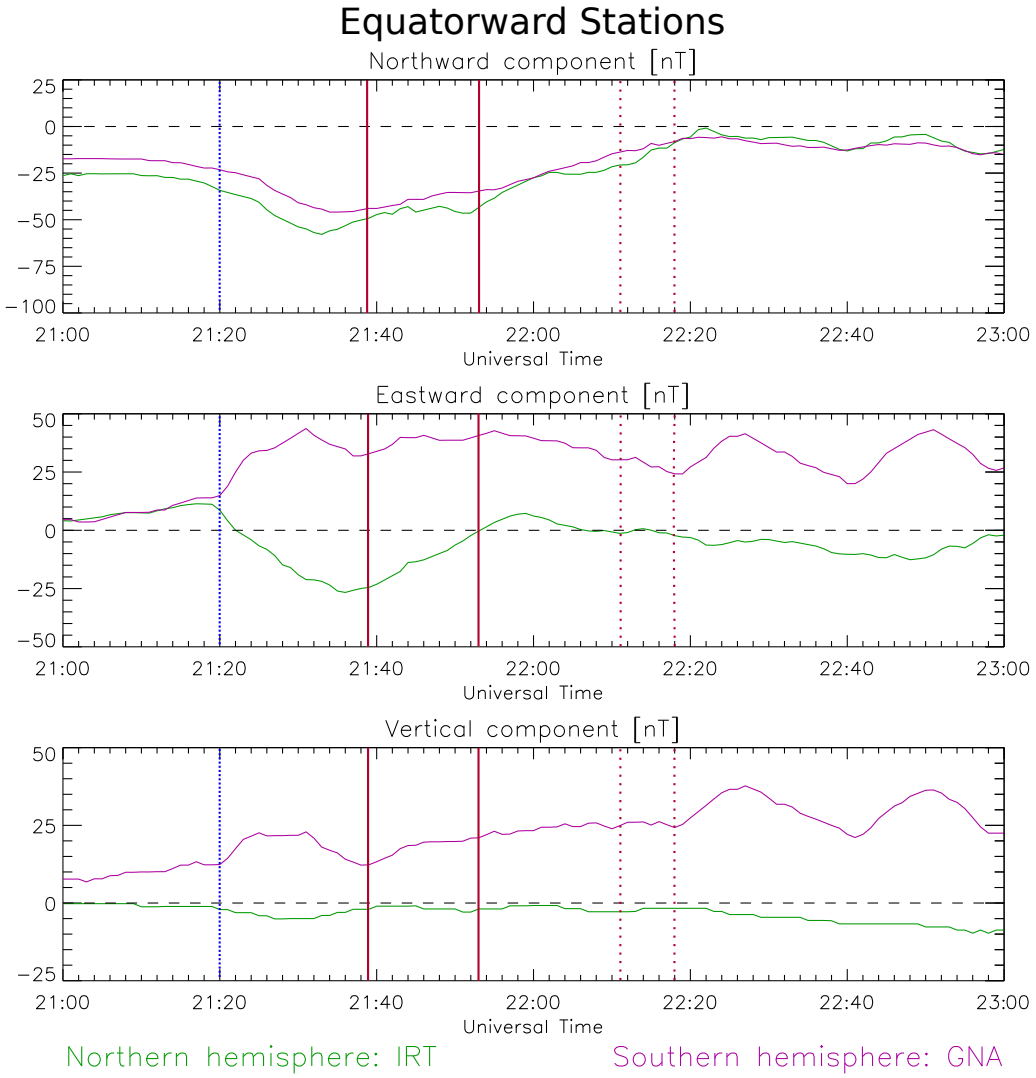

Figure 5.6: Conjugate stations IRT and GNA in the dawn sector, equatorward of the auroral oval on May 12th 2001. The dashed blue line indicates the time of substorm onset, solid red lines indicate the first appearance and disappearance of the non-conjugate auroral feature, while the dashed red lines indicate the second appearance of the non-conjugate feature.

5.1.1.2 Interpretation

In the following we present a possible interpretation of the ground magnetometer data and satellite images from May 12th 2001.

Figure 5.8 illustrates the simultaneous aurora in the northern and southern hemisphere, and the ground magnetic perturbation field measured at the SuperMAG stations. The upper panel shows our interpretation of the system of field aligned and horizontal currents related to the observed aurora and ground magnetic perturbations, at 21:35 UT being after substorm onset and before the non-conjugate feature first appears. On the left side of the circle representing the Earth we indicate the magnetic latitude in both hemispheres. The longitudinal green lines, numbered 21, 00, 03, 06 and 09 indicate the MLT. Midnight MLT is shown as a red line to highlight that the reference point is shifted dawnward from the center for a better field of view of the morning sector. A simplified sketch of the aurora observed by the two imagers onboard Polar and IMAGE satellites (see Figure 5.3), are shown in light blue. As the aurora is mostly produced by downward going electrons, we associate an upward field aligned current to these regions. We indicate these field aligned currents by blue arrows out of the plane. Proposed downward field aligned currents are indicated by brown arrows. Black arrows are drawn to indicate the approximate size and the direction of the horizontal currents in the ionosphere. The dashed black line in the southern hemisphere is shown to indicate the edge of the satellite image FOV. Magnetometer stations are drawn as red dots with an arrow pointing in the direction of the measured total horizontal ground magnetic perturbation field. One should keep in mind that Figure 5.8 sketches a three-dimensional system on a two-dimensional plane. Also, the shift in MLT of the conjugate points in the two hemispheres is not included in the sketch. The bottom panel is similar to the top panel but shows a sketch of the aurora and ground magnetic perturbation measured at 21:45 UT when the recurring non-conjugate auroral feature in the morning sector of the northern hemisphere is clearly visible. A sketch of the non-conjugate feature and the associated ground magnetic perturbation measurement are drawn in yellow. As the coverage of auroral oval by the VIS Earth Camera is decreasing towards the end of the substorm, our main focus is on the first appearance of the non-conjugate auroral feature.

After substorm onset and before the appearance of the non-conjugate auroral feature in the morning sector of the northern hemisphere, the ground magnetic perturbation measurements are not distinctly consistent with a single field aligned current regardless of polarity. This leads us to interpret the measurements as a superposition of several field aligned currents. We suggest the two-current-wedge (DCW) system proposed by *Gjerloev and Hoffman* [2014] as a possible current configuration at this time. *Gjerloev and Hoffman* [2014] present a DCW system model derived from ground magnetic measurements of 116 substorms in the northern hemisphere. The key features are a poleward shift of the westward electrojet in the premidnight sector, a polar cap vortex bounded by the westward electrojet towards the equator and a significant difference in magnitude of the two current wedges. For the May 12th 2001 event, we observe two of the three key features specified by *Gjerloev and*

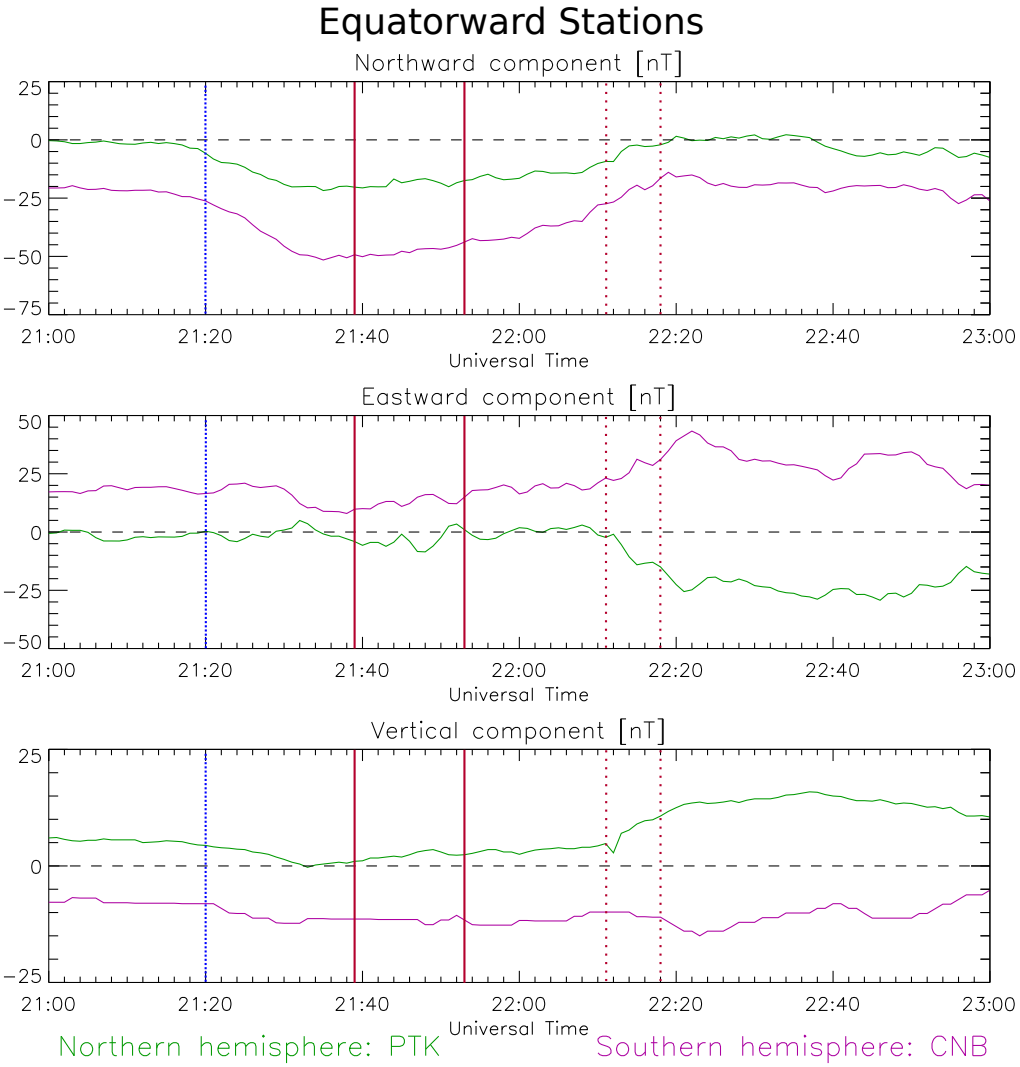

Figure 5.7: Conjugate stations PTK and CNB in the morning sector, equatorward of the auroral oval on May 12th 2001. The dashed blue line indicates the time of substorm onset, solid red lines indicate the first appearance and disappearance of the non-conjugate auroral feature, while the dashed red lines indicate the second appearance of the non-conjugate feature.

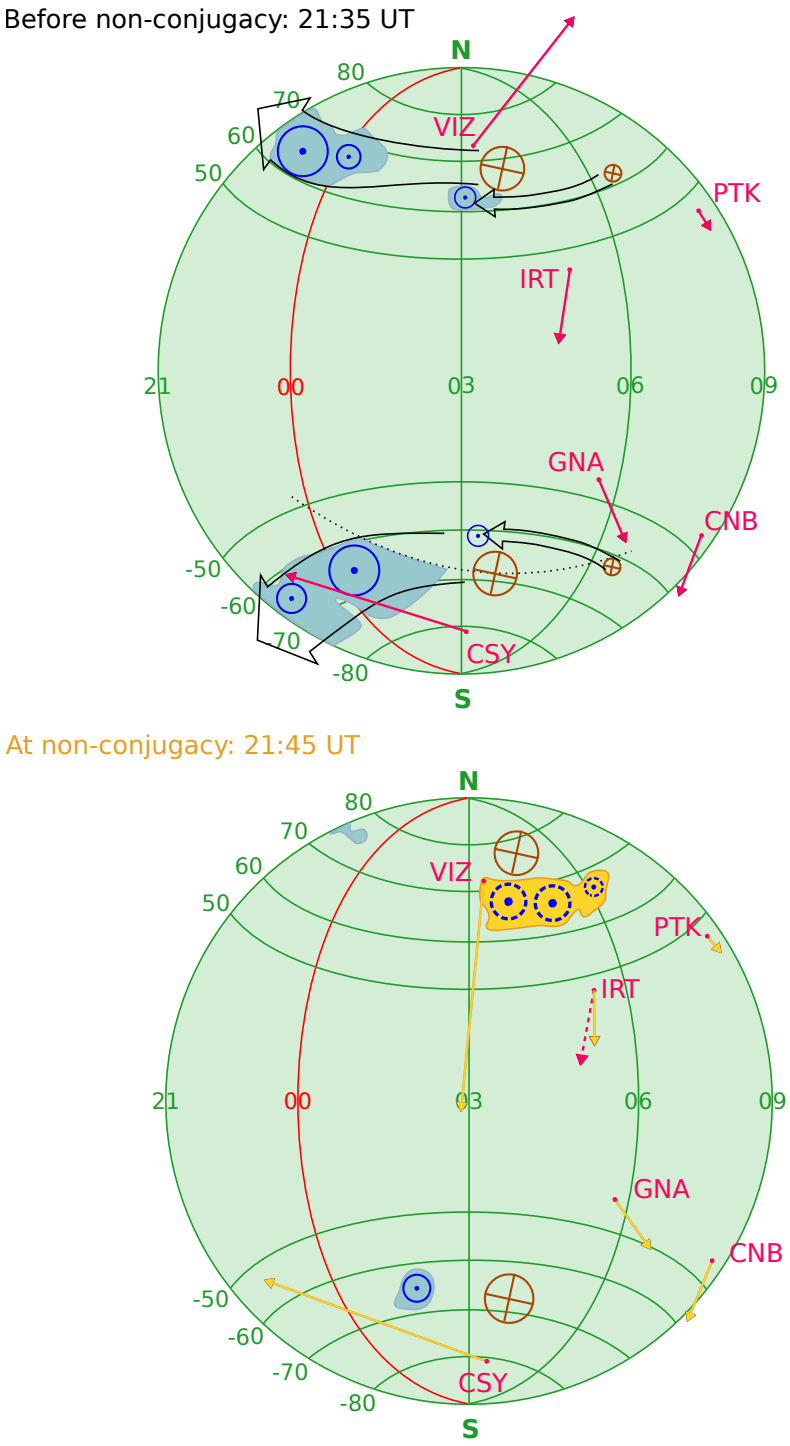

Figure 5.8: Sketch of the observed aurora, proposed current and double current wedge system for the event of May 12th 2001 at 21:35 UT (upper panel). Ground magnetometer stations and the associated measurements are shown in red. The large black arrows show the horizontal currents. The dashed black line indicates the edge of the satellite FOV in the southern hemisphere. Field aligned currents are indicated in blue and brown depending on their direction. The lower panel shows the proposed current systems at 21:45 UT. Perturbation measurements at the time of the non-conjugate auroral feature, are shown in yellow. The dashed pink line at IRT in the northern hemisphere of the lower panel is identical to the solid line at IRT in the upper panel, and show here to highlight the change from the measurement at 21:35 UT.

Hoffman [2014]. The poleward shift of the westward electrojet and the polar cap vortex are apparent when utilizing most of the available SuperMAG ground magnetometer stations in the northern hemisphere. To support this suggestion we have included a plot of this in Appendix B. Consequently, we interpret the measurements as a DCW system as sketched in the top panel of Figure 5.8. In the southern hemisphere we postulate a downward field aligned current consistent with the observed magnetic perturbation field and the arguments of Chapter 4.4 in the postmidnight sector, and upward field aligned currents and a westward electrojet in the 03-21 MLT sector in the southern hemisphere. We note that the indicated downward field aligned currents in the two hemispheres around 04 MLT are at conjugate footpoints. As we do not have as many ground magnetometer stations in the southern hemisphere, as in the northern, and VIS images have a restricted coverage compared to WIC at this time, we can not confidently propose an equal DCW system here. *Laundal et al.* [2010] point out a significant asymmetry in the polar cap boundary location in the two hemispheres starting at substorm onset. This further complicates an assumption of similarity of the current configuration in the two hemispheres. However, the few measurements in the southern hemisphere do not contradict the existence of such a DCW in the southern hemisphere. Consequently, we indicate the DCW configuration in the conjugate region in the southern hemisphere as a possible current configuration at this time.

Identifying the field aligned current system during the non-conjugate auroral feature in the morning sector of the northern hemisphere, is challenging. As mentioned earlier, we do not see a distinct signature in the ground magnetic perturbation measurements, of the non-conjugate auroral feature. In the bottom panel of Figure 5.8, a sketch of the horizontal ground magnetic perturbation and the non-conjugate auroral feature at 21:45 UT is shown in yellow. The poleward station VIZ, in the northern hemisphere is beneath the transient auroral feature and exhibits a large southward component, as is the expected signature of an overhead westward electrojet (see right panel of Figure 4.13). Consequently, we are not able to measure signatures of field aligned currents at VIZ at this time (see Chapter 2.2.5). In the fourth panel of Figure 5.3 it is apparent that CSY, the conjugate station in the southern hemisphere, is further polewards than VIZ, and poleward of the aurora at 21:45 UT. In the time span of the non-conjugate auroral feature we observe a decrease from -50nT to -270nT of the vertical component at CSY, indicating an increase in the westward electrojet, equatorward of the station. However, we do not observe any signature indicating that an upward field aligned current exists, that is comparable to the upward field aligned current we propose to be related to the non-conjugate feature in the northern hemisphere. In addition we observe a slight increase in the horizontal magnetic perturbation field at CSY, consistent with a slight increase of a downward field aligned current, indicated by the brown arrow. In the period from 21:50 UT to 22:00 UT a large response in the eastward component is observed at CSY (see Figure 5.5). However, the satellite images in the two bottom panels of Figure 5.3 reveal a small auroral feature appearing directly above CSY in that time span, and consequently we attribute the response to this feature.

The total direction of the horizontal magnetic perturbation field at the equatorward stations IRT and PTK, in the northern hemisphere, are mostly southwards and not

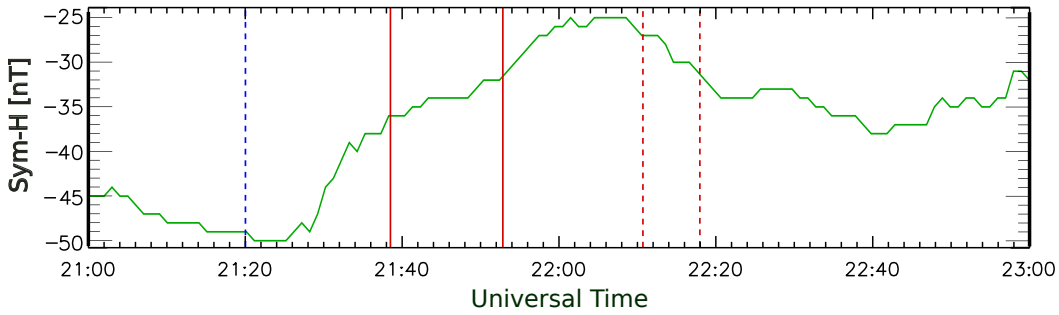

Figure 5.9: *Sym-H* index indicating the activity in the ring current on May 12th 2001. The dashed blue line indicates the time of substorm onset, solid red lines indicate the first appearance and disappearance of the non-conjugate auroral feature, while the dashed red lines indicate the second appearance of the non-conjugate feature.

consistent with the expected eastward perturbation from the postulated upward field aligned current in the area of the non-conjugate feature [e.g. *Stenbaek-Nielsen et al.*, 1972]. It is likely that the equatorward stations are significantly affected by contributions from the ring current during this event. In fact, the ring current indicies *SMR*, *SMR LT*, and *Sym-H*, indicating the activity in the ring current, are derived using ground magnetometer stations at geomagnetic latitudes up to $\pm 50^\circ$ [*Newell and Gjerloev*, 2012; *Wanliss and Showalter*, 2006]. Figure 5.9 shows the *Sym-H* index for the present event. For the duration of the non-conjugate auroral feature the *Sym-H* index had an average value of -34nT, indicating a slightly intensified ring current. The northward component at IRT and PTK in the equatorward region of the northern hemisphere show similar values. Starting at 21:35 UT we observe a small change of the total horizontal ground magnetic perturbation field in an eastward direction at IRT. We interpret this eastward turning to be consistent with an overhead upward field aligned current, related to the observed non-conjugate auroral feature in the morning sector of the northern hemisphere superposed on the ground magnetic perturbation field induced by the ring current. In Figure 5.8 this small eastward turning is illustrated in the lower panel. The dashed red arrow at IRT, identical to the solid arrow at IRT in the upper panel, indicates the direction of the ground magnetic perturbation field before the appearance of the non-conjugate auroral feature, while the yellow solid arrow shows the direction as influenced by the non-conjugate auroral feature at 21:45 UT. In total we observe one signature in the ground magnetic perturbation measurements at IRT which we attribute to the first appearance of the non-conjugate auroral feature in the morning sector.

A surprising observation at IRT and GNA is that the absolute magnitudes of the horizontal magnetic perturbation fields at these stations are comparable in the period from substorm onset to 21:36 UT. Also, subsequently, for the duration of the observed intense non-conjugate auroral feature in the northern hemisphere, the absolute magnitude of the horizontal magnetic perturbation field in the northern hemisphere is less than in the southern hemisphere. Satellite images in Figure 5.3 reveal, by the position of the terminator, that IRT is in the sunlit hemisphere while GNA is in the dark hemisphere. In addition IRT is closer to the auroral oval and the observed non-conjugate aurora than GNA, further leading us to expect a larger

ground magnetic perturbation field in the northern hemisphere. A possible factor contributing to the comparable magnitudes of the horizontal component in the two hemispheres, is that the postulated downward current in the conjugate region in the dark southern hemisphere is stronger and equals the expected difference from the non-conjugate aurora in the sunlit northern hemisphere. Such effects are reported to occur in the post midnight sector. *Ohtani et al.* [2009] found that, for a given field-aligned current density, the electron and ion precipitation is more intense and energetic in the dark (winter) hemisphere. They suggest that because the plasma density in the acceleration region is significantly lower in the dark hemisphere, the electrons need to be more accelerated along the field line to carry imposed currents. However, it is unknown if this effect can occur in the morning sector.

The comparable eastward and northward component at GNA supports our believe that the ground magnetic perturbation field observed in the equatorward regions before, during and after the non-conjugate auroral feature, is a superposition of the magnetic fields induced by the proposed field aligned currents and the ring current. The comparable value of the *Sym-H* index to the value of northward component at GNA, supports this (see Figure 5.6 and 5.9) . Also, the decrease in the northward component of the measurements from PTK and CNB, at substorm onset, is consistent with a ring current intensification at both stations. For an intensified ring current we expect an increased southward directed magnetic perturbation at ground magnetometer stations at low latitudes. The slight offset in magnitude observed in the northward component of CNB and PTK is expected as CNB is at a lower magnetic latitude than PKT ($-45.20°$ and $46.34°$ respectively). This is supported by the vertical components at PTK and CNB. The vertical components at IRT and GNA are not conclusive. It is also notable that both CNB and PTK are in the sunlit hemisphere for the duration of this event.

To summarize, we observe one signature at IRT which we attribute to the first appearance of the non-conjugate auroral feature. Further, we interpret the absence of a signature of an upward field aligned current in the southern hemisphere, comparable to the upward field aligned current we propose to be associated to the non-conjugate feature, as an indication of the existence of an asymmetric current.

5.1.2 Event of November 3rd 2002

5.1.2.1 Observations

The second event we present occurred on November 3rd 2002, during a magnetic substorm with onset at 04:40 UT. In Figure 5.10 we present conjugate satellite images from Image WIC (upper) and Polar VIS Earth (lower) at 04:47 UT when the observed asymmetry is most clearly visible. Figure 5.10 is in the same format as Figure 5.1, but here we only show the nightside oval. It should be noted that there is a large seasonal difference in the two hemispheres signified by the position of the terminator in the southern hemisphere. The terminator in the northern hemisphere is not visible in the image as it is far into the dayside. This is due to the large tilt angle of $\lambda_{tilt} = -28°$, at this time, leaving the entire southern oval sunlit, unlike the northern oval which is in darkness. In Figure 5.10 we indicate the asymmetric feature by a blue circle and a dashed blue circle at the conjugate region in the

hemisphere where we do not see the feature. In this event the non-conjugate auroral feature is a small bright spot at 01-02 MLT on the poleward edge of the oval in the northern hemisphere. Due to the asymmetry induced by the large IMF B_y component, *Reistad et al.* [2013] calculated a ΔMLT of 0.4 for this event, which we will use in the following analyses (see Chapter 4.3). Also, *Reistad et al.* [2013] reported that none of their considered mechanisms for producing interhemispheric or asymmetric currents can explain the observed asymmetry. They argue that a possible explanation for this particular event could be the ionospheric conductivity feedback mechanism proposed by *Newell et al.* [1996]. Dots and vectors at the position of the SuperMAG stations used for the event are indicated in purple.

The summarized general geomagnetic conditions during this event are shown in Figure 5.11. The dashed blue line shows the time of substorm onset while the solid vertical red lines indicate the time of the first and last image where we clearly see the non-conjugate auroral feature in the northern hemisphere. The black line and the right y-axis indicate the value of the *AE* index, which at 04:40 UT shows a sudden increase, coinciding with substorm onset identified from the satellite images. The IMF B_x, shown in orange, fluctuates between -2 and -10nT, as well as the IMF B_z, shown in pink, which fluctuates between 0nT and -9nT. The B_y component of the IMF, shown in green, is more steady during the event at a value around 8nT.

Figure 5.12 shows conjugate satellite images from VIS and WIC in the same format as in Figure 5.10. We show five conjugate image pairs from the time span from 04:39 UT to 04:49 UT, with images of the southern hemisphere in the left column and images of the northern hemisphere in the right column. The second row shows the conjugate image pair obtained at 04:41 UT, just after substorm onset. The different spatial extent of the auroral features appearing at onset, around 00 MLT are apparent in the images at this time. Images in the third row, obtained at 04:45 UT, show the first indication around 01 MLT and 66° latitude, of the non-conjugate auroral feature, in this time series of conjugate image pairs. The fourth panel shows the same images as in Figure 5.10, as this is the image pair that shows the non-conjugate feature of this event most clearly and to place it within context of the observed substorm. In the bottom panel we show the image pair obtained at 04:49 UT, which is the last pair where we see the non-conjugate auroral feature. In the image series in Figure 5.12, substorm onset, the increasing auroral intensities and the non-conjugate auroral feature, and the subsequent decrease in auroral intensities is apparent. As in Figure 5.10, the purple vectors indicate the SuperMAG observations with direction and magnitude of the total horizontal magnetic perturbation field in AACGM coordinates. From this image series we identify the interval of the non-conjugate auroral feature to be from 04:45 UT to 04:49 UT (see Chapter 4.4.1).

Figure 5.13 shows a map in the same format as Figure 5.4. The northern hemisphere is rotated by $\Delta\text{MLT} = 0.4$, and projected onto the map of the southern hemisphere, so the stations line up to the expected footpoints of the conjugate field lines. Pink dots indicate the position of the stations in the southern hemisphere, while green dots mark stations in the northern hemisphere. The MLT is given for both hemispheres, green for north and pink for south. A sketch of the observed asymmetric

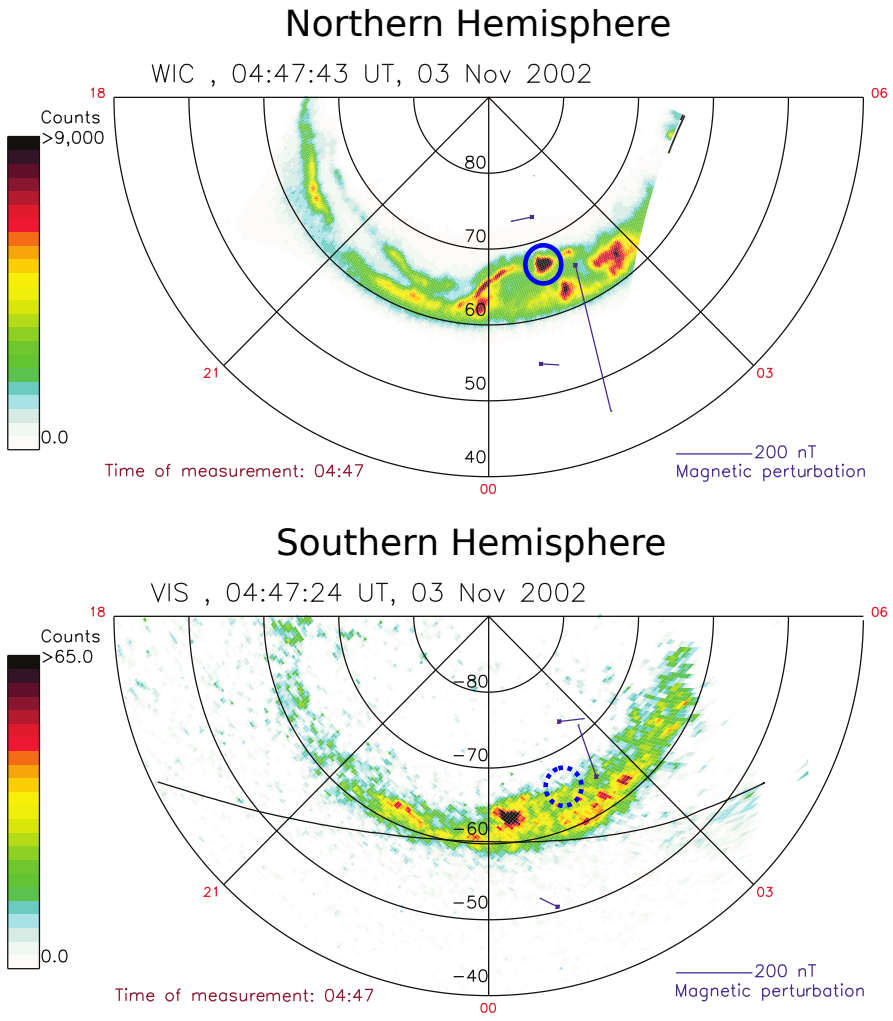

Figure 5.10: Conjugate image pair from IMAGE WIC (upper panel) and Polar VIS Earth (lower panel) obtained at 04:47 UT on November 3rd 2002. The blue circle indicates the non-conjugate auroral feature in the northern hemisphere. The purple dots show the position of the SuperMAG stations used in this event, while lines indicate the direction and magnitude of the measured magnetic perturbation field vector. The exact time of the exposure of the images is shown at the topof each image while the exact time of the magnetic measurement is shownlower left corner of the Figure. A unit vector is shown in the lower right corner.

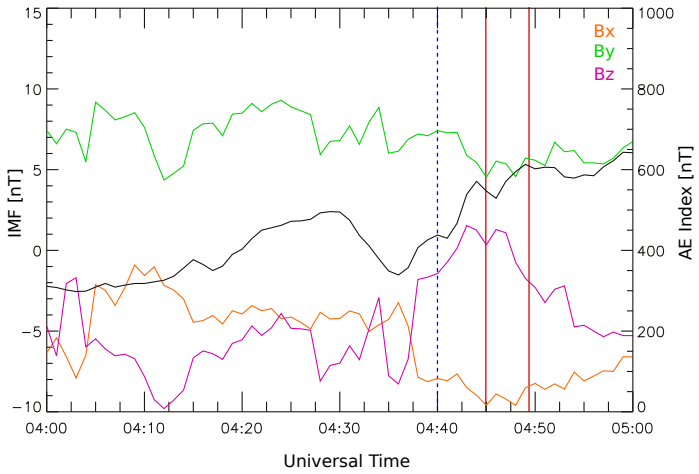

Figure 5.11: IMF and geomagnetic activity on November 3rd 2002. The x, y and z components of the IMF are shown in orange, green and pink, respectively. The black line shows the *AE* index with the scale indicated on the right axis. The vertical dashed blue line indicates the time of substorm onset while the vertical red lines indicate the time interval of the visible non-conjugate aurora.

feature is also included to give an idea of its position. The color of this dashed line signifies that the observed asymmetric feature in this event occurred in the northern hemisphere. From this map we determine three station pairs for the three different regions mentioned in Chapter 4.4. They are:

Poleward region: IQA and B21

Equatorward region: GTF and B02

Oval region: NAN and B12

Poleward stations IQA and B21

Measurements from the two poleward stations IQA and B21 are shown in Figure 5.14. Vertical red lines are drawn at the time when we first observe the asymmetry clearly in the satellite images and the time of the last image before it disappears. Dashed blue lines indicate the time of substorm onset. A westward turning, indicated by a negative value of the eastward component, starting at 04:40 UT is observed at IQA. At this point the perturbation measured at IQA is 50 nT. The measured ground magnetic perturbation in southern hemisphere station, B21, is equal in magnitude to IQA at 04:40 UT and is slowly increasing. Measurements of the eastward component in the southern hemisphere does not change significantly at any time during the duration of the spot. The northward component of both stations decreases in magnitude at a comparable rate, starting 3 minutes earlier in the northern hemisphere.

The vertical components shown in the bottom panel, indicate the activity in the horizontal currents. For this event no significant differences except for a difference in magnitude ranging from 20nT to 50nT can be detected. It is notable that the

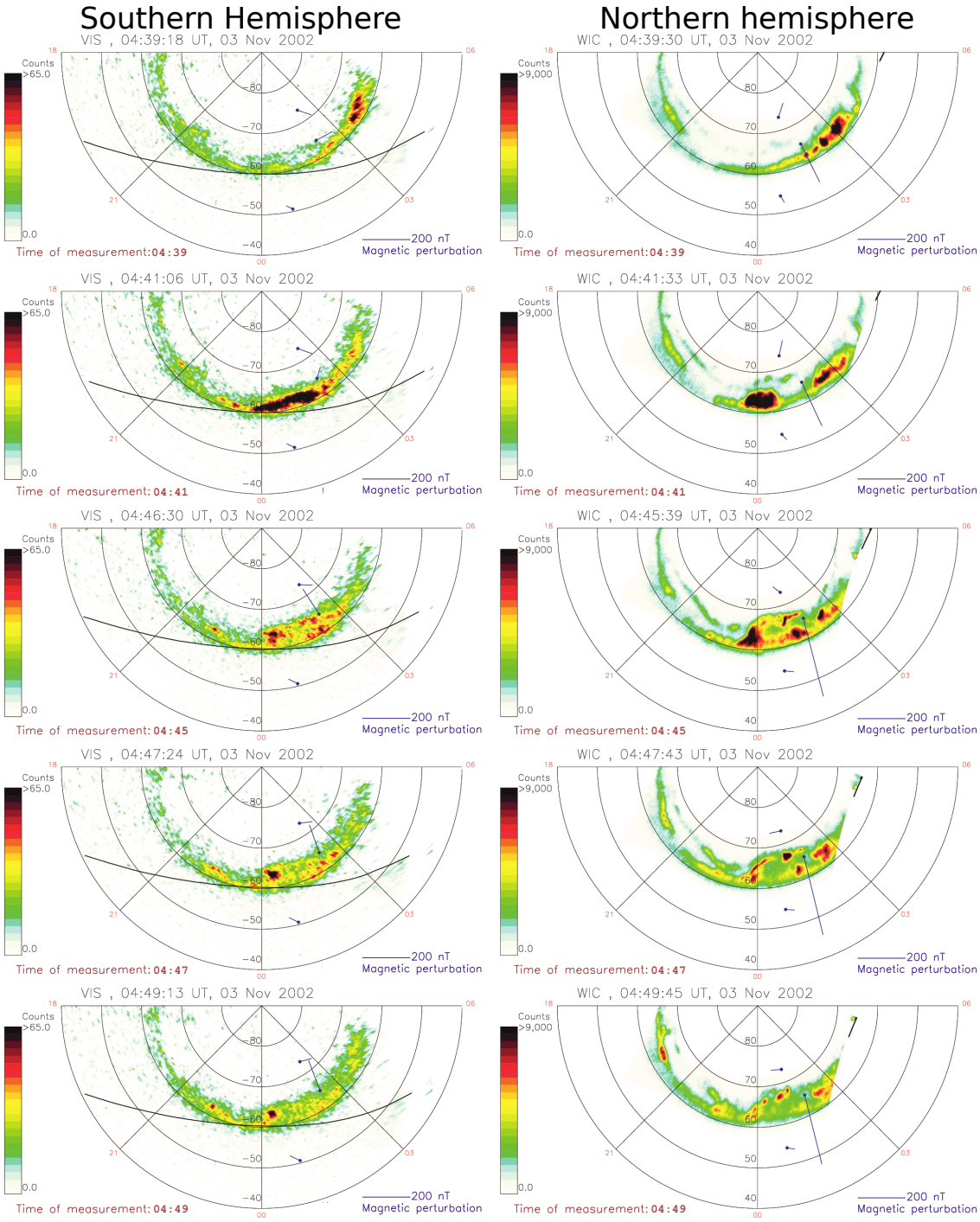

Figure 5.12: Conjugate image pairs from the southern (left) and northern (right) hemisphere from 04:39 UT to 04:49 UT on November 3rd 2002. Purple lines show the SuperMAG magnetic perturbation field vector at the time of the image.

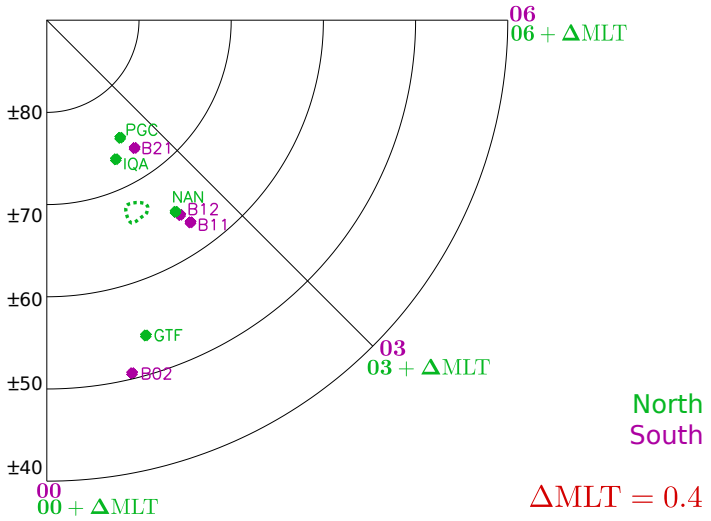

Figure 5.13: Map of the southern hemisphere in magnetic AACGM coordinates at 04:47 UT on November 3rd 2002, indicating the SuperMAG stations used for this event. Stations in the northern hemisphere, shown in green, are projected onto the map and rotated by ΔMLT = 0.4. The stations in the southern hemisphere are shown in pink. ΔMLT as calculated by *Reistad et al.* [2013] is shown in the lower right corner. Each concentric circle indicates the magnetic latitude for the northern hemisphere (positive values) and the southern hemisphere (negative values). MLT values are shown for both hemispheres, green for north and pink for south. The green dotted circle is a sketch of the approximate position of the asymmetric auroral feature in the northern hemisphere. Conjugate station pairs for this event are IQA and B21, GTF and B02 and NAN and B12.

vertical component in both hemispheres is positive, as we would expect an equal but opposite value in the two hemispheres if the measured perturbations were due to a symmetric westward electrojet (see Chapter 4.4).

Equatorward stations GTF and B02
Figure 5.15 displays measurements from the conjugate station pair, GTF and B02, in the same format as Figure 5.14 but for stations in the eqautorward region. The station in the northern hemisphere, GTF, indicated in green shows an increase of approximately 30 nT in the eastward component starting at 04:40 UT and an increase of approximately 20 nT in the northward component also starting at 04:40 UT. This corresponds to a turning in a counterclockwise direction of the total magnetic perturbation field vector. This corresponds well to the expected direction of the magnetic perturbation field generated by an upward field aligned current. Magnetic ground measurements from the station in the southern hemisphere, B02, show a slow, gradual decrease of 50nT in the eastward component, starting at 04:30 UT. The northward component of B02 shows a slight decrease of 10nT starting at 04:34 UT. These observed changes in the two horizontal components in the southern hemisphere have a different evolution in time than the observed changes in the northern hemisphere. At GTF we see a development in the eastward component, coinciding with substorm onset at 04:40 UT.

The vertical components of both stations show an increase in absolute magnitude (negative for the northern hemisphere and positive for the southern hemisphere) of approximately 10nT starting first at 04:31 UT at B02 and 9 minutes later at GTF. The increase in absolute magnitude the northern hemisphere is simultaneous to substorm onset. We note that the increase in the southern hemisphere happens at the same time as the observed change in the other two components for this station.

Stations NAN and B12 in the auroral oval
Figure 5.16 shows SuperMAG measurements from the two conjugate stations, NAN and B12, positioned in the auroral oval close to the observed asymmetric feature in the northern hemisphere. For NAN and B12, all components show a strikingly similar development. In the southern hemisphere, shown in pink, both horizontal components decrease by 150nT starting at 04:39 UT. Similar development occurs for NAN in the northern hemisphere starting 5 minutes prior, at 04:34 UT. During the time where we observe the asymmetric feature, the horizontal components at NAN reach the minimum value observed with an offset of approximately 75nT compared to B12. However, there does not seem to be a clear signature directly related to the appearance and disappearance of the asymmetric feature in the northern hemisphere. Perhaps the most notable in the horizontal measurements, is the short period where the magnetic perturbation field vector had a westward component in the southern hemisphere. However, its magnitude is small compared to the northward component, making only a small change to the direction of the total vector.

The vertical components vary with $\pm$50nT throughout the time series and are almost mirror images of each other with only a difference in sign. As described in Chapter 4.4 the vertical components corresponds to the activity in the horizontal currents so for comparable currents in the northern and southern hemisphere we expect equal

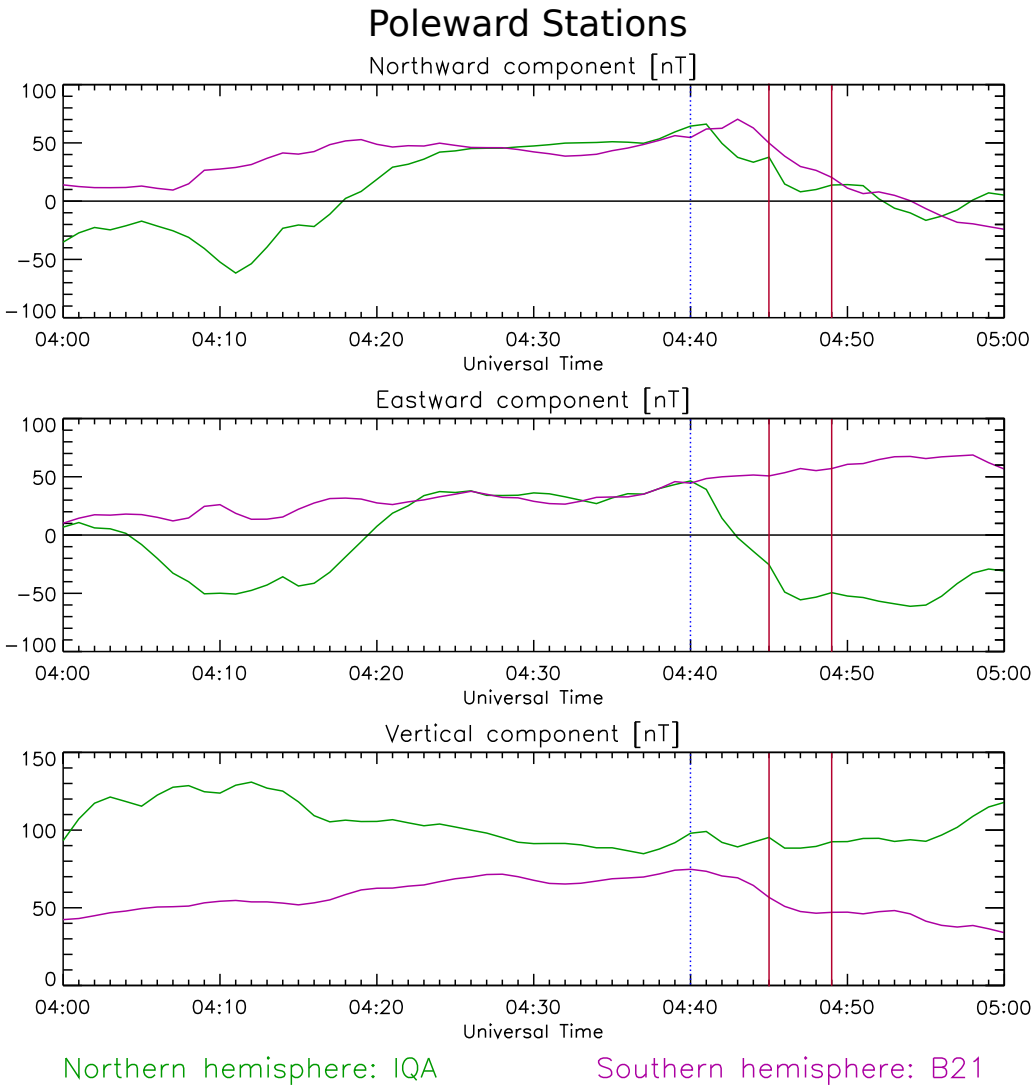

Figure 5.14: Conjugate stations IQA and B21 positioned poleward of the oval in the northern (green) and southern hemisphere (pink), respectively, for the event on November 3rd 2002. The dashed blue line indicates substorm onset while the solid red lines indicate the appearance and disappearance of the non-conjugate feature.

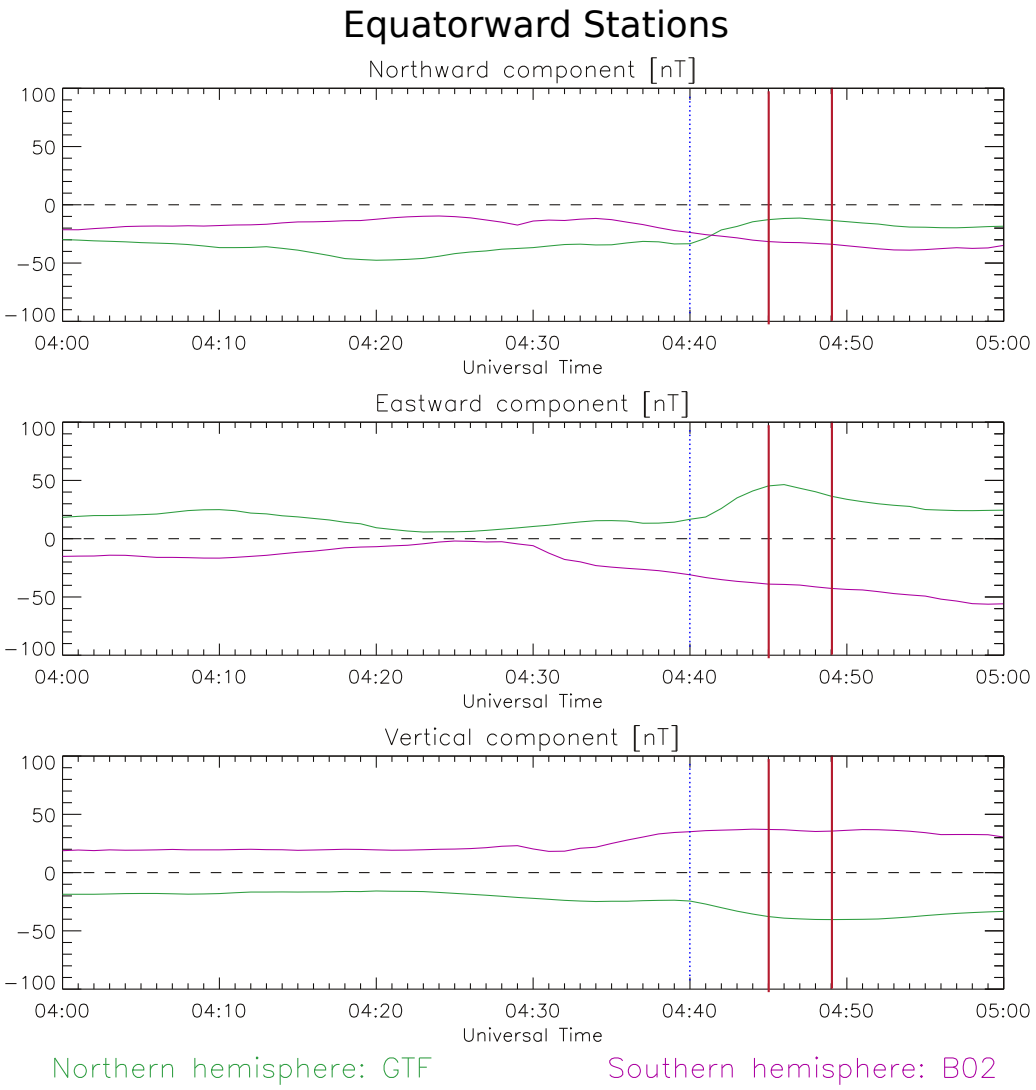

Figure 5.15: Conjugate stations GTF and B02 positioned equatorward of the oval in the northern and southern hemisphere, respectively for the event on November 3rd 2002. The dashed blue line indicates substorm onset while the solid red lines indicate the appearance and disappearance of the non-conjugate feature.

but opposite vertical measurements.

5.1.2.2 Interpretation

In the following we propose a possible interpretation of the data shown in Section 5.1.2.1, in terms of the associated large scale current systems.

Figure 5.17 illustrates the simultaneous aurora in the northern and southern hemisphere, and the ground magnetic perturbation field measured at the SuperMAG stations. The upper panel of Figure 5.17 shows our interpretation of the field aligned current system from 04:20 UT to 04:40 UT. The figure is similar to Figure 5.8, but 00 MLT is now at the center of the sketch. A simplified sketch of the aurora observed by the two cameras (see Figure 5.12), is shown in light blue. As the aurora is mostly produced by downward going electrons, we associate an upward field aligned current to these regions. In order to explain the magnetic perturbation field measurements we need to postulate downward field aligned currents in the poleward region. These are shown as brown arrows and will be explained and justified in more detail in the discussion below.

Before substorm onset (upper panel of Figure 5.17), weak aurora is observed in the auroral oval in both hemispheres. It is somewhat more stretched in the southern hemisphere than in the northern. At IQA, the ground magnetic perturbation field in the northern hemisphere appears to be affected by several different field aligned currents, as shown by the upper panel of Figure 5.17. We postulate a weak downward *R1* current in the early morning sector, indicated by brown arrows into the plane. A downward current in this area is consistent with the statistical results of *Iijima and Potemra* [1978] (see Chapter 2.2.2). Utilizing most of the available SuperMAG stations in the morning sector of the northern hemisphere, ground magnetic perturbation fields consistent with weak downward field aligned currents are observed in parts of the west-Greenland magnetometer chain east of IQA. As we have no conjugate stations to these in the southern hemisphere, we do not include the measurements from the west-Greenland stations here. Instead, we include a plot of the ground magnetic perturbation field in the morning sector of the northern hemisphere in Appendix B to support our interpretation. The measured horizontal ground magnetic perturbation field at IQA and its position as well as magnetic perturbation measurements from the additional stations in the northern hemisphere support the argument for postulating the *R1* downward current in the morning sector. As apparent from Figure 5.17 we propose comparable currents in the conjugate region of the southern hemisphere. The measured magnetic perturbation at IQA is mostly a response to the downward *R1* current with only a slight contribution from the weak upward field aligned current with a footpoint in the observed aurora. In the southern hemisphere the proposed current system is similar to that in the northern hemisphere for this time interval before substorm onset. The horizontal ground magnetic measurements at B21 are consistent with both upward and downward field aligned currents. However, unlike in the northern hemisphere, we propose that the contribution from the upward field aligned current at this station, is comparable to the contribution from the downward field aligned current. The sketch of the southern hemisphere in the top panel in Figure 5.17 illustrates this. This is reasonable since the strong IMF B_y during this event will, tend to rotate the entire

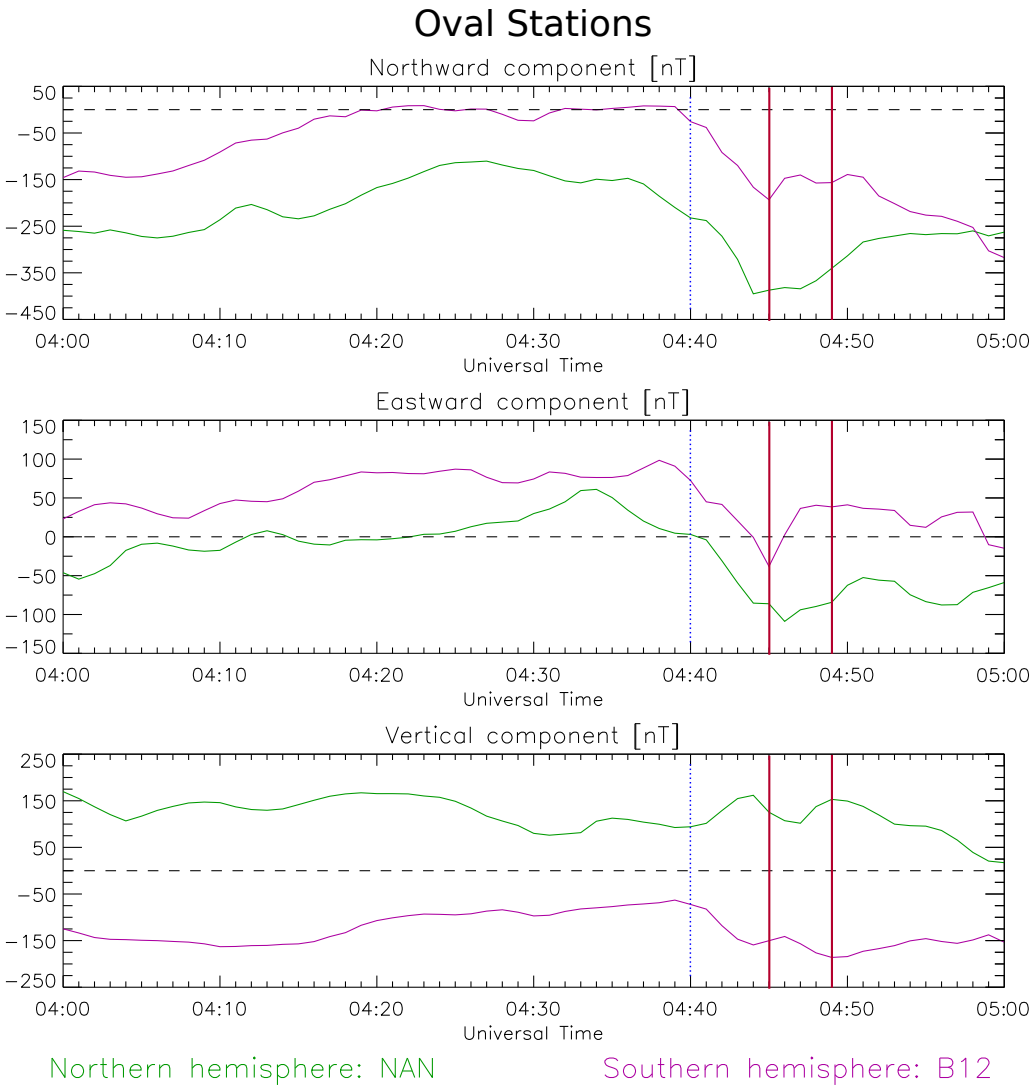

Figure 5.16: Conjugate stations NAN and B12 positioned in the auroral ovals in their respective hemispheres on the event of November 3rd 2002. The dashed blue line indicates substorm onset while the solid red lines indicate the appearance and disappearance of the non-conjugate feature.

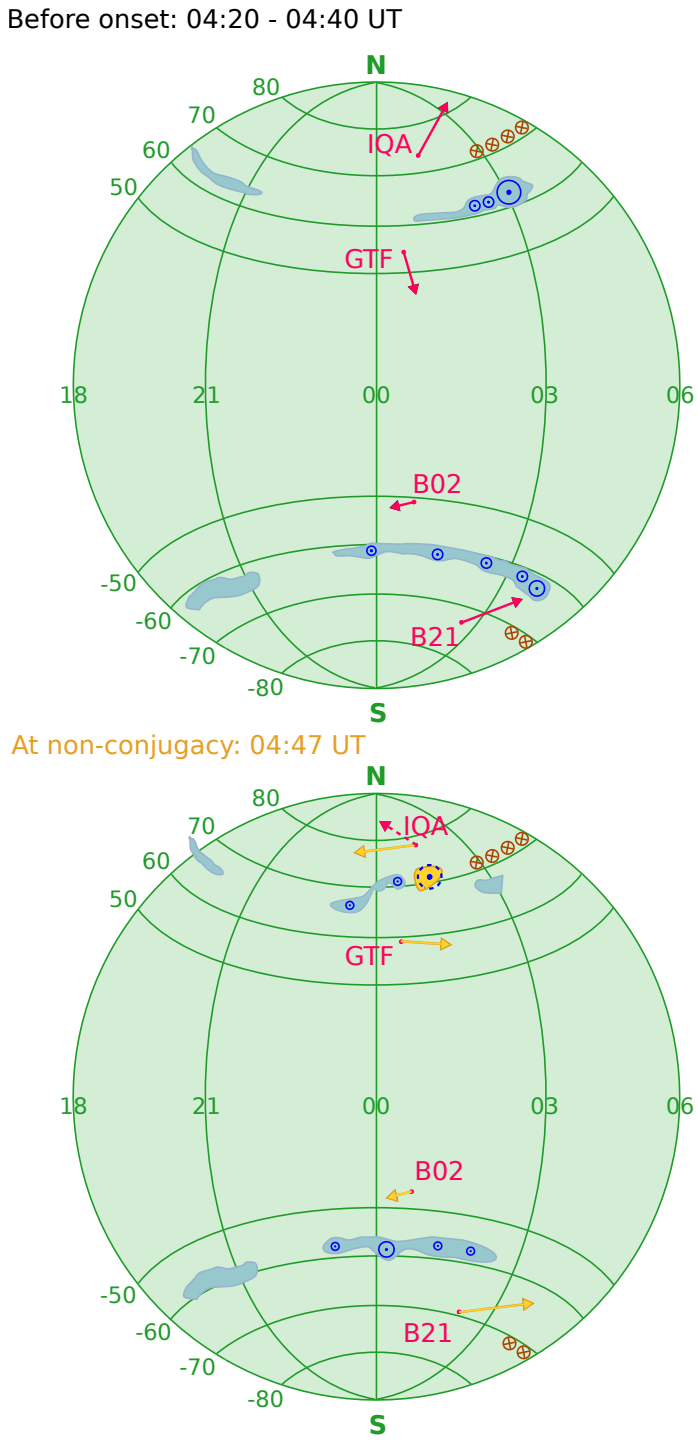

Figure 5.17: Sketch of the aurora and observed magnetic perturbations field at ground magnetometer stations for the event of November 3rd 2002. The upper panel shows the proposed system of field aligned currents causing the aurora and magnetic perturbations in the time span from 04:20 UT to 04:40 UT, before substorm onset. Ground magnetometer stations and the associated measurements are shown in red. Upward field aligned currents are indicated in blue, while brown arrows show the proposed downward field aligned currents. The lower panel is similar, but shows the proposed current systems at 04:47 UT. The magnetic perturbation measurements are shown in yellow for this time. The dashed red arrow at IQA in the northern hemisphere shows the magnitude and direction of the magnetic perturbation at 04:45 UT, two minutes prior to the arrow indicated in yellow, to highlight the change of direction that occurred at this station.

R1/R2 pattern, consistent with our placements of the postulated *R1* currents. At the equatorward station B02, the direction of the horizontal magnetic perturbation field is consistent with an upward field aligned current in the auroral oval, consistent with arguments presented in Chapter 4.4. Likewise, at GTF, in the northern hemisphere, the horizontal ground magnetic perturbation is consistent with an upward field aligned current in the area of the observed aurora, indicated by the blue circles.

The bottom panel of Figure 5.17 is similar to the top panel, but shows a sketch of the proposed field aligned currents during the observed non-conjugate auroral feature indicated in yellow. The light blue auroral features are sketches of the observed aurora at 04:47 UT (Figure 5.10). The yellow shape represents the non-conjugate, transient auroral feature as visible in the Polar VIS image, while the yellow arrows indicate the measured horizontal ground magnetic perturbation field at 04:47 UT. The dotted blue arrow out of the plane indicates the enhanced field aligned current with its footpoint in the non-conjugate auroral feature. The dashed red arrow shows the direction and magnitude of the magnetic perturbation measured at 04:45 UT, two minutes prior to the measurement indicated by the yellow arrow. In the conjugate satellite images in Figure 5.12 we see that, while the pre-onset aurora was centered around 3 MLT, the substorm onset is centered around 00 MLT in the northern hemisphere and 00 MLT $+\Delta MLT$ in the southern hemisphere. The horizontal magnetic perturbation measurements in the southern hemisphere are consistent with an upward field aligned current in the auroral oval after substorm onset and during the substorm. At B02, in the equatorward region, we see no significant change in the direction of the horizontal magnetic perturbation field. In the poleward region of the southern hemisphere we observe a southward turning of the horizontal magnetic perturbation field, likely a response to the expansion and intensification of the aurora in the auroral oval, especially around 01 MLT, during the substorm. Comparing the upper and lower panel of Figure 5.17, the westward turning of the horizontal magnetic perturbation field at IQA mentioned above, is evident. As the aurora intensifies and expands during substorm onset at 04:40 UT, the horizontal magnetic perturbation field at IQA turns in a response to the enhanced field aligned currents with footpoints in the auroral oval. The evolution at IQA is clearly seen in the ground magnetic measurements (Figure 5.14 middle panel) and in the satellite images in the right panel of Figure 5.12 where IQA is the poleward station around 73° latitude. At 04:45 UT we see a small enhanced southward turning in the northward component. We indicate the magnetic perturbation measurement at 04:45 UT by a red dashed arrow, to highlight the subsequent change. As this change is simultaneous to the appearance of the non-conjugate feature, and absent in the measurement from the southern hemisphere, it is a possible signature of the currents associated with the non-conjugate feature. However, the small response at IQA occurs as a slight deviation from a response we largely attribute to substorm onset. At GTF, in the equatorward region, we see a clear response to the substorm onset at 04:40 UT in the eastward component, reaching a maximum at 04:46 UT and decreasing slightly after that (see Figure 5.15 middle panel). We do not observe a corresponding response in the southern hemisphere. We attribute the observed signature in the northern hemisphere to the auroral activity starting at substorm onset. We note that the substorm onset in the southern hemisphere is more elongated and spreads over a larger region, and a less distinct signature of substorm onset is

therefore expected to some extent. Because a substorm onset signature is absent in the southern hemisphere, the asymmetry of the two magnetic signatures at GFT and B02, may be due to a combination of the more restricted extent of substorm onset and the non-conjugate auroral feature in the northern hemisphere. This is however not distinctly evident in the measurements. In total we observe one response at IQA, that is possible signature of asymmetric field aligned currents associated with the non-conjugate auroral feature. However, the signature is small and in the same direction as the change we attribute to substorm onset. Thus, we can not draw confident conclusions for this event.

5.1.3 Event of July 2nd 2001

5.1.3.1 Observations

The event of July 2nd 2001 is presented in the following section. Figure 5.18 shows the conjugate image pair from the two satellite imagers IMAGE WIC (upper panel) and Polar VIS Earth (lower panel), obtained at 04:41 UT, in the same format as Figure 5.1. *Reistad et al.* [2013] reported two separate non-conjugate auroral features for this event. The first is seen as an elongated shape in the southern hemisphere, which is absent in the northern. The second is seen in the area from 03 MLT to 04 MLT in the northern hemisphere. As the coverage by Polar VIS Earth of the conjugate region in the southern hemisphere is limited in the beginning of the data set it is not possible to determine the exact time of appearance for the second feature. Thus, we will focus on the non-conjugate feature observed in the southern hemisphere between 23 MLT and 00 MLT. We indicate the feature with a blue shape as before. The asymmetry occurred during the recovery phase of a substrom with an onset at 04:29 UT in the winter hemisphere. *Reistad et al.* [2013] attributes the non-conjugate feature to the solar wind dynamo effect (see Chapter 2.3.1). It is first clearly visible around 23-00 MLT, in the images obtained at 04:39 UT and last in the image obtained at 04:43 UT.

The IMF and geomagnetic conditions are summarized in Figure 5.19, presented in the same format as Figure 5.2. The B_y component, shown in green, dominated the IMF with steady values around -9nT. The B_x and B_z component of the IMF, shown in orange and pink, are steady at 3nT and 1nT, respectively, for the duration of this event. The AE index, shown in black, fluctuated and was approximately at 320nT at the time of the observed asymmetry. The vertical red lines at 04:39 UT and 04:43 UT indicate the time and duration of the non-conjugate auroral feature, while the dashed blue line indicates the time of substorm onset [*Frey and Mende*, 2006].

Figure 5.20 shows five conjugate image pairs obtained in the time span from 04:35 UT to 04:43 UT on July 2nd 2001. The first panel shows the conjugate pair obtained at 04:35 UT, before the non-conjugate auroral feature is clearly visible. At 04:37 UT, shown in the second panel, the elongated auroral feature around midnight MLT in the southern hemisphere intensifies. However, at this time it is difficult to tell from the satellite images alone whether the auroral feature in the southern hemisphere is non-conjugate, as the conjugate feature in the northern hemisphere between 1 and 2 MLT shows a somewhat similar, slightly elongated auroral shape on the poleward

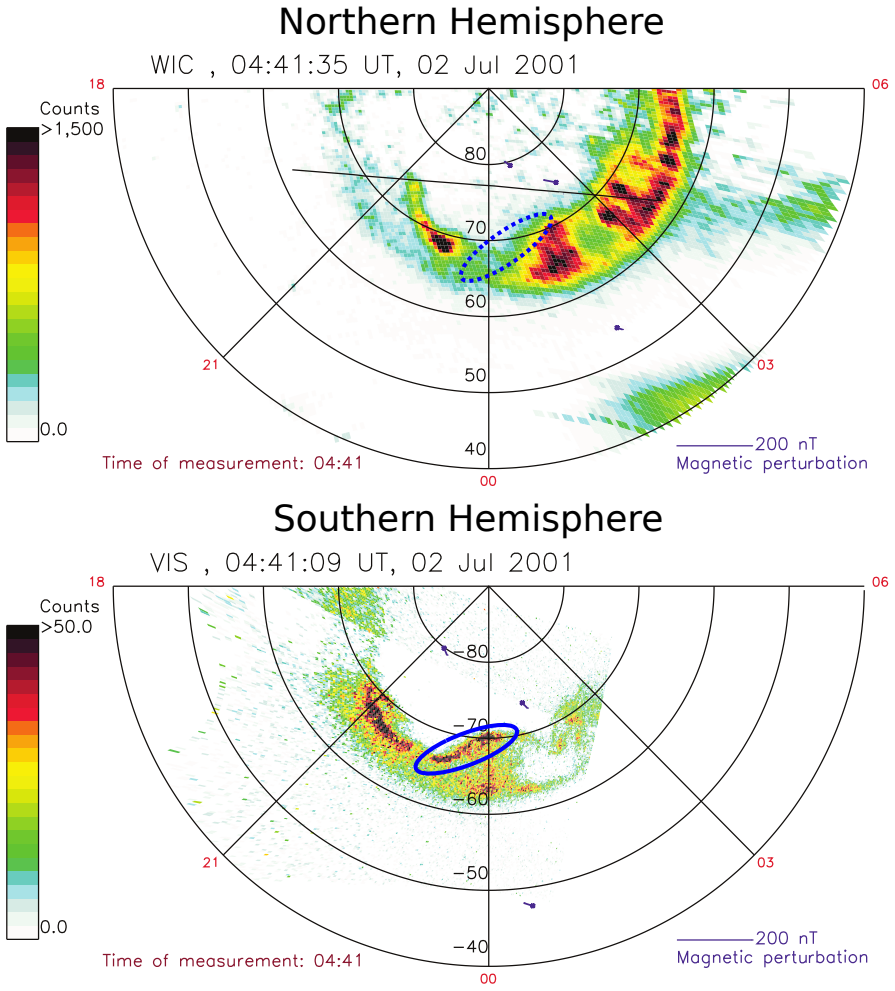

Figure 5.18: Conjugate image pair from IMAGE WIC (upper panel) and Polar VIS Earth (lower panel) obtained at 04:41 UT on July 2nd 2001. The blue ring indicates the non-conjugate auroral feature in the northern hemisphere identified by *Reistad et al.* [2013]. The dashed ring indicates the conjugate area. Purple lines show the SuperMAG magnetic perturbation field vector at the time of the image. The exact time of the exposure of the images is shown at the top of each image while the exact time of the magnetic measurement is shown in the lower left corner of the figure. A unit vector is shown in the lower right corner of each image.

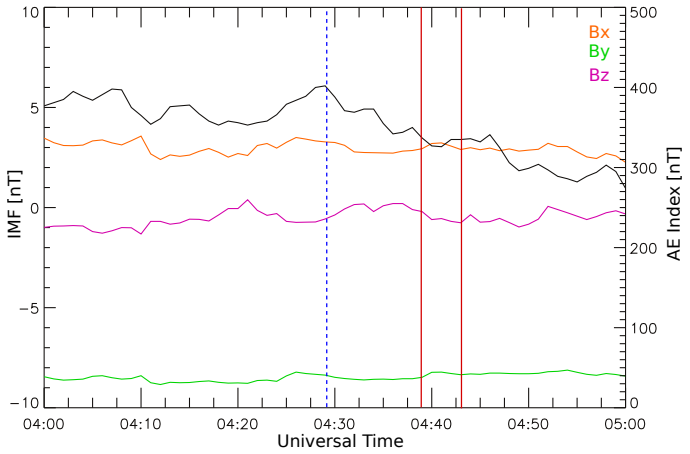

Figure 5.19: The IMF and geomagnetic conditions on July 2nd 2001. The dashed blue line indicates the time of substorm onset, solid red lines indicate the appearance and disappearance of the non-conjugate auroral feature. The x, y and z components of the IMF are shown in orange, green and pink, respectively. The black line shows the *AE* index with the scale indicated on the right axis.

edge. The third panel shows the first conjugate image pair where the non-conjugate feature is clearly identifiable at 04:39 UT. The elongated auroral feature visible in the southern hemisphere, is not visible at the poleward edge in the northern conjugate hemisphere. The fourth panel show the same image pair as in Figure 5.18, obtained at 04:41 UT. The bottom panel is obtained at 04:43 UT. This is last image pair in which the non-conjugate auroral feature is still clearly visible in the southern hemisphere. Consequently, we define the end time of the non-conjugate auroral event to be at 04:43 UT, in the following analyses.

Figure 5.21 is in the same format as Figure 5.4 and shows the map of the northern hemisphere, with the used SuperMAG stations for this event, rotated and projected onto a similar map of the southern hemisphere. The calculated ΔMLT for this event is -1.3 [*Reistad et al.*, 2013]. We indicate a sketch of the non-conjugate auroral feature by a dashed pink shape. There are no stations within the auroral oval for this event, but two conjugate station pairs in the poleward region. The identified conjugate station pairs for this event are:

Poleward region 1 : CY0 and SBA

Poleward region 2 : ATU and SPA

Equatorward region : STJ and LIV

Poleward stations SBA and CY0

All components of the ground magnetic perturbation field at the two stations, CY0 and SBA, shown in Figure 5.22 are small in magnitude. This is likely due to the distance between the stations and the auroral oval, with SBA being $\sim$ 800km further into the polar cap. The northward component of the station in the northern

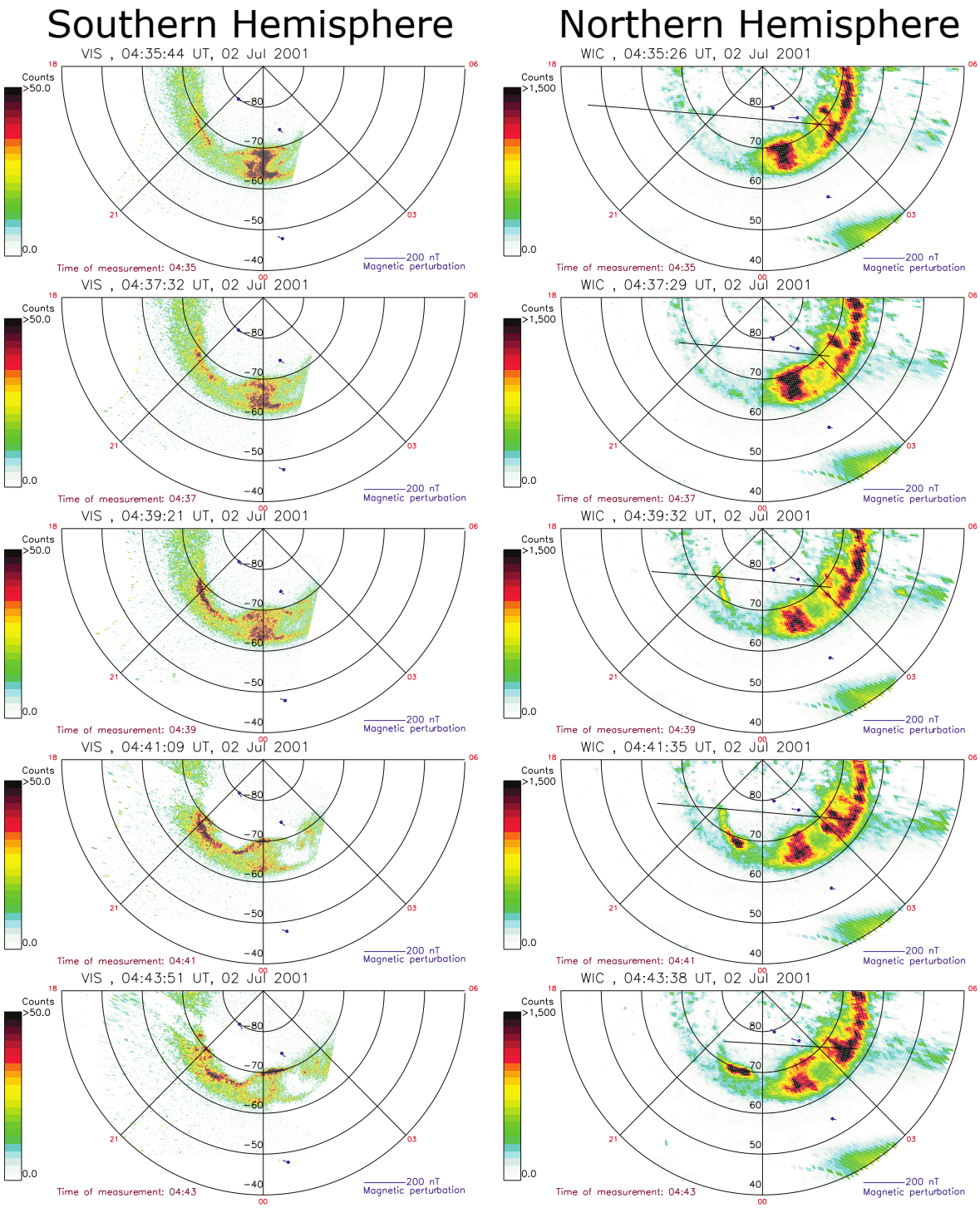

Figure 5.20: Conjugate image pairs obtained in the time span from 04:35 UT to 04:43 UT on July 2nd 2001. Purple lines show the SuperMAG magnetic perturbation field vector at the time of the image.

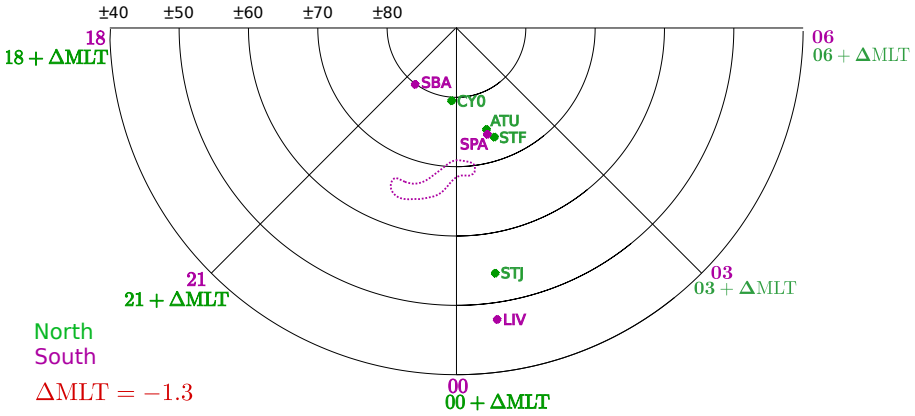

Figure 5.21: Map of the Southern Hemisphere in magnetic AACGM coordinates at 04:41 UT on July 2nd 2001, indicating relevant SuperMAG stations used for this event. Stations in the northern hemisphere, shown in green, are projected onto the map and rotated by $\Delta\text{MLT} = -1.3$. The stations in the southern hemisphere are shown in pink. Each concentric circle indicates the magnetic latitude for the northern hemisphere (positive values) and the southern hemisphere (negative values). MLT values are shown for both hemispheres, green for north and pink for south. Conjugate station pairs for this event are SBA and CY0, SPA and ATU, and LIV and STJ. The pink dotted line shows the approximate outline of the non-conjugate aurora observed in the southern hemisphere.

hemisphere, CY0, is steady around 15nT. At SBA, in the southern hemisphere the northward component fluctuates slightly more around a value of 10nT. For the duration of the non-conjugate auroral feature we observe a small local maximum in this component with a magnitude of 5nT. The eastward component at CY0 is stable around -10nT, while at SBA we observe a slight increase from 15nT to 20nT at the time of the non-conjugate feature. At CY0, in the northern hemisphere, we see a decrease in the eastward component from 0nT at 04:20 UT to a minimum of −15nT at 05:10 UT, with no fluctuations or changes occurring during the time interval of the observed non-conjugate auroral feature. At SBA, slight fluctuations around 15nT are observed in the northward component. The total direction of the horizontal ground magnetic perturbation field in the southern hemisphere is consistent with an upward field aligned current, considering the arguments in Chapter 4.4. In the northern hemisphere the observe direction of the total horizontal magnetic perturbation field at CY0, also corresponds to an upward field aligned current.

The vertical component at CY0 is approximately 5nT for the duration of the non-conjugate auroral feature observed in the southern hemisphere. This is the only time interval with downward directed vertical component at this station. Before and following the non-conjugate auroral feature this component is negative and fluctuating between −10nT and −5nT. Simultaneously the vertical component SBA station shows a gradual decrease from 5nT to −5nT.

Poleward stations ATU and SPA

Figure 5.23 show SuperMAG measurements of the two stations, ATU and SPA, positioned around ±74° latitude close to midnight at the time of the observed non-

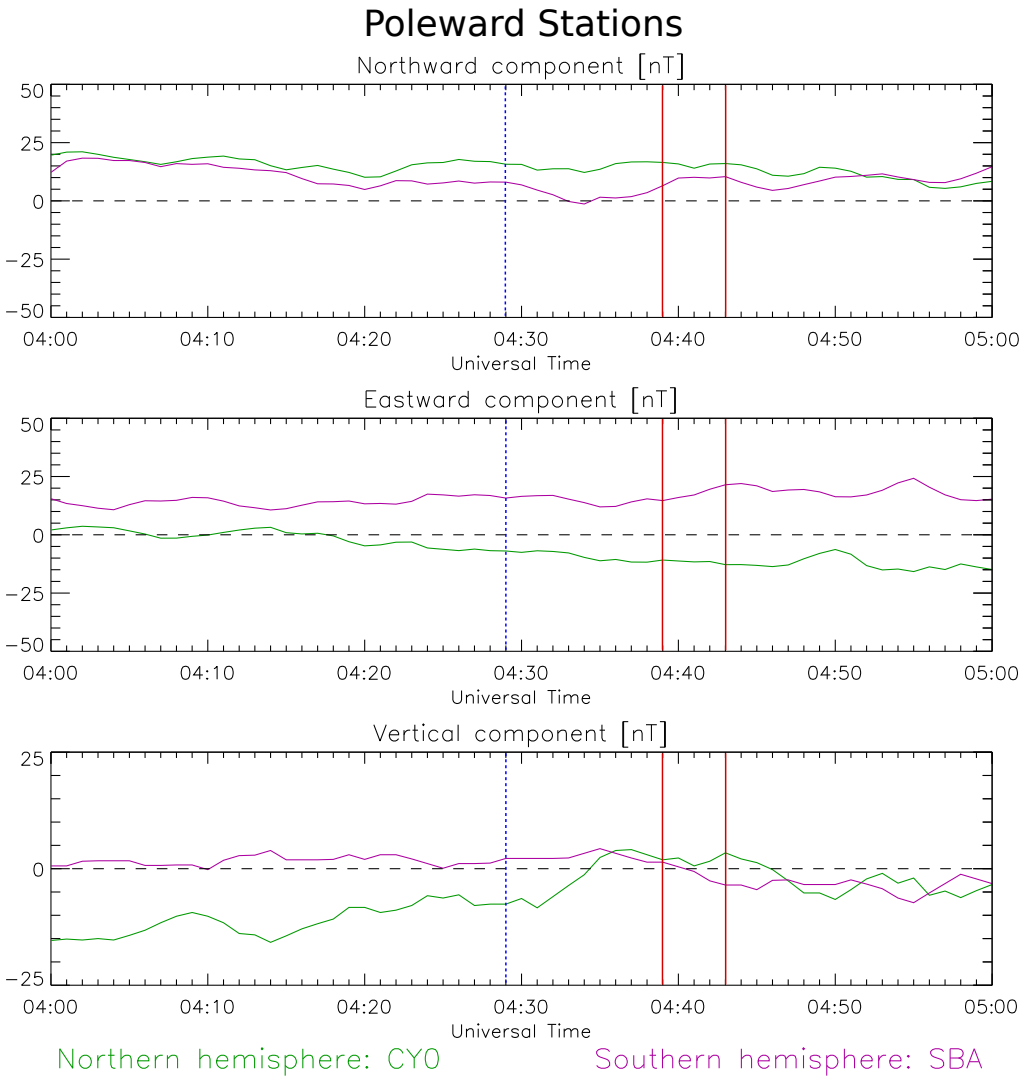

Figure 5.22: Poleward conjugate stations SBA and CY0 around the midnight sector on July 2nd 2001. The dashed blue line indicates the time of substorm onset, while solid red lines indicate the appearance and disappearance of the non-conjugate auroral feature.

conjugate auroral feature. The northward component at both stations is slowly decreasing from 30nT to 0nT, in the time span form 04:00 UT to 05:00 UT. They show a very similar evolution in time except for a small increase and subsequent decrease of 10nT in the time span from 04:36 UT to 04:40 UT at ATU, in the northern hemisphere. The eastward component at both stations is shown in the middle panel. Measurements at SPA fluctuate around 0nT. At 04:31 UT an increase to a local maximum value of 20nT occurs. After fluctuating for approximatley 18 minutes a decrease to 0nT occurs. At ATU values fluctuated around -25nT. Similar to the observations in the other polward region at, CY0 and SBA, the total horizontal direction of the ground magnetic perturbation field is consistent with an upward field aligned current in the northern hemisphere and an upward field aligned current in the southern hemisphere.

The vertical components at both stations, shown in the bottom panel of Figure 5.23, show a very similar evolution only separated by a difference in magnitude of approximately 50nT. At ATU the vertical component has an increase of 20nT superimposed onto a gradual increasing trend. We note that both are positive with the largest values in the southern hemisphere.

Equatorward stations STJ and LIV
The STJ and LIV station are located well outside the auroral oval towards the equator in both hemispheres. Measurements obtained from these stations are show in Figure 5.24. The northward component at both stations is steady around -10nT. No variations in relation to the observed non-conjugate auroral feature are clearly visible. The eastward component at STJ, in the northern hemisphere, increases gradually from 5nT to 15nT in the time span of one hour, starting at 04:00 UT. In the southern hemisphere, the eastward component is steady around -20nT. The total direction of the ground magnetic perturbation field in the northern hemisphere consistent with an upward field aligned current. The same is true for the southern hemisphere.

The vertical components displayed in the bottom panel of Figure 5.24 show little variation. In the southern hemisphere the observed vertical perturbation field is approximately 2nT. The northern hemisphere is steady at 5nT from 04:00 UT 04:30 UT where an increase to 10nT and a subsequent decrease to 0nT at 04:52 UT, is observed. The increase and subsequent decrease does not coincide with the non-conjugate aurora feature observed in the southern hemisphere.

5.1.3.2 Interpretation

An interpretation of the non-conjugate auroral event that occurred on July 2nd 2001 is presented in Figure 5.25. The Figure is in the same format as Figure 5.8. In the upper panel, the ground magnetic perturbation field at the SuperMAG magnetometer stations and the proposed field aligned currents are shown at 04:35 UT. The lower panel is identical but shown at at 04:41 UT, the time when the non-conjugate auroral feature is most clearly seen in the satellite images. A sketch of the non-conjugate auroral feature we focus on, is drawn in yellow, while the dashed black

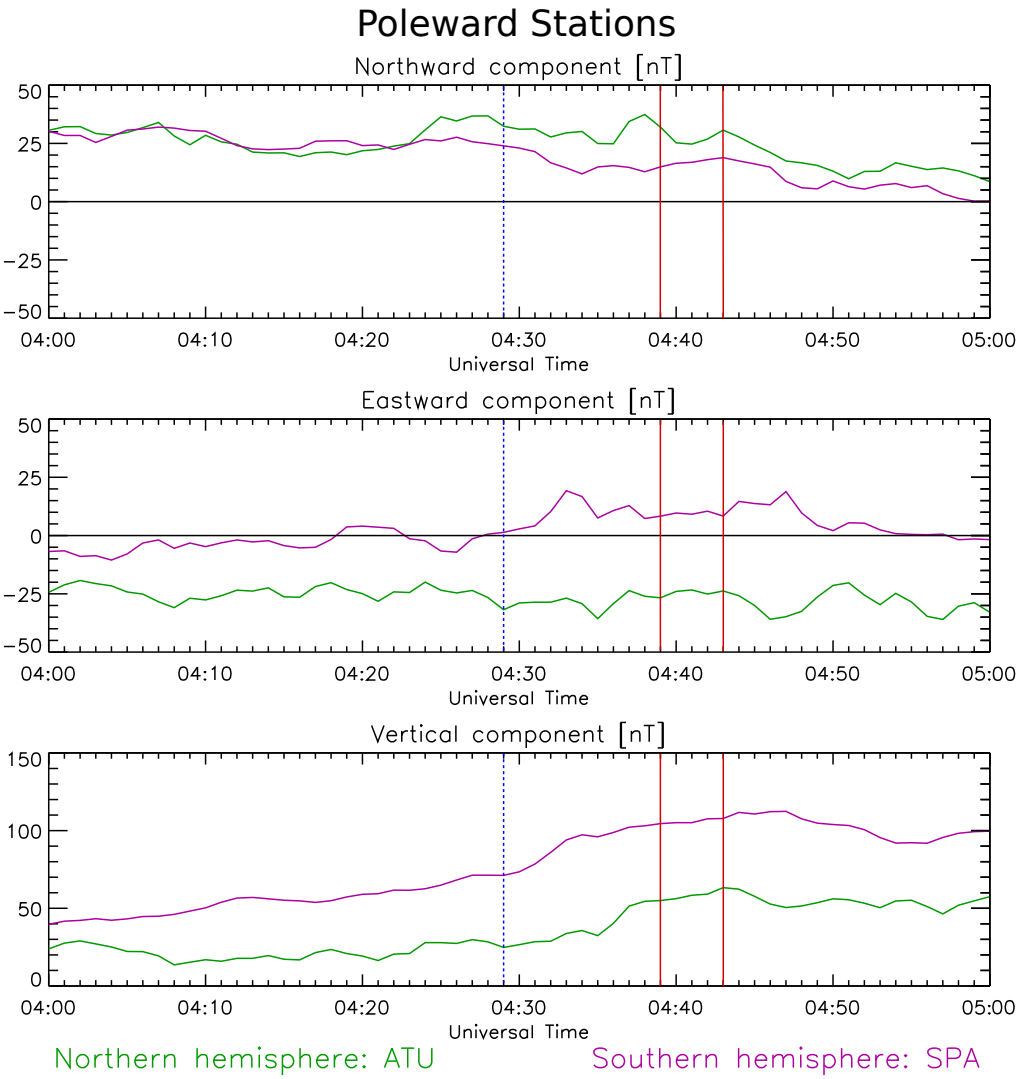

Figure 5.23: Poleward stations ATU and SPA located around midnight and ±74° latitude on July 2nd 2001. The dashed blue line indicates the time of substorm onset, while solid red lines indicate the appearance and disappearance of the non-conjugate auroral feature.

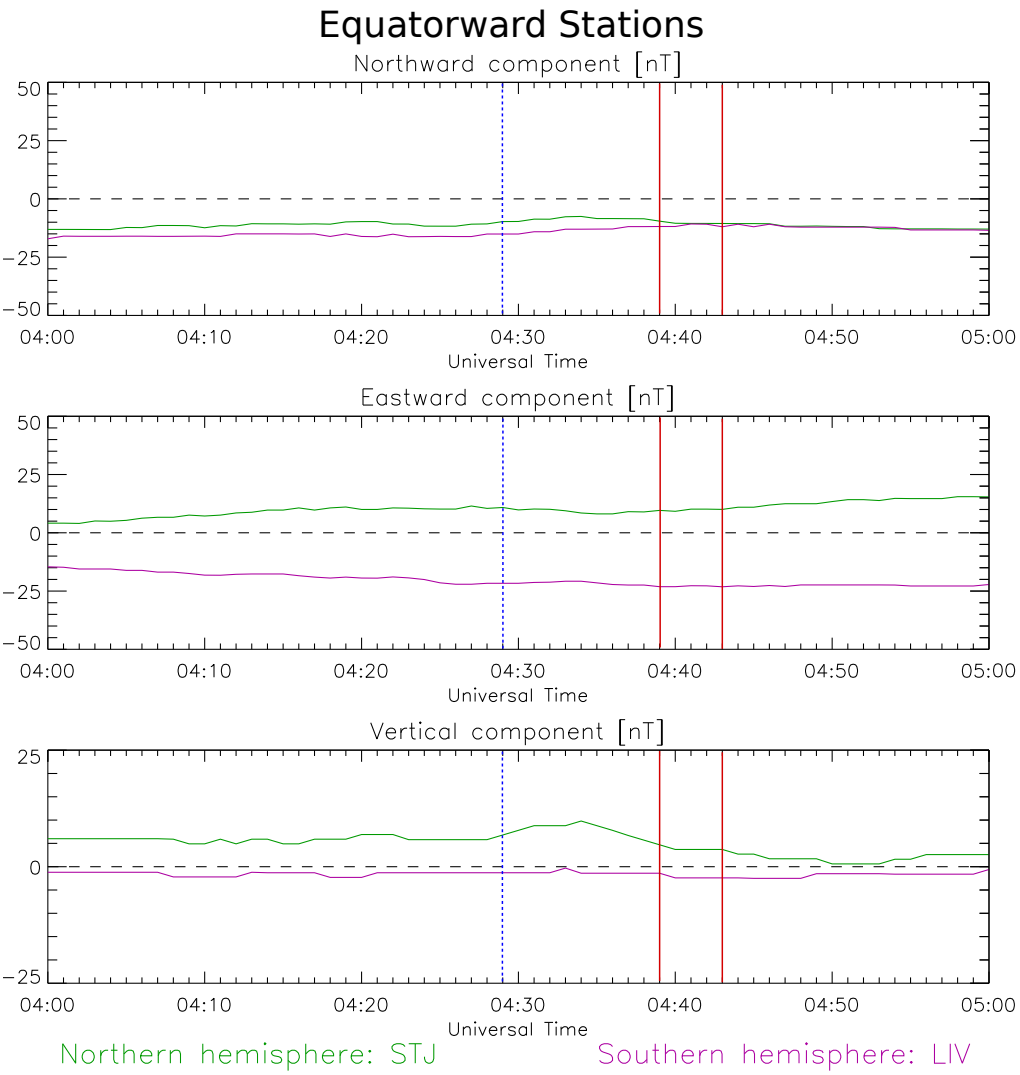

Figure 5.24: Equatorward stations STJ and LIV located around 53.6° latitude and -47.8° latitude, respectively on July 2nd 2001. The dashed blue line indicates the time of substorm onset, while solid red lines indicate the appearance and disappearance of the non-conjugate auroral feature.

line indicates the edge of the satellite image.

After substorm onset the measured ground magnetic perturbations field, is consistent with upward field aligned currents in the auroral oval in both hemispheres. The upper panel of Figure 5.25 illustrates this. As for the event on May 12th 2001, the equatorward stations in this event, show a southward component. This may indicate that the measurements here, are affected by the ring current. The direction of the vertical components at the equatorward stations supports this. However, the average value of the *Sym-H* index for the duration of the non-conjugate auroral event is -13 nT, indicating low activity in the ring current.

The bottom panel shows our interpretation of the field aligned currents for the duration of the non-conjugate auroral feature. There are no clear signatures in the measured horizontal ground magnetic perturbation field at any stations related to the non-conjugate auroral feature appearing in the southern hemisphere. Only minor changes or fluctuations are observed at all stations. At the poleward stations ATU and SPA we observe strikingly similar fluctuations in the eastward component, however in opposite directions and at an offset of about 25nT. The reason for the offset is unknown.

It is possible that we do not observe clear signatures of any non-conjugate field aligned currents during the present event, as the non-conjugate auroral feature has a small spatial extent compared to the non-conjugate features of the events presented earlier. In addition local magnetic variations are known to exist in the vicinity of the SBA station in the southern hemisphere [*Adams and Christoffel*, 1962; *Cullington*, 1968]. This may considerably affect the measurements.

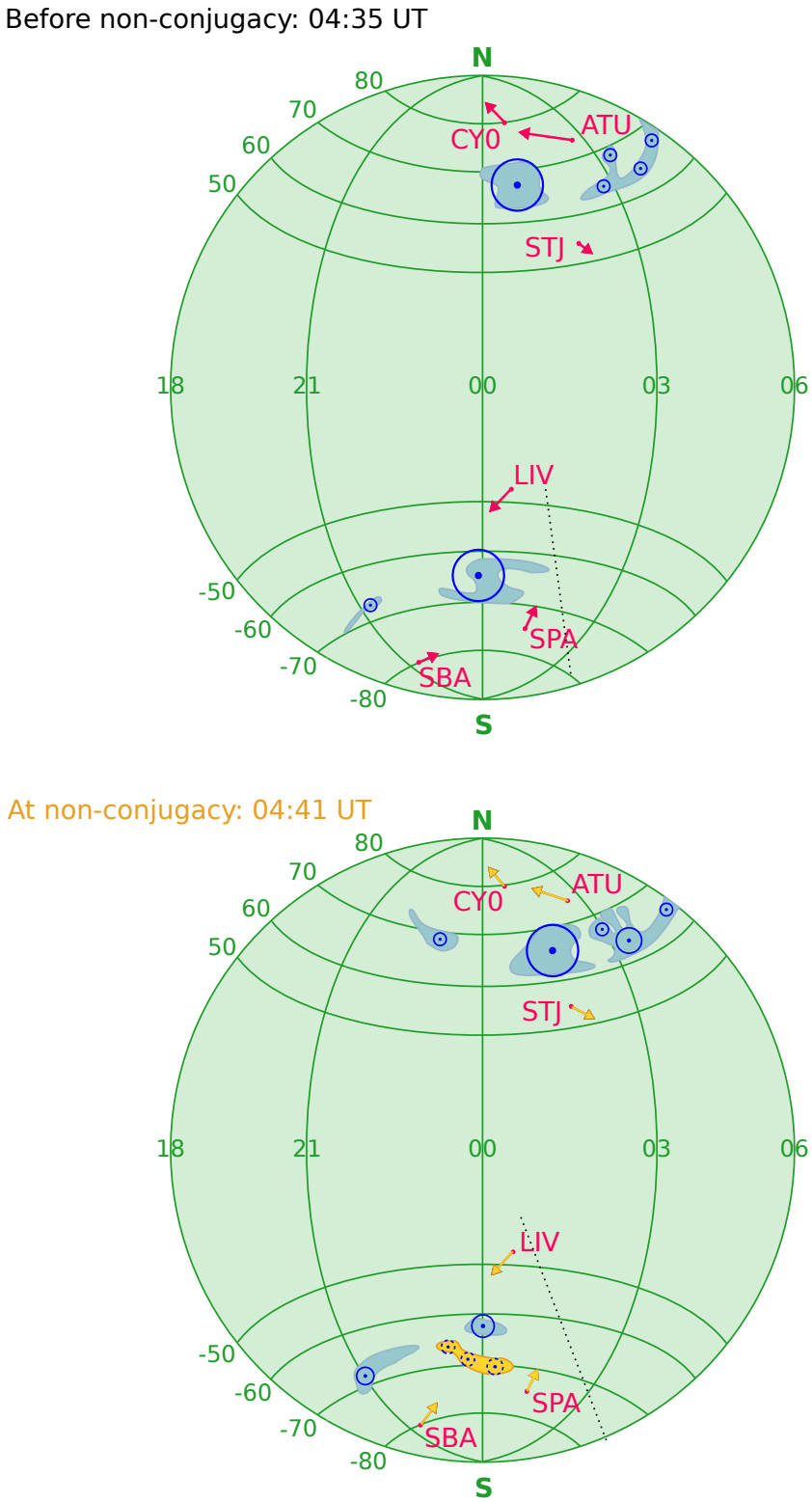

Figure 5.25: Proposed field aligned currents before and during non-conjugate auroral event on July 2nd 2001. The upper panel shows the proposed system of field aligned currents causing the aurora and magnetic perturbations 04:35 UT. Ground magnetometer stations and the associated measurements are shown in red. Upward field aligned currents are indicated in blue. The lower panel is similar, but shows the proposed current systems at 04:41 UT. The magnetic perturbation measurements are shown in yellow for this time. The dashed line indicates the FOV of the VIS image from the southern hemisphere.

5.1.4 Event of July 5th 2001

5.1.4.1 Observations

In the following section we present the event of July 5th 2001. Two non-conjugate auroral features were observed around 05:52 UT in the evening sector of the southern hemisphere [*Reistad et al.*, 2013].

Figure 5.26 shows the conjugate image pair obtained at 05:52 UT, where we indicate the non-conjugate features in blue rings and label them 1 and 2. The dashed circles show the conjugate areas in the opposite hemisphere. In the southern hemisphere we observe an intense wavelike structure in the evening sector, between 20 -23 MLT, that is not visible in the northern hemisphere. A second non-conjugate auroral feature is observed in the northern hemisphere, in the dusk/evening sector. A small auroral spot is visible between 20 and 21 MLT, around 70° latitude, that is absent in the southern hemisphere. We label the two features 1 and 2. *Reistad et al.* [2013] reports Feature 1 as consistent with the Solar Wind dynamo generator mechanism while Feature 2 is not consistent with any of the proposed generator mechanisms for non-conjugate aurora. In the present thesis we focus on Feature 1 as it has a larger spatial extent and is closer to the available conjugate SuperMAG station pairs. Unless otherwise indicated, the following presentation of data and interpretations will refer to Feature 1.

Figure 5.27 summarizes the IMF and geomagnetic conditions during this event. At the time of the observed asymmetry the AE index, indicated in black, was 320nT. The IMF B_x was steady around 6nT while B_y fluctuated slightly between -5nT and -7nT during the non-conjugate auroral event. The B_z component was negative with one short northward turning just prior to the observed non-conjugate auroral feature. *Frey and Mende* [2006] report a substorm onset at 03:34 UT and at 06:04 UT, well before and after the observed non-conjugate auroral features appear. We indicate the second onset by a dashed blue line. Vertical red lines indicate the time span where the non-conjugate auroral feature is visible in the satellite images. The first conjugate satellite image pair, obtained at 05:52 UT, where the non-conjugate feature is visible is also the first image pair of simultaneous images from both hemispheres. We do not have a sufficient field of view in the satellite images of the southern hemisphere prior to this. Consequently, we do not have an unambiguous time span where the non-conjugate auroral features begin for this event.

Figure 5.28 is a time series of five conjugate image pairs from the satellite imagers VIS (left column) and WIC (right column). The first panel shows the conjugate image pair obtained at 05:52 UT. The non-conjugate auroral feature observed in the southern hemisphere is clearly visible between 20 and 23 MLT in the left panel. Each successive panel displays a conjugate image pair with two minute cadence (except for the bottom panel which is obtained 3 minutes after the previous image pair), showing the development of the non-conjugate auroral feature in the southern hemisphere. From this image series we identify the interval of the non-conjugate auroral feature to be from 05:52 UT to 05:56 UT.

The ΔMLT for this event, calculated by *Reistad et al.* [2013], is $\Delta\text{MLT} = 0.4$, and

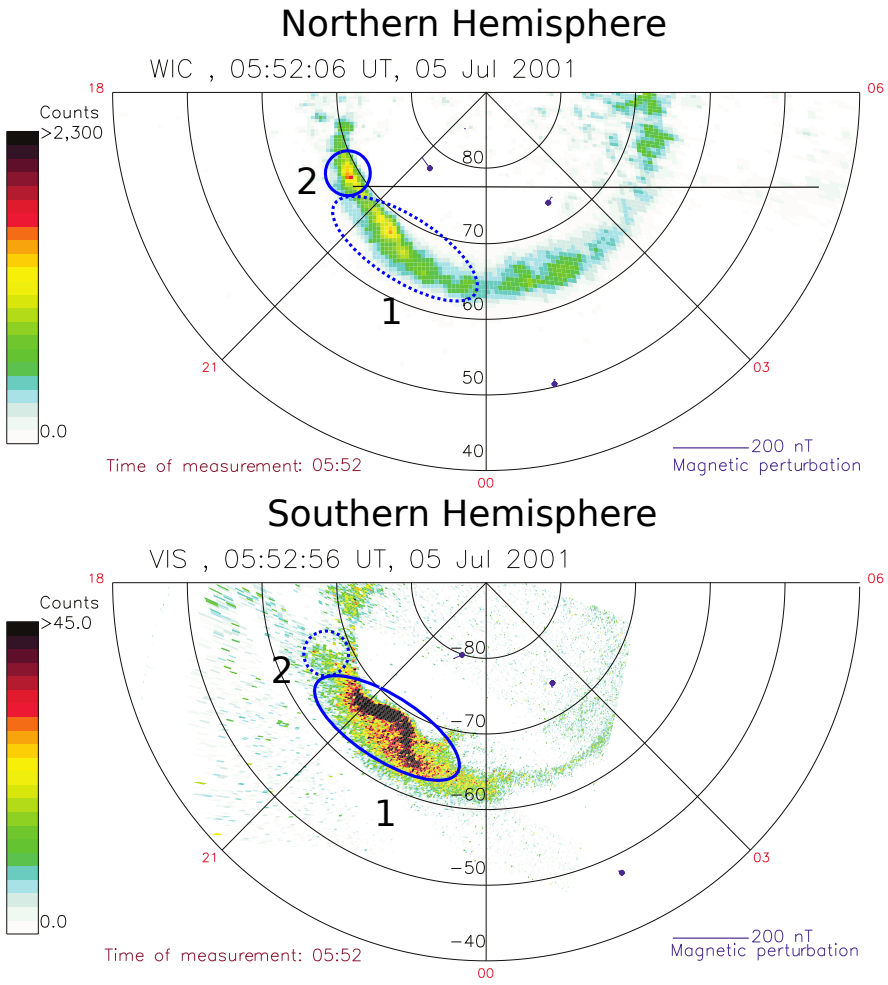

Figure 5.26: Conjugate image pair from IMAGE WIC (upper panel) and Polar VIS Earth (lower panel) obtained at 05:52 UT on July 5th 2001. The blue rings indicate the non-conjugate auroral features in the northern and southern hemisphere identified by *Reistad et al.* [2013]. The dashed rings indicate the conjugate areas. Purple lines show the SuperMAG magnetic perturbation field vector at the time of the image. The exact time of the exposure of the images is shown at the top of each image while the exact time of the magnetic measurement is shown in the lower left corner of the figure. A unit vector is shown in the lower right corner of each image.

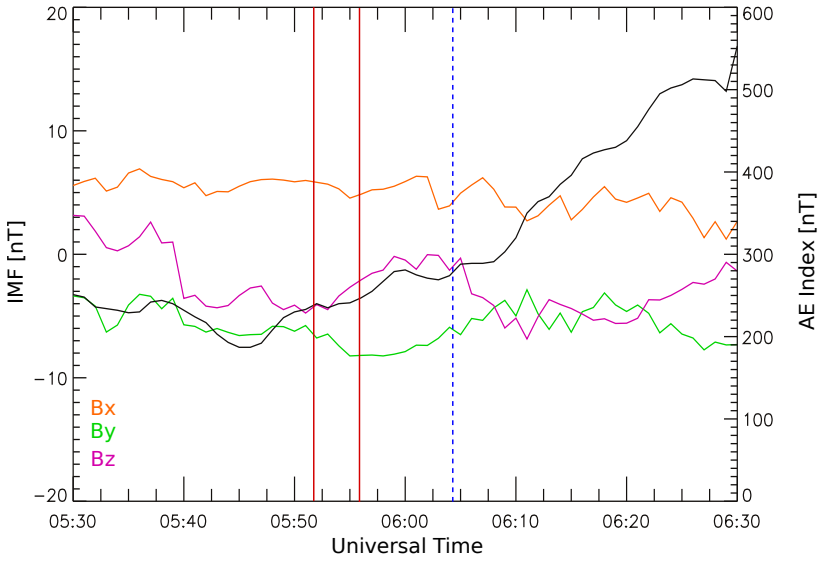

Figure 5.27: IMF and geomagnetic condition on July 5th 2001. The solid red lines indicate the appearance and disappearance of the non-conjugate feature, while the dashed blue line indicates substorm onset. The x, y and z components of the IMF are shown in orange, green and pink, respectively. The black line shows the *AE* index with the scale indicated on the right axis.

in Figure 5.29 we show a map of the rotated northern hemisphere projected onto the southern hemisphere to identify conjugate SuperMAG stations, similar to Figures 5.4, 5.13 and 5.21. Note that there are no stations in the auroral oval region. Also, the equatorward stations for this event are more than 3 hours MLT and 10° latitude away from the observed non-conjugate auroral features. We identify the following conjugate station pairs from Figure 5.29:

Poleward region 1 : CBB and SBA

Poleward region 2 : IQA and SPA

Equatorward region : APL and LIV

Poleward stations CBB and SBA

Figure 5.30 is in the same format as 5.5 and shows the northward, eastward and vertical components of the two conjugate stations CBB and SBA, poleward of the observed non-conjugate auroral feature. CBB at a magnetic latitude of 77.22° is closer to the conjugate region than SBA at -79.91°. The northward components at both stations, shown in the upper panel, show a very similar development. Measurements at both stations are stable around 0nT until 05:40 UT before gradually increasing. The eastward component at CBB is steady around -35nT for the time span of conjugate image pairs. In the southern hemisphere at SBA the eastward component is steady around -15nT for the same time interval. The direction of the total horizontal ground magnetic perturbation field at SBA in the southern hemisphere is somewhat consistent with a downward field aligned current. At CBB in the

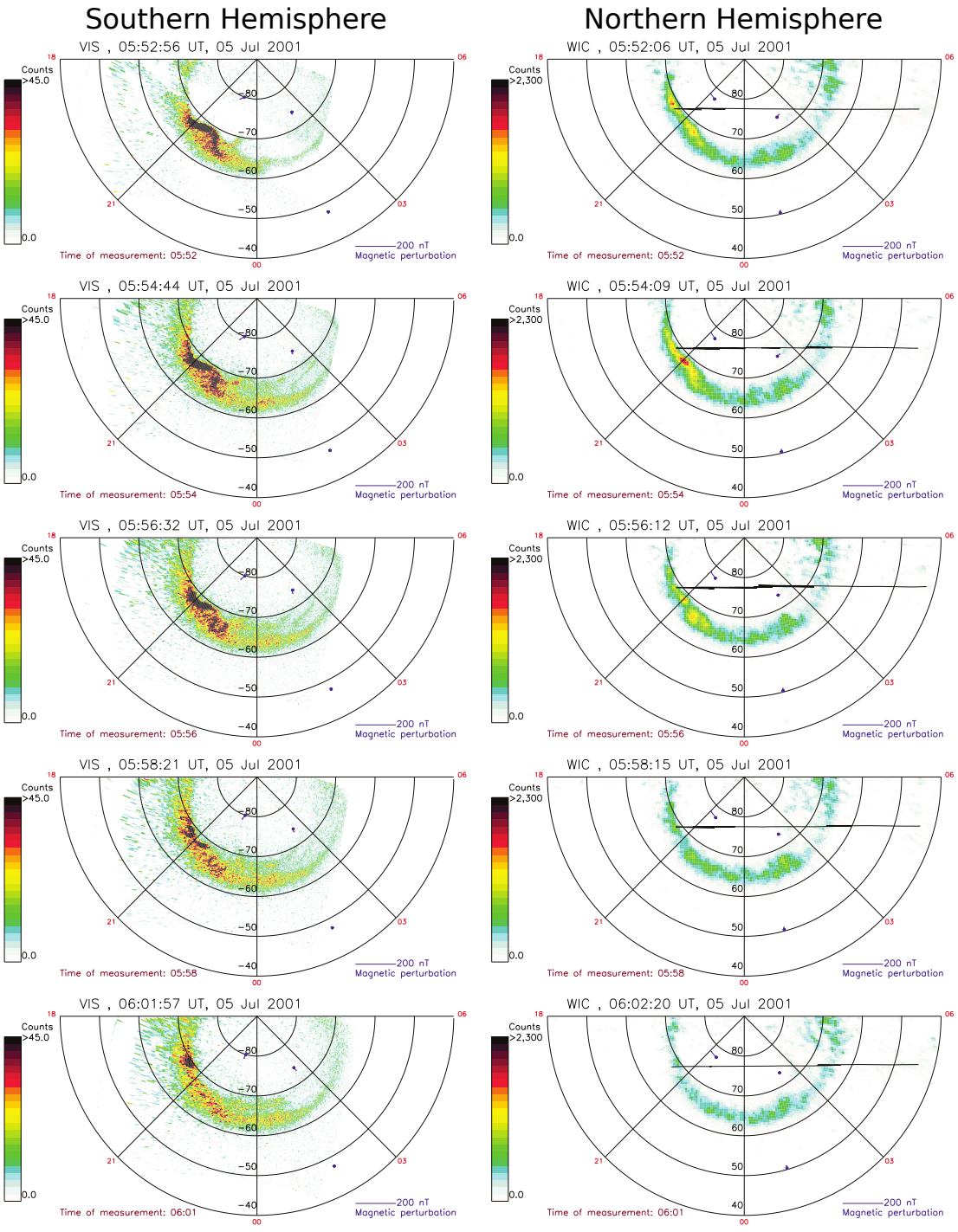

Figure 5.28: Conjugate image pairs obtained in the time span from 05:52 UT to 06:01 UT on July 5th 2001. Purple lines show the SuperMAG magnetic perturbation field vector at the time of the image.

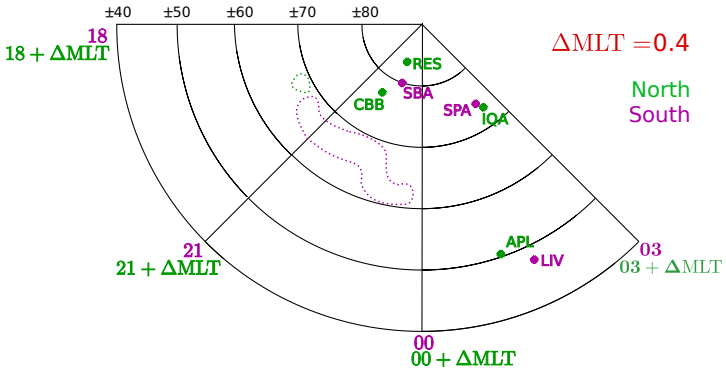

Figure 5.29: Map of the southern hemisphere where the northern hemisphere is rotated by ΔMLT and projected onto a map of the southern hemisphere on July 5th 2001. Each concentric circle indicates the magnetic latitude for the northern hemisphere (positive values) and the southern hemisphere (negative values). MLT values are shown for both hemispheres, green for north and pink for south. The dashed shapes indicate the observed non-conjugate auroral features. Their color indicates the hemisphere in which they are observed. Conjugate station pairs for this event are CBB and SBA, IQA and SPA and APL and LIV.

northern hemisphere we see signatures of an upward field aligned current considering the arguments presented in Chapter 4.4. From the measurements of the horizontal ground magnetic perturbation components at CBB and SBA, shown in Figure 5.30, we do not see any clear signature of the non-conjugate aurora. However, we note the small decrease and subsequent increase in the eastward component at SBA, starting at 05:43 UT and lasting until 06:00 UT. As we do not know the exact time span for the non-conjugate auroral feature, it is a possible response to an increase of field aligned currents associated with the non-conjugate feature.

The vertical component at CBB show a steady gradual increase throughout the event. A small decrease of 5nT is observed at 05:45 UT, simultaneous to a small increase of the vertical component at SBA. At this time the evolution at SBA and CBB is in opposite directions. The increase at SBA is followed by a gradual decrease starting at 05:52 UT.

Poleward stations IQA and SPA

Figure 5.31 shows the magnetic perturbation field measurements from the two poleward stations in the post-midnight sector, IQA and SPA. As for Figure 5.30 we have drawn vertical red lines for the time of the exposure of the conjugate image pair in Figure 5.26. In the southern hemisphere, at SPA, the northward component is steady around 10nT at the time of the observed non-conjugate aurora. The eastward component at SPA is steady at approximately -7nT for the same time span. We note that is evolution is very similar to the eastward component at SBA. The total direction at this station in the southern hemisphere is consistent with an upward current in the aurora oval from the arguments presented in Chapter 4.4. In the northern hemisphere, at IQA, the northward component of the horizontal magnetic perturbation field varies from a maximum of 20nT at 05:49 UT to -25nT at 06:12

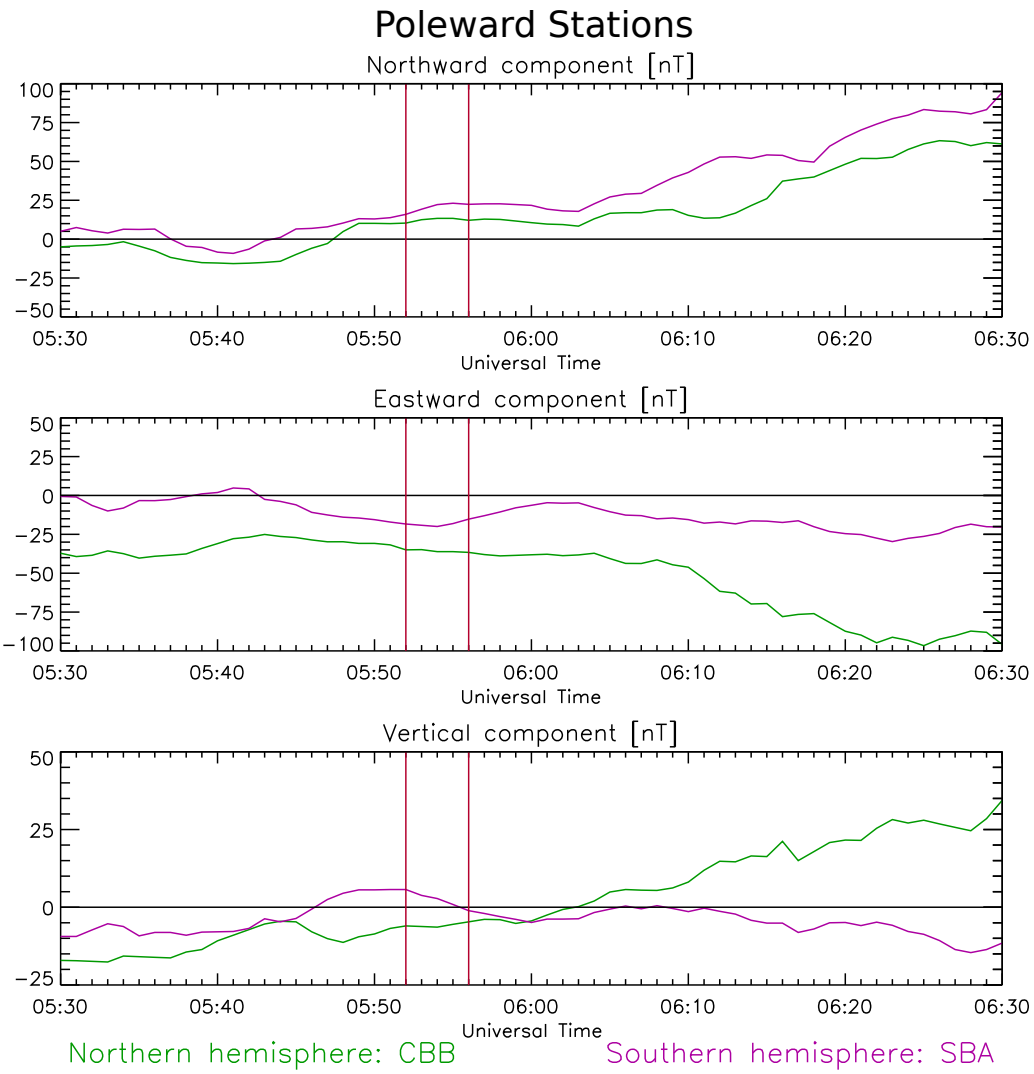

Figure 5.30: Poleward stations CBB and SBA on July 5th 2001. Vertical red lines indicate the time of the first and last conjugate satellite image pair where the non-conjugate aurora is visible. The start time of the feature is uncertain for this event as the FOV of Polar VIS is not sufficient prior to 05:52 UT.

UT. For the time span of the non-conjugate aurora, the northward component is 5nT. The eastward component at IQA has a local maximum and minimum simultaneous to the northward component. At the time of the non-conjugate aurora the eastward component is around 15nT. As we can not easily determine the beginning and end of the non-conjugate event, we are not able to say whether we do see a signature of the feature in the southern hemisphere from these plots.

The vertical components of the stations are both positive and reveal similar development with an offset of 30nT, with larger values in the northern hemisphere. Although, we see the non-conjugate feature in the southern hemisphere.

Equatorward stations APL and LIV
Figure 5.32 shows measurements of the horizontal and vertical ground magnetic perturbation field at the conjugate station pair APL and LIV, in the equatorward region. All components are very stable throughout the event in both hemispheres. In Figure 5.29, showing the conjugate station pairs and their approximate position related to the non-conjugate auroral features, we see that APL and LIV are in a different MLT sector and at a large distance from the non-conjugate auroral feature. Consequently, no response to the non-conjugate aurora is apparent. The northward component at APL is stable at 10nT for 30 minutes from 05:40 UT to 06:10 UT. At LIV the northward component is gradually increasing from -10nT at 05:30 UT to 5nT at 06:30 UT. For the time interval of conjugate satellite image pairs, indicated by the vertical red lines, the northward component at LIV is -10nT. The eastward component for the same time interval is 0nT at APL and -5nT at LIV in the southern hemisphere.

The vertical components at the two stations are equal in magnitude but opposite in direction. In the northern hemisphere we see a negative vertical component, while a positive vertical component is observed in the southern hemisphere. This is consistent with the arguments of Chapter 4.4 and expected, and it is a possible indication of a westward horizontal current in the poleward of the station.

5.1.4.2 Interpretation

As mentioned above, we have a limited number of conjugate satellite image pairs for the present event. No images are available for the time prior to the appearance of the non-conjugate aurora. As a consequence, we are not able to compare the measured ground magnetic perturbation field before and at the time of the non-conjugacy, as we have done for the previous events. Thus, we present only one figure in the following interpretation of the measurements and the associated current system. Figure 5.33 shows the proposed field aligned and horizontal currents at 05:54 UT where the intense non-conjugate aurora is sketched in yellow in the southern hemisphere.

In Figure 5.33 it is clear that the available ground magnetometer stations, especially in the equatorward region, are not in optimal positions in respect to the observed non-conjugate auroral feature in the southern hemisphere on July 5th 2001. The best positioned conjugate station pair is CBB and SBA in the poleward region. From the measurements at these stations, presented in Figure 5.30, no clear response was

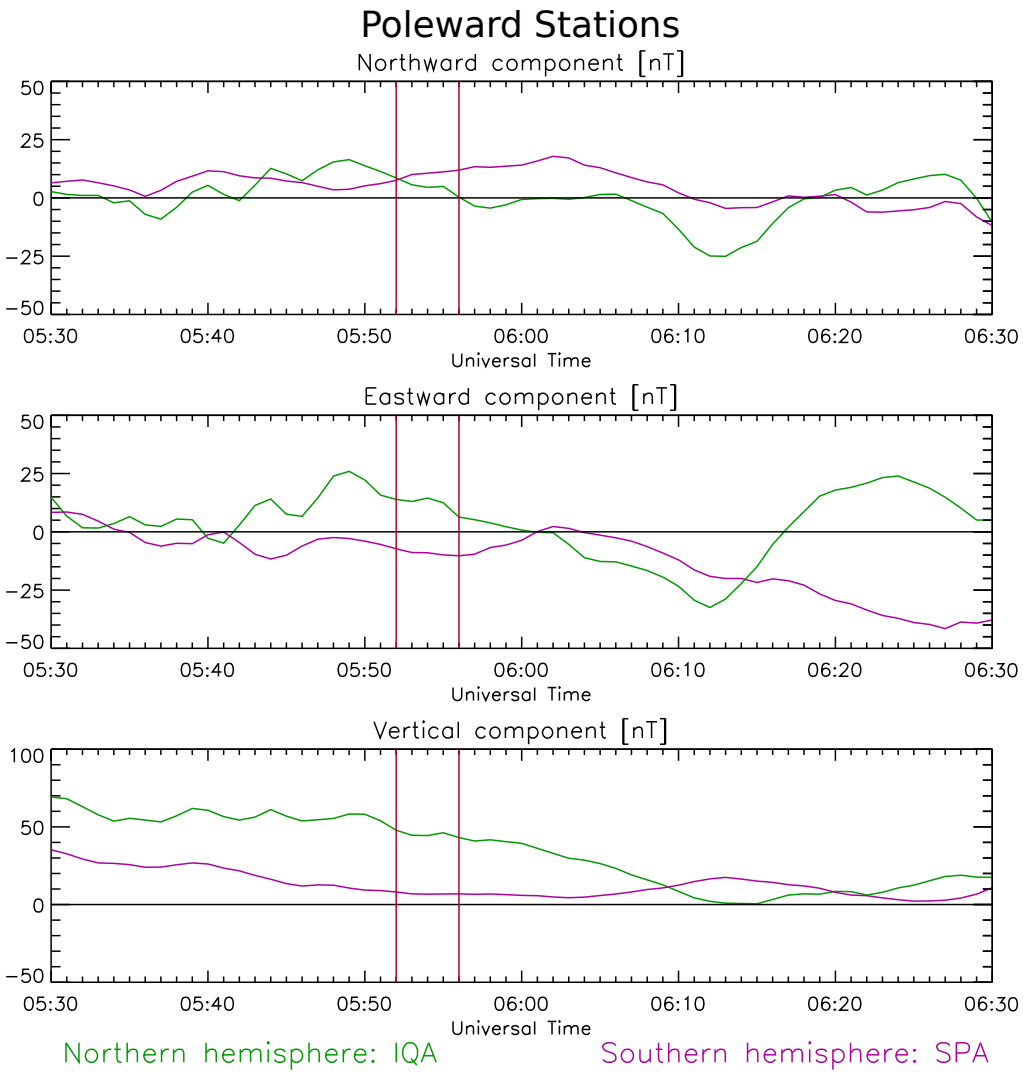

Figure 5.31: Poleward sations IQA and SPA on July 5th 2001. Vertical red lines indicate the interval of the visible non-conjugate aurora. The start time of the feature is uncertain for this event as the FOV of Polar VIS is not sufficient prior to 05:52 UT.

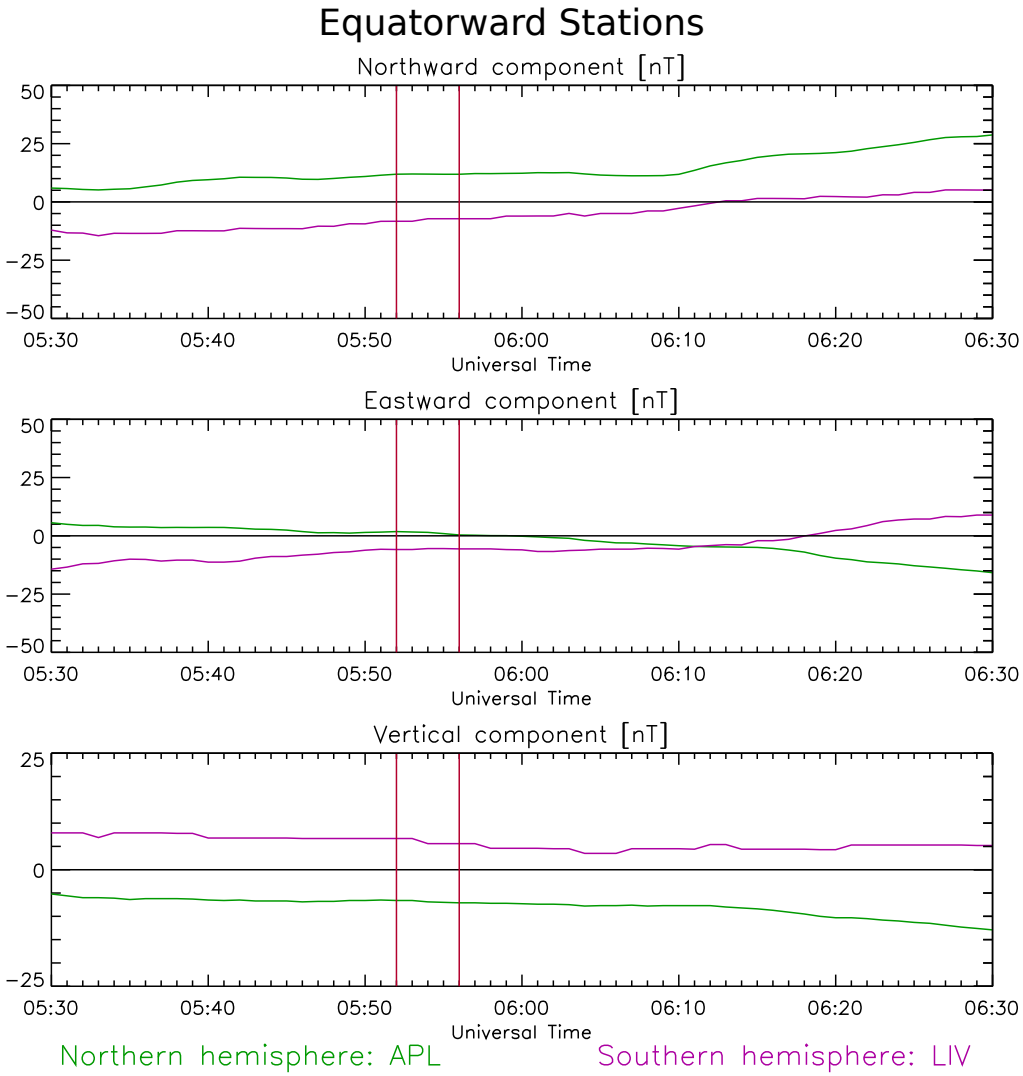

Figure 5.32: Equatorward stations APL and LIV on July 5th 2001. Vertical red lines indicate the time of the first and last conjugate satellite image pair where the non-conjugate aurora is visible. The start time of the feature is uncertain for this event as the FOV of Polar VIS is not sufficient prior to 05:52 UT.

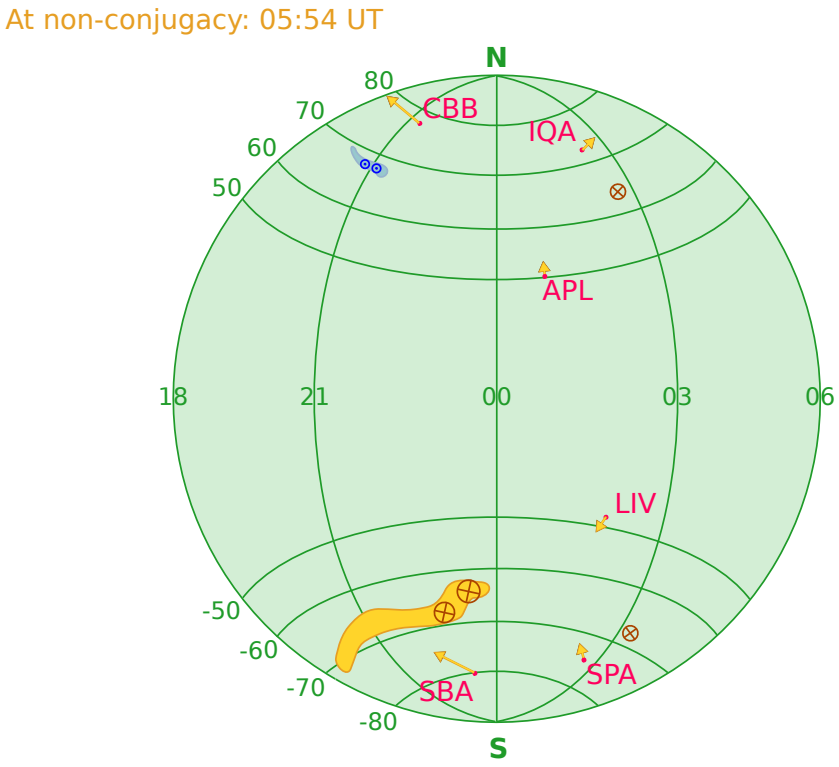

Figure 5.33: Proposed field aligned currents during non-conjugate auroral event at 05:54 UT on July 5th 2001. Upward field aligned currents are indicated in blue, while brown arrows show the proposed downward field aligned currents. The magnetic perturbation measurements are shown in yellow.

observed for the indicated interval of non-conjugate aurora. However, it is probable that the non-conjugate feature existed for a longer period before and after the time span of conjugate image pairs. This leads us to consider the mentioned decrease of 20nT in the eastward component at SBA at 05:43 UT to 06:00 UT as a possible response to the non-conjugate feature in the southern hemisphere. For the same time interval we see an increase in the vertical component at SBA, indicating an intensification of an eastward horizontal current. At CBB, in the northern hemisphere, we do not see a similar response or change in that time interval. The eastward component in the northern hemisphere continues to be stable at -35nT. Nevertheless, the total horizontal direction of the ground magnetic perturbation field at SBA in the southern hemisphere, is not in a direction consistent with the expected perturbation from the proposed field aligned currents in the area of the non-conjugate auroral feature. Nor is the decrease of the eastward component at SBA, mentioned above. A decrease in the eastward component indicates a westward turning of the total horizontal magnetic perturbation field. Considering the arguments presented in Chapter 4.4, we expect an eastward turning at this station, as a response to the observed non-conjugate auroral feature. This apparently contradictory response leads us to consider a downward field aligned current to be associated with the non-conjugate auroral feature. For this event the Defense Meteorological Satellite Program (DMSP) satellite F.13 passes through the non-conjugate auroral feature in the southern hemisphere. The DMSP satellites measure the ion and electron precipitation in the region they pass through. The DMSP F.13 pass through the non-conjugate arc in the southern hemisphere shows that there is a large flux of precipitating protons in this area. This may indicate that the current in this arc is carried mostly by protons and consequently is directed downward. This should be investigated further (see Chapter 8). In Figure 5.33 we propose a downward current, consistent with the measurements at SBA and possibly the DMSP data. For a downward current, the decrease and subsequent increase at SBA, discussed above, is a possible signature of the current associated with the non-conjugate aurora. However, as we can not identify the start time of the non-conjugacy accurately and the DMSP data needs further analysis, we can not conclude confidently about this signature. Additionally, as for the event on July 2nd 2001, the concern regarding the local magnetic variations, possibly affecting the measurements at SBA, should be kept in mind.

5.2 Summary of the observations

In Chapter 5.1 we presented and interpreted four observations of non-conjugate aurora events previously identified by *Laundal and Østgaard* [2009] and *Reistad et al.* [2013] and the associated ground magnetometer measurements. We summarize and categorize our findings in the following. Results are presented in Table 5.1.

In one of the four presented events we were able to find signatures of asymmetric field aligned currents in the two hemispheres related to the non-conjugate aurora. From the observations we find that there are three essential factors that are decisive in finding signatures of field aligned currents directly linked to non-conjugate auroral features.

1. The spatial evolution of the non-conjugate auroral features.
2. The temporal evolution of the non-conjugate auroral features.
3. The position of the conjugate ground magnetometer station pairs in relation to the non-conjugate auroral features.

The magnitude and spatial extent of a current are important as the magnetic perturbation of the current is proportional to this (see Equation 2.10). For an isolated intense auroral feature we are likely to detect signatures of the respective intense field aligned current. Signatures of non-conjugate auroral features and their accompanying field aligned currents are extremely difficult to detect with certainty as we have no means for source separation of the ground magnetometer data. Especially when they are in close vicinity of other auroral features of similar or higher intensity or have a small spatial extent. In our analyses we found that three of the four presented events show isolated intense non-conjugate auroral features. In Table 5.1 we indicate the events that had intense auroral features by an $\times$, in the third column. For one of these, the auroral feature was intense, but had a small spatial extent. This is indicated by the parenthesis. Also, for the same reasons the position of the conjugate ground magnetometer station pairs relative to the observed non-conjugate auroral features is important. We found that three out of the four events presented, had conjugate station pairs at acceptable locations. The second column of Table 5.1 summarizes this.

A distinct temporal evolution of the non-conjugate auroral features is important for the identification of the asymmetric field aligned currents and their signatures. For events with a well defined start and end time of the non-conjugate feature, determined from the satellite images, we examined the ground magnetic perturbation measurements for a simultaneous response. For changes coinciding with the appearance and disappearance of the non-conjugate auroral feature we interpret these as a response to the associated field aligned current. We were able to identify well defined start and end times for three of four of the non-conjugate events presented. These are indicated in the fourth column of Table 5.1. In the last column we indicate if a response associated with the identified non-conjugacy was observed.

Event	Good Station Position	Intense Non-conjugate Aurora	Well defined interval Non-conjugate Aurora	Visible Magnetic Signature
May 12th 2001	×	×	×	×
November 3rd 2002	×	(×)	×	(×)
July 2nd 2001	×	-	×	-
July 5th 2001	-	×	-	-

Table 5.1: Events are categorized in terms of the position of the ground magnetometer station used and the spatial extent and intensity of the non-conjugate auroral features. In the last column we indicate if a response associated with the identified non-conjugacy was observed. For the event of November 3rd the magnetic signatures were inconclusive, indicated by the (×).

6 Discussion

In the following chapter we discuss the general outcome of our observations. This is followed by a discussion of the method. Last we briefly comment on the limitations of the method.

6.1 Discussion of the findings

Our goal for this thesis was to investigate the field aligned currents in both hemispheres, associated with non-conjugate aurora. Our observations, presented in Chapter 5, suggest that we can measure signatures of the the field aligned currents in the ground magnetic perturbation field if certain conditions are met. Such conditions occurred for one out of four events analyzed, and we identified signatures of field aligned currents that appeared to be asymmetric in the two hemispheres, using the method developed in Chapter 4. On May 12th 2001, which has been the focus of several studies [*Laundal and Østgaard*, 2009; *Laundal et al.*, 2010], we observed that the evolution of the ground magnetic perturbation field in the equatorward region of the two hemispheres was different. This was interpreted as a signature of an asymmetric field aligned current associated with the transient non-conjugate auroral feature in the morning sector of the northern hemisphere. The absence of a signature from a current in the southern hemisphere, associated with the non-conjugate feature in the northern hemisphere, further supports this. Similar observations were made on November 3rd 2002 where the evolution of the ground magnetic perturbation field was slightly different for the two hemispheres. The signature is in accordance with a field aligned current present in the northern hemisphere where a small, intense non-conjugate auroral feature is observed. This current is absent in the southern hemisphere. However these signatures were small, and we could not make confident conclusions for this event.

In Table 5.1 we summarized our findings from the observations and listed the factors we found to be significant for identifying asymmetric field aligned currents. By

comparing the data sets for the four events presented we found that the presence of a signature from asymmetric field aligned currents at the conjugate ground magnetometer stations depends on the position of the conjugate station pairs, the intensity and the temporal evolution of the associated non-conjugate auroral feature. This is based on the assumption that the spatiotemporal behavior of the non-conjugate auroral feature is dependent on the associated field aligned current as suggested by *Østgaard and Laundal* [2012] based on a number of previous studies. The ground magnetometer data show measurements of all perturbations to the Earth's magnetic field at its position related to external sources (see Chapter 3.2). As we have no means to separate these sources, the interpretation is complex [*Kelley*, 2009]. The more intense a given field aligned current is, causing a proportionally intense non-conjugate feature, the larger and more clear we expect the magnetic perturbation measured in the vicinity of it to be. The magnitude of the magnetic perturbation also depends on the relative distance of the measurement to the source current. This is a direct result of *Biot-Savart's law* (Equation 2.10) and consequently, we found the position of the ground magnetometer station to be of great importance. Actually, the lack of adequate stations is the reason for the exclusion of the remaining non-conjugate events identified by *Reistad et al.* [2013]. However, we can not make confident conclusions about any critical distance region at which a signature fades, as we do not know the magnitude of the field aligned currents causing the non-conjugate features and the lack of means to identify any source current uniquely.

For the two events on the 2nd and 5th of July 2001 we found no signatures of asymmetric field aligned currents. In our analyses of the data set for each of these events we found the major difference compared with the other events, to be the three factors mentioned above. Because only four of the ten identified non-conjugate auroral events from *Reistad et al.* [2013] had sufficient ground magnetometer data available, our data set is limited. In order to conclude more confidently on the crucial factors for the identification of field aligned currents associated to the non-conjugate aurora, a larger data set is needed.

6.2 Discussion of the method

The method for analyzing our data is described in Chapter 4. A substantial part of the data processing we do before interpreting the data, consists of a transformation between coordinate systems. We convert magnetic perturbation measurements from the local magnetic coordinate system used by SuperMAG [*Gjerloev*, 2009] to geographic coordinates and subsequently to AACGM coordinates [*Baker and Wing*, 1989] using the approach suggested by *Richmond* [1995]. The method we used (Chapter 4.2) is similar to the method described by *Laundal and Gjerloev* [2014] as it was developed simultaneously and in cooperation with one of the authors.

We argue that the transformation is essential as the comparison of two data sets should be in a common reference system. Omitting this step could lead to different and likely erroneous interpretations and conclusions, as the difference between the coordinate systems is variable and large at the position of some ground magnetometer stations, especially close to the magnetic pole in the southern hemisphere (see

Figures 4.3 and 4.10). The ionospheric electrodynamics are altitude dependent and highly organized by the Earth's magnetic field. Using a reference frame based on a realistic magnetic field model such as Apex and AACGM will therefore better represent the SuperMAG measurements, originally given in an orthogonal frame defined locally at ground level. Unfortunately, the IGRF model we use in the transformation, does not include sources of local variations of less than $\sim$ 3000 km extent, which can be significant at some of the SuperMAG ground magnetometer stations. As mentioned in Chapter 5.1.3.2 and 5.1.4.2, we have strong indication that the local magnetic variations are indeed a significant contribution at SBA (Scott Base, Antarctica) in the southern hemisphere. However, we did not observe any signatures of asymmetric field aligned currents for the two events where measurements from SBA were used. Ideally, information of the small scale local magnetic field at the position of the magnetometer, if such were available, should be included in the calculations and analysis.

Our analyses of the non-conjugate auroral events is based on the events identified by *Reistad et al.* [2013]. We outline their method in Chapter 4.3. The process for the identification of non-conjugate features is challenging as a result of the difference in camera sensitivity of WIC and VIS (see Chapter 3.3.3). A general intensity relation between the two cameras is established from an intensity profile at a reference magnetic latitude, and used to scale the images obtained by VIS Earth so that the color should reflect an approximate equal brightness in the WIC image. Although the method developed by *Reistad et al.* [2013] is fairly robust, a slight change in the scaling factor can lead to a significant change in the appearance of the aurora in the conjugate image pairs. To avoid misinterpretation, *Reistad et al.* [2013] performs an MLT-slice test, validating the suspected non-conjugate auroral features by demanding an intensity difference of a factor 2 in conjugate regions. We apply the identical intensity relation as suggested by *Reistad et al.* [2013] to images in a time interval, centered at the time of the conjugate image pair in which the non-conjugate auroral feature first was identified. Subsequently, we identify the interval where the non-conjugate auroral feature is visible in these images, by visual inspection. This method for determining the duration of the non-conjugate feature is crude and a possible source of error. Ideally, a slice-test identical to the one performed by *Reistad et al.* [2013], should be carried out for each of the conjugate images pairs, to identify the duration of the non-conjugate feature. Because we try to identify signatures of current systems directly related to the non-conjugate auroral features, we search for responses simultaneous to the appearance and disappearance of these. A misinterpretation in the identification of the start and end time of the non-conjugate auroral features, could lead to an erroneous analysis of the magnetic perturbation measurements related to the auroral feature. However, in the present thesis we have used the identified start and end times in an indicative manner, rather than a strict requirement, when looking for simultaneous signatures in the magnetic perturbation measurements. Thus, the presented results are not thought to change significantly for a small change in the time interval of the non-conjugate feature.

6.3 Limitations

To perform the analyses of the non-conjugate auroral events in Chapter 5, multiple assumption were made regarding the coordinate systems, conjugate footpoints of the magnetic field lines and their geometry. Some of the limitations induced by these will be discussed here as well as potential sources of error.

In Chapter 4 we described in detail the method developed for the analyses of the data. The assumptions made in relation to the coordinate transformation are stated in Chapter 4.2.6 in accordance with *Gjerloev* [2012], and we assumed the N-coordinate of the SuperMAG coordinate system to be along the IGRF model. As briefly mentioned in Chapter 5.1.4.2, we found the measurements at SBA in the southern hemisphere to be inconsistent with any reasonable current system during the event of July 5th 2001. We mentioned the effects of local magnetic variation for the SBA station in Chapter 5.1.4.2 In Chapter 6.2 explain that the local magnetic variations are not taken into account in the IGRF model. *Laundal and Gjerloev* [2014] compared the declination computed by SuperMAG and IGRF and used it as an indicator of the local variations. This concern is not unique regarding to the SBA station and further examples are known, where this is a significant effect [e.g. Kiruna, Sweden *Laundal and Gjerloev*, 2014].

Further, in our analysis and interpretation of the data we used the ΔMLT value calculated by *Reistad et al.* [2013] to compensate for the displacement of conjugate points in the two hemispheres. We shifted the northern hemisphere such that footpoints of conjugate field lines aligned, and by this we determined conjugate ground magnetometer station pairs and compared the measurements from these. The same value for ΔMLT is used for the entire interval of an event and regardless of the position of the non-conjugate auroral feature. The shift varies with local time [*Cowley et al.*, 1991] and *Reistad et al.* [2013] limited the calculation of the ΔMLT to the nightside region of the oval within 20-04 MLT. The events on May 12th 2001 and July 5th 2001 presented here, show non-conjugate auroral features in areas just at the border of this limitation. Also, *Laundal et al.* [2010] found that for the event on May 12th 2001 the interhemispheric differences in the polar cap location and size may change rapidly during the substorm expansion phase, confirming that processes linked to the asymmetric and non-conjugate aurora are very dynamic. However, a change in the ΔMLT during the interval of the non-conjugate auroral event is not likely to alter our interpretation of the current systems significantly. As the number of available ground magnetometer stations in the preferred regions relative to the non-conjugate aurora is limited, we would likely, depending on the magnitude of the change of ΔMLT choose the same conjugate magnetometer station pairs.

We made the assumption of negligible contributions from the ring current for ground magnetic measurements from latitude regions of the auroral oval and higher in Chapter 2.2.5. In the event of May 12th 2001, we proposed that the equatorward measurements were strongly affected by contributions from the ring current as the position of the station is at low magnetic latitudes (below $\pm 50^\circ$). For all presented events the equatorward boundary of the auroral oval was around $\pm 60^\circ$ or higher. We assume no contribution from the ring current to the ground magnetic perturbation measure-

ments in this region. All stations determined to be in the equatorward region for the events are at latitudes above $\pm 50^{\circ}$ but below $\pm 60^{\circ}$. The latitude at which the effects from the ring current becomes truly negligible is uncertain, making the interpretation of the extent of the impact from the ring current on the measurements, difficult at these station. The *Sym-H* index gives an indication of the intensity of the ring current.

The non-conjugate events that form the base of this Thesis, are identified by *Reistad et al.* [2013]. The identification of these is challenging, as a result of the difference in camera sensitivity.

7 Summary and Conclusions

Our main goal with the present thesis was twofold. First, we wanted to develop a solid method for identifying the field aligned currents related to the specific non-conjugate auroral features identified by *Reistad et al.* [2013] and *Laundal et al.* [2010]. Secondly, by utilizing this method we intended to explore the idea that the non-conjugate aurora can be explained by asymmetries in the field aligned current system in the two hemispheres [*Østgaard and Laundal*, 2012].

7.1 Key Results

Based on the methods of numerous previous studies [e.g. *Nakano*, 2005], we expanded and developed a method to identify field aligned currents associated with identified non-conjugate auroral events. We transformed the ground magnetometer measurements to AACGM coordinates and combined them with conjugate satellite images from Polar VIS Earth and IMAGE WIC. Using ΔMLT, the shift of the conjugate footpoints of magnetic field lines, calculated by *Reistad et al.* [2013], we found conjugate ground magnetometer station pairs in a geomagnetic coordinate system. We proposed expected ground magnetic perturbation field directions from the field aligned currents assumed to cause the non-conjugate auroral features, using *Biot-Savart's* law. We compared them to our measurements and utilized these to postulate a current system. For one out of four events presented we were able to identify signatures of asymmetric field aligned currents. Three factors stood out, that we found to be important for the identification of these currents. The position of the ground magnetometer station in relation to the non-conjugate auroral feature, the spatial extent of the feature and its intensity compared to surrounding auroral features. We summarize that our developed method and our findings are an indication that the field aligned currents causing non-conjugate aurora can be identified and are asymmetric.

7.2 This thesis in a larger context

Several studies have been concerned with the identification of non-conjugate aurora in terms of location and intensity, and understanding the processes and dynamics involved [e.g. *Laundal and Østgaard*, 2009; *Laundal et al.*, 2010; *Østgaard et al.*, 2007; *Reistad et al.*, 2013]. The present thesis aims to contribute to this effort. Based on conjugate satellite imaging by IMAGE WIC and Polar VIS Earth, *Østgaard and Laundal* [2012] suggested that the observed non-conjugate aurorae can be explained in terms of asymmetric currents in the two hemispheres. We explore this possibility by utilizing and expanding well established methods for studying the field aligned currents in the ionosphere with ground based magnetometers [e.g. *Friis-Christensen et al.*, 1985; *Iyemori*, 1990; *Kamide et al.*, 1981; *Nakano*, 2005]. Combining the ground magnetic perturbation data with conjugate satellite images of identified non-conjugate auroral events [*Laundal and Østgaard*, 2009; *Reistad et al.*, 2013], we were able to identify signatures of field aligned currents related to the non-conjugate aurora in two out of four suitable events, supporting the suggestions of *Østgaard and Laundal* [2012]. Identifying and quantifying the non-conjugate aurora and the asymmetric field aligned currents can advance our understanding of the processes that lead to the interhemispheric asymmetries in the aurora and current systems and thereby the coupling of the ionosphere to the magnetosphere and space for the two hemispheres.

8 Future Work

In this thesis we identify ground magnetic perturbations field that we relate to asymmetric field aligned currents associated with the observed non-conjugate aurora in one out of four non-conjugate events. Few non-conjugate auroral events are published in the conjugate images from Polar VIS Earth and IMAGE WIC at the present time. Only four of these had adequate ground magnetometer stations available during the event. Thus, besides aspiring to motivate the identification of further non-conjugate auroral events, we present our suggestion for future work in this chapter.

8.1 Suggestions for improvement

Based on the experience gathered throughout this Thesis and the discussion in Chapter 6, we suggest improvements that could clarify and expand the present work in the following section.

- Perform an MLT slice-test, as done by *Reistad et al.* [2013], to verify the beginning and end time of the non-conjugate auroral feature with greater confidence.
- Calculate ΔMLT more frequently, using the method described by *Reistad et al.* [2013], to validate the conjugacy of the station pairs in the northern and southern hemisphere during the whole time interval of the non-conjugate aurora.
- Calculate and compare the deviation of the declination, D, derived by SuperMAG and the IGRF model, to give an indication of the local magnetic anomalies that might affect some magnetometer stations [as done by *Laundal and Gjerloev*, 2014].
- Calculate the power difference of the measured asymmetric field aligned currents. Use Biot-Svart's law and estimating the extent of the asymmetric field aligned current producing the non-conjugate auroral features, to quantify the asymmetries observed between the two hemispheres.

8.2 Comparison to ground magnetic perturbation from conjugate auroral events

We have developed a method for identifying asymmetric current systems in association with observed non-conjugate aurora in conjugate regions of the two hemispheres. Applying the same method to conjugate auroral events should yield symmetric current systems and symmetric ground magnetic field perturbations in conjugate regions. A comparison of ground magnetic perturbations of conjugate auroral events to the events presented in this thesis would give further insight to the topic of asymmetric currents causing non-conjugate aurora. We suggest to carefully select conjugate events at similar general geomagnetic activity and seasons as the presented non-conjugate events, to minimize differences induced by effects from other sources than the aurora. As the number of observed conjugate auroral events is much larger, it is likely possible to find events with several ground magnetometer station in conjugate regions of the two hemispheres.

Such an analysis and comparison could, depending on the result, strengthen or weaken the hypothesis of asymmetric field aligned currents causing non-conjugate aurora as well as give further indication to if the developed method is adequate for the study of these.

8.3 Inclusion of additional data sets

The proposal of the field aligned currents in the presented events based on SuperMAG data only is crude. It would be useful to use additional data to verify the field aligned currents. Satellite data with passes over the area of the proposed currents would greatly improve the confidence of the proposed field aligned current areas. One such satellite data set is the Defense Meteorological Satellite Program (DMSP) data. The DMSP satellites are run by the United States Air Force Space and Missile Systems Center part of Department of Defense program and National Aeronautics and Space Administration (NASA). They follow a near-polar orbit at an altitude of 830km. A Precipitating Electron and Ion Spectrometer on board the satellites could provide information about particle fluxes and magnetic coordinates of the area in which the particles are absorbed in the aurora oval [*NOAA*, 2015]. However, to use this data the satellite must pass over the auroral features we wish to investigate. For the events presented in this thesis we were able to find one suitable satellite pass through the non-conjugate auroral feature on July 5th 2001. The data of the ion and electron precipitation from the DMSP F.13 should be investigates further for this event. The probability of finding a well suited non-conjugate auroral event, well positioned conjugate SuperMAG station pairs in both hemispheres and DMSP data for the same time interval is low. However, not impossible as there are four DMSP satellites and future analyses of asymmetric field aligned currents related to non-conjugate aurora should investigate the availability of DMSP data. For non-conjugate auroral events after January 2010, it is possible to use Active Magnetosphere and Planetary Electrodynamics Response Experiment (AMPERE) data derived from measurements done by the Iridium satellites. The magnetic field measurements provided by AMPERE can be used to determine areas in which field aligned currents flow [*Kramer*, 2002]. In combination with the method developed

in this thesis, further insight on the small scale field aligned currents related to the non-conjugate aurora could be gained from additional satellite data.

Appendices

A SuperMAG station information

In Table A.1 we list all SuperMAG stations used in this Thesis and their respective geographic latitude and longitude, magnetic latitude and longitude, and both components of the $\mathbf{f_1}$ and $\mathbf{f_2}$ vectors calculated (see Chapter 4.2.6). For SPA station in the southern hemisphere we indicate the geographic latitude and longitude used to calculate $\mathbf{f_1}$ and $\mathbf{f_2}$ in brackets. This is done to avoid a numerical error in the calculations.

Northern Hemisphere								
IAGA, station name	**Glon**	**Glat**	**Mlon**	**Mlat**	**f_1 (east)**	**f_1 (north)**	**f_2 (east)**	**f_2 (north)**
APL, Applied Physics Lab	283.12	39.17	-1.34	49.98	0.974346	-0.0959919	-0.0681253	-1.17694
ARC, Arctic Village	214.43	68.13	-96.81	68.94	0.983558	0.502892	0.360880	-0.804692
ATU, Attu	306.43	67.93	38.76	74.47	0.952811	-0.483839	-0.255063	-0.895821
BFE, Brorfelde	11.67	55.62	89.54	52.14	1.09869	-0.0915707	-0.230514	-0.890920
BOR, Borok	38.33	58.03	113.25	53.94	1.01923	-0.0265857	-0.163906	-0.991257
BRW, Barrow	203.25	71.30	-108.95	70.25	0.994469	0.479704	0.406841	-0.767250v
CBB, Cambridge Bay	255.00	69.10	-51.61	77.22	0.884070	0.432730	0.269274	-0.986765
CLF, Chambon la foret	2.27	48.02	79.35	44.12	1.27640	-0.0819264	-0.207793	-0.877888
CMO, College	212.14	64.87	-96.03	65.29	1.00954	0.453956	0.317371	-0.828863
CY0, Clyde River	291.40	70.50	18.56	79.18	0.908026	-0.367497	-0.174513	-1.00213
DIK, Dixon	80.57	73.55	156.09	68.71	0.902457	-0.0606204	-0.118788	-1.10049
DMH, Danmarkshavn	341.37	76.77	86.17	77.30	0.905776	-0.578351	-0.575633	-0.660395
FRN, Fresno	240.30	37.10	-56.46	43.02	1.02270	0.257802	0.205357	-0.979171
FUR, Furstenfeldbruk	11.28	48.17	86.91	44.01	1.22318	-0.0271692	-0.194189	-0.916953
GTF, Grafton	288.05	43.62	6.12	53.70	0.974041	-0.181415	-0.0790235	-1.14898
HLP, Hel	18.82	54.61	95.19	50.79	1.08444	-0.0546706	-0.207296	-0.924852
IRT, Irkoutsk	104.45	52.17	177.24	47.40	1.02916	-0.0543614	-0.0104870	-1.12065
NAL, New Aalesund	11.95	78.92	111.27	76.25	0.909819	-0.405329	-0.591227	-0.760371
NAN, Nain	298.30	56.40	22.44	64.57	0.985580	-0.337889	-0.122500	-1.02535
NRD, Nord	343.33	81.60	104.81	81.11	0.691615	-0.740525	-0.813663	-0.468029
PBK, Pebek	170.90	70.10	-130.45	65.49	1.06149	0.200260	0.327515	-0.848945
PGC, Pangnirtung	294.20	66.10	20.27	74.74	0.938392	-0.356081	-0.150080	-1.00885
PTK, St Paratunka	158.25	52.94	-133.34	46.34	1.05303	0.0337994	0.102263	-0.911219
RES, Resolute Bay	265.11	74.69	-41.38	83.29	0.834440	0.403345	0.295145	-1.00314
SIT, Sitka	224.67	57.07	-79.93	59.93	1.00692	0.409188	0.261362	-0.908104
STJ, St Johns	307.32	47.60	31.24	53.68	1.03109	-0.377740	-0.123239	-0.991896
STF, Kangerlussuaq	309.28	67.02	41.46	73.06	0.967155	-0.482072	-0.256528	-0.883186
THY, Tihany	17.54	46.90	92.02	42.49	1.20552	0.0111101	-0.172517	-0.950268
TIK, Tixie	129.00	71.58	-162.65	66.04	0.976883	-0.0322318	0.184242	-1.04352
VIC, Victoria	236.58	48.52	-63.97	53.83	1.01549	0.333902	0.219354	-0.971767
VIZ, Vieze Island	76.98	79.48	156.02	74.02	0.870069	-0.110319	-0.191327	-1.08026

Southern Hemisphere								
IAGA, station name	**Glon**	**Glat**	**Mlon**	**Mlat**	**f_1 (east)**	**f_1 (north)**	**f_2 (east)**	**f_2 (north)**
AMS, Martin de Vivias	77.57	-37.80	138.67	-49.11	0.963912	-0.143001	-0.368744	-0.938023
B02, m66-294	294.00	-66.03	8.37	-50.79	0.967498	-0.0110793	0.155738	-0.837897
B11, m78-337	336.58	-77.51	30.06	-63.22	0.811475	-0.349577	-0.186471	-0.901915
B12, m79-336	335.88	-79.08	29.08	-64.46	0.832227	-0.346737	-0.201442	-0.902346
B21, m87-028	28.41	-87.00	29.01	-73.32	0.315862	-0.925689	-0.896450	-0.333082
CNB, Canberra	149.36	-35.32	-133.21	-45.20	1.08408	0.166148	0.185344	-1.01015
CSY, Casey	110.53	-66.28	156.79	-80.74	0.894789	-0.395447	-0.484887	-0.948112
CZT, Port Alfred	51.87	-46.43	106.16	-53.05	0.763867	-0.191280	-0.467049	-0.811800
DRV, Dumont Durville	140.01	-66.67	-124.41	-80.47	0.976196	0.469264	0.431671	-0.901770
EYR, Eyrewell	172.40	-43.40	-103.64	-50.00	1.04723	0.287381	0.342497	-0.967608
GNA, Gnangara	116.00	-31.80	-173.01	-44.14	1.12533	0.0412046	-0.0720065	-1.00330
HER, Hermanus	19.23	-34.43	82.55	-42.07	0.643397	-0.0809354	-0.350597	-0.932374
LIV, Livingston Island	299.61	-62.66	10.70	-47.77	0.942550	-0.100829	0.126206	-0.823039
MAW, Mawson	62.88	-67.61	90.15	-70.05	0.589532	-0.621523	-0.680533	-0.667112
MCQ, Macquarie Island	158.95	-54.50	-111.91	-64.48	1.03731	0.358389	0.387874	-0.951757
PAF, Port aux Francias	70.26	-49.35	122.10	-58.49	0.840391	-0.278859	-0.473962	-0.869421
SBA, Scott Base	166.78	-77.85	-33.34	-79.91	0.0148013	0.996427	1.05816	-0.00795248
SPA, South Pole Station	0.00(72)	-90.00(-89.7)	19.01	-74.08	-0.49483490	-0.86056149	-0.83973360	0.48503458

Table A.1: Table of all utilized SuperMAG station in the northern and southern hemisphere, showing geographic latitude and longitude, magnetic latitude and longitude, and both components of $\mathbf{f_1}$ and $\mathbf{f_2}$.

B Supplementary plots

B.1 Supplementary plot for May 12th 2001

Figure B.1 is plot of the measured magnetic perturbation rotated by 90° clockwise to indicate the equivalent current direction. All available SuperMAG stations above 40° magnetic latitude in the northern hemisphere are utilized. The plot is included here to support our proposal of a two wedge current system on May 12th 2001 in accordance to the model suggested by *Gjerloev and Hoffman* [2014]. The key features of the two wedge current model are: A poleward shift of the westward electrojet connecting the post- and premidnight components,a polar cap vortex on the poleward edge of the westward electrojet with a center around 74° magnetic latitude, and differing magnitudes in the post- and premidnight sectors of the westward electrojet. In Figure B.1 we plot the equivalent current direction instead of the magnetic perturbation (as in the rest of the Thesis) for easier identification of these key features. Centered at approximately 21 MLT and 75°, a swirl-shape is apparent, consistent with the second key feature of *Gjerloev and Hoffman* [2014]. A poleward shift of the westward electrojet is also visible in the region it is observed (from approximately 23 to 01 MLT). A difference in magnitude of the post- and premidnight westward electrojet is not clearly identifiable. As two out of three key features are visible, we propose the double current wedge current system as a possible solution to the current system during the non-conjugate auroral event on May 12th 2001.

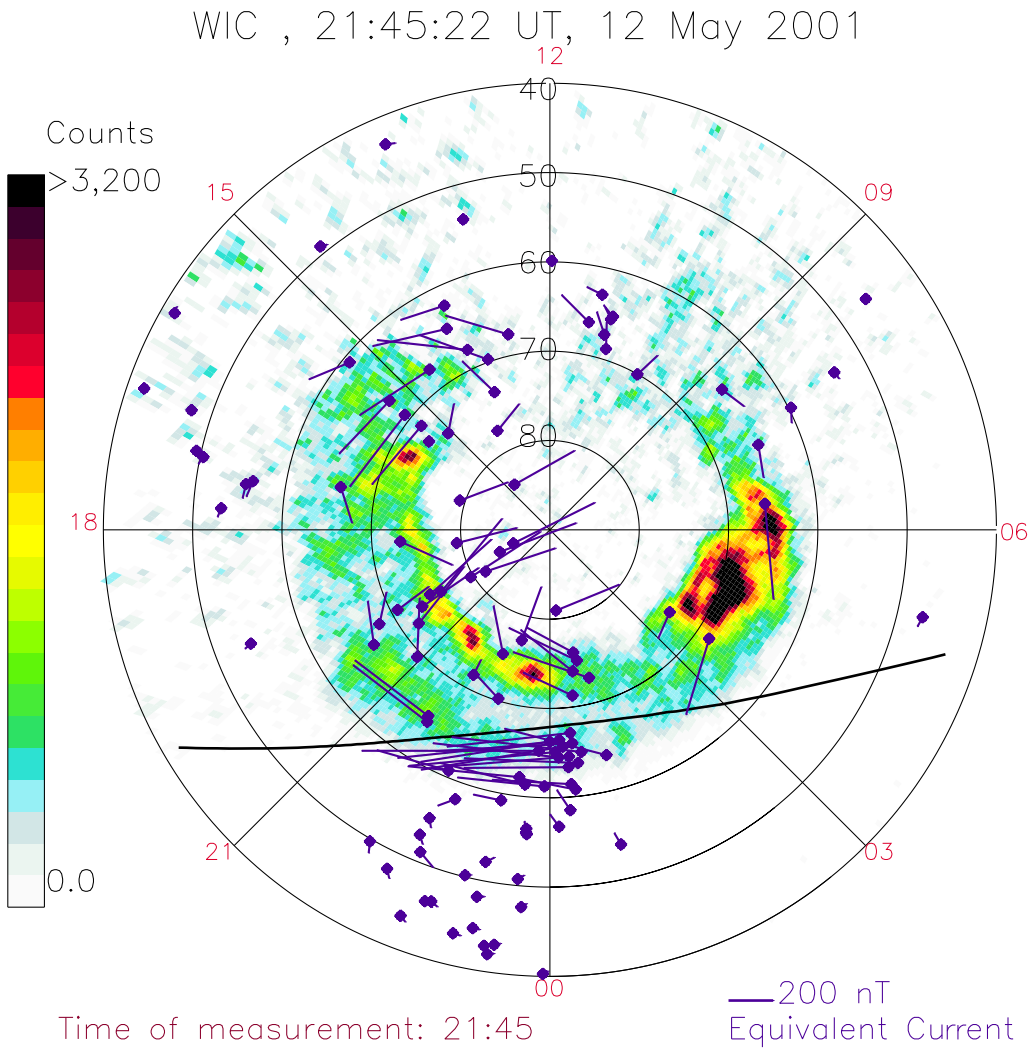

Figure B.1: Magnetic perturbation rotated clockwise by 90 ° indicating the direction of equivalent currents at all available SuperMAG stations in the northern hemisphere on May 12th 2001.

B.2 Supplementary plot for November 3rd 2002

Figure B.2 shows a plot of the magnetic perturbation at all available SuperMAG station in the northern hemisphere on November 3rd 2002. We indicate the ground magnetometer stations on the west Greenland coast by a pink dashed circle. In Chapter 5.1.2.2 we postulate downward field aligned currents in the area eats of the indicated stations around the same latitude region. The plot in Figure B.2 shows that the ground magnetic perturbation field at the west Greenland coast stations is consistent with these currents.

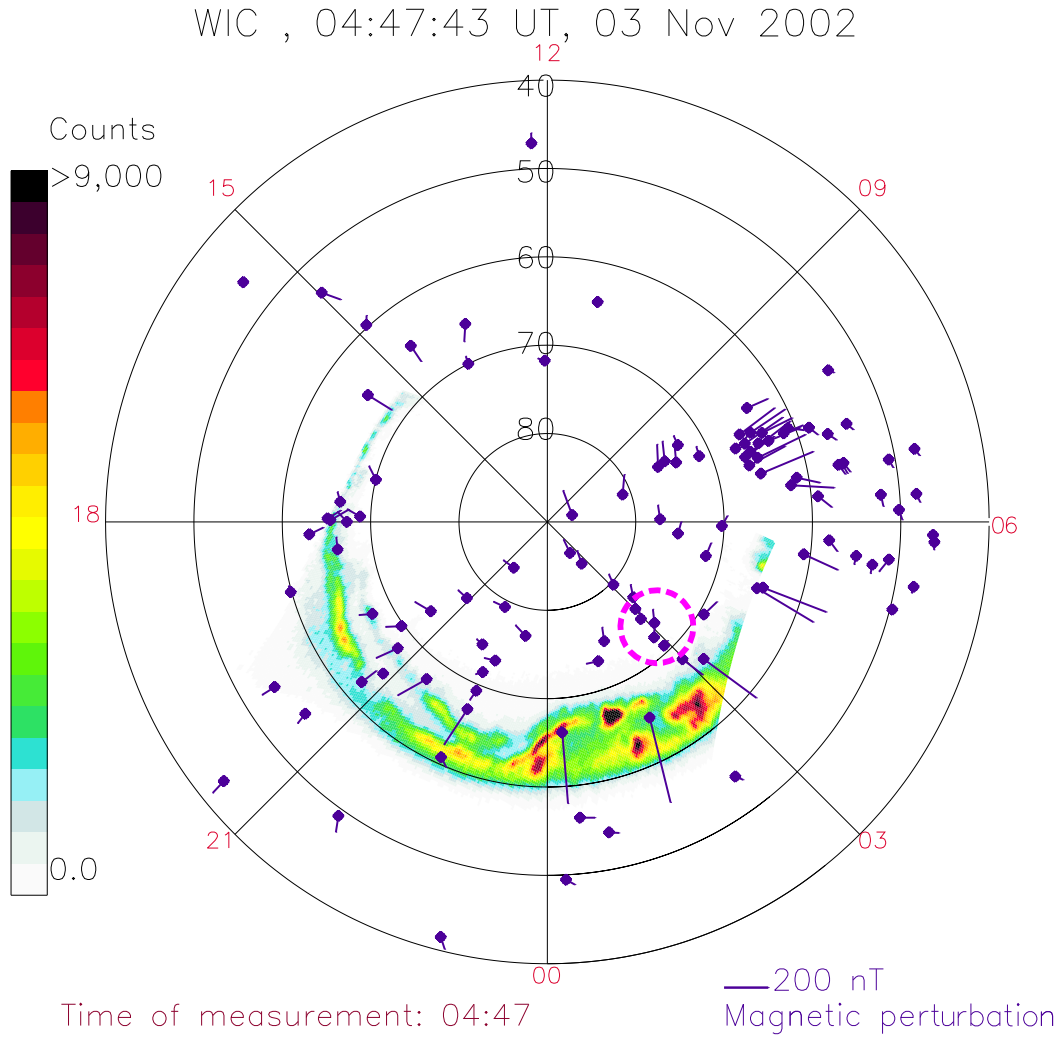

Figure B.2: Magnetic perturbation at all available SuperMAG stations in the northern hemisphere on November 3rd 2002.

C List of Abbreviations

AACGM	Altitude Adjusted Corrected Geomagnetic Coordinates
ACE	Advanced Composition Explorer
AE	Kyoto Auroral Electojet index
AL	Kyoto Wesward Electrojet index
AU	Kyoto Eastward Electrojet index
AMPERE	Active Magnetosphere and Planetary Electrodynamics Response Experiment
$\mathbf{B_x}$	IMF x-component [nT]
$\mathbf{B_y}$	IMF y-component [nT]
$\mathbf{B_z}$	IMF z-component [nT]
DCW	Double Current Wedge
DE1	Dynamic Explorer 1
DMSP	Defense Meteorological Satellite Program
Dst	Disturbed Storm Time index
DZA	Satellite Zenith Angle
FAC	Field Aligned Current
FOV	Field Of View
FUV	Far Ultraviolet
IAGA	International Association of Geomagnetism and Aeronomy

IGRF	International Geomagnetic Reference Field
IMAGE	Imager for Magnetopause to Auroral Global Exploration
IMF	Interplanetary Magnetic Field
$\lambda_{\mathbf{tilt}}$	Tilt angle of dipole axis with respect to the rotational axis of the Earth
LBH	Lyman-Birge-Hopfield
MHD	Magnetohydrodynamics
MLT	Magnetic Local Time
NASA	National Aeronautics and Space Administration
nT	nano Tesla
OMNI	NASA data product
QDC	Quiet Day Curve
$\mathbf{R_E}$	Earth radii (≈ 6731km)
RIP	Radio Plasma Imager
SCW	Substorm Current Wedge
SuperMAG	Global Ground-Based Magnetometer Initiative
SW	Solar Wind
SZA	Solar Zenith Angle
TDI	Time Delay Integration
UT	Universal Time
UV	Ultraviolet
VIS	Visible Imaging System
WIC	Wideband Imaging Camera

Bibliography

Acuña, M. H., K. W. Ogilvie, D. N. Baker, S. A. Curtis, D. H. Fairfield, and W. H. Mish (1995), The global geospace science program and its investigation, *Space Science Reviews*, *71*, 5–21.

Adams, R. D., and D. A. Christoffel (1962), Total Magnetic Field Surveys between New Zealand and the Ross Sea, *Journal of Geophysical Research*, *67*(2), 805–814.

Ahn, B., B. A. Emery, H. W. Kroehl, and Y. Kamide (1999), Climatological characteristics of the auroral ionosphere in terms of electric field and ionospheric conductance, *Journal of Geophysical Research*, *104*(A5).

Ajello, J., and D. Shemansky (1985), A reexamination of important N2 cross sections by electron impact with application to the dayglow: The Lyman Birge Hopfield Band System and NI (119.99 nm), *Journal of Geophysical Research Space Physics*, *90*(NA10), 9845–9861, doi:10.1029/JA090iA10p09845.

Akasofu, S. (1983), The magnetospheric currents: An introduction, *Geophysical Monograph*, *28*, 29.

Akasofu, S., and C. Meng (1969), A study of polar magnetic substorms, *Journal of Geophysical Research*, *74*(1), 293–313.

Akasofu, S.-I. (1964), The development of the auroral substorm, *Planetary Space Science*, *12*, 273–282.

Babcock, H. W. (1961), The topology of the Sun's magnetic field and the 22-year cycle, *Astrophysical Journal*, *133*, 572, doi:10.1086/147060.

Baker, K. B., and S. Wing (1989), A new magnetic coordinate system for conjugate studies at high latitudes, *Journal of Geophysical Research*, *94*(A7), 9139, doi:10.1029/JA094iA07p09139.

Barnes, R. (2013), ampere.jhuapl.edu/code/idl_aacgm.html, *IDL AACGM DLM*.

Baumjohann, W., and R. Treumann (2012), *Basic Space Plasma Physics*, revised ed ed., IMperial Colleg Press, London.

Birkeland, K. (1908), *The Norwegian Aurora Polaris Expedition 1902-1903*, H. Aschelhoug & Co.

Biskamp, D. (2000), *Magnetic Reconnection in Plasmas*, Cambridge University Press.

Brekke, A. (2013), *Physics of the upper Polar Atmosphere*, second edi ed., Springer, Tromsø.

Burch, J. L. (2000), Image mission overview, *Space Science Reviews*, *91*, 1–14.

Chapman, S. S. (1935), 4tmospheric Electricity, *Terrestial Magnetism and Atmospheric Electricity*, *40*(4), 349–370.

Clauer, C. R., and R. L. McPherron (1974), Mapping the local time-universal time development of magnetospheric substorms using mid-latitude magnetic observations, *Journal of Geophysical Research*, *79*(19), 2811–2820, doi:10.1029/JA079i019p02811.

Cowley, S. W. H. (1981), Asymmetry effects associated with the x-component of the IMF in a magnetically open magnetosphere, *Planetary Space Science*, *29*(8), 809–818.

Cowley, S. W. H., J. P. Morelli, and M. Lockwood (1991), Dependence of convective flows and particle precipitation in the high-latitude dayside ionosphere on the X and Y components of the interplanetary magnetic field, *Journal of Geophysical Research*, *96*(A4), 5557–5564.

Craven, J., J. Murphree, L. A. Frank, and L. Cogger (1991), Simultaneous optical observations of transpolar arcs in the two polar caps, *Geophysical Research Letters*, *18*(12), 2297–2300.

Cullington, a. L. (1968), The magnetic secular variation at Scott Base and Hallett Station, *New Zealand Journal of Geology and Geophysics*, *11*(4), 982–986, doi:10.1080/00288306.1968.10420764.

Davis, N., and M. Sugiura (1966), Auroral Electrojet Activity Index AE and its Universal Time variations, *Journal of Geophysical Research*, *71*(3).

DeWitt, R. N. (1962), The Occurrence of Aurora in Geomagnetically Conjugate Areas, *Journal of Geophysical Research*, *67*(4).

Dungey, J. W. (1961), Interplanetary magnetic Field and the Auroral Zones, *American Physical Society Journals*, *6*(2), Pysical Research Letter.

Emmert, J. T., A. D. Richmond, and D. P. Drob (2010), A computationally compact representation of Magnetic-Apex and Quasi-Dipole coordinates with smooth base vectors, *Journal of Geophysical Research*, *115*(A8), A08,322, doi:10.1029/2010JA015326.

Finlay, C. C., et al. (2010), International Geomagnetic Reference Field: the eleventh generation, *Geophysical Journal International*, *183*(3), 1216–1230, doi:10.1111/j.1365-246X.2010.04804.x.

Förster, M., S. E. Haaland, G. Paschmann, J. M. Quinn, R. B. Torbert, H. Vaith, C. A. Kletzing, and I. City (2008), High-latitude plasma convection during Northward IMF as derived from in-situ magnetospheric Cluster EDI measurements, *Annales Geophysicae*, *26*, 2685–2700.

Frank, L. A., and J. B. Sigwarth (2000), Findings concerning the positions of substorm onsets with auroral images from the Polar spacecraft, *Journal of Geophysical Research*, *105*(A6), 12,747–12,761.

Frank, L. A., and J. B. Sigwarth (2003), Simultaneous images of the northern and southern auroras from the Polar spacecraft: An auroral substorm, *Journal of Geophysical Research*, *108*(A4), 8015, doi:10.1029/2002JA009356.

Frank, L. A., J. B. Sigwarth, J. D. Craven, J. E. Cravens, J. S. Dolan, M. R. Dvorsky, P. K. Hardebeck, J. D. Harvey, and D. W. Muller (1995), The Visible Imaging System (VIS) For The Polar Spacecraft, *Space Science Reviews*, *71*, 297–328.

Frey, H. (2010), http://sprg.ssl.berkeley.edu/sprite/ago96/image/wic_summary/0_fuv_operations.log, *FUV Operations LOG-file*.

Frey, H. U., and S. B. Mende (2006), Substorm onsets as observed by IMAGE-FUV, *Proc. 8th Int. Conf. Substorms (ICS-8)*, pp. 71–75.

Frey, H. U., S. Mende, C. Carlson, J.-C. Gerard, B. Hubert, J. Spann, R. Gladstone, and T. Immel (2001), The electron and proton aurora as seen by IMAGE-FUV and FAST, *Geophysical Research Letters*, *28*(6), 1135–1138.

Frey, H. U., et al. (2003), Summary of quantitative interpretation of image far ultraviolet auroral data, *Space Science Reviews*, *109*, 255–283.

Friis-Christensen, E., Y. Kamide, A. D. Richmond, and S. Matsushita (1985), Interplanetary magnetic field control of high-latitude electric fields and currents determined from Greenland Magnetometer Data, *Journal of Geophysical Research*, *90*(A2), 1325–1338.

Fukushima, N. (1976), Generalized theorem for no ground magnetic effect of vertical currents connected with Pedersen currents in the uniform-conductivity ionosphere, *Report Ionosphere Space Research Japan*, *30*, 35–50.

Fukushima, N. (1994), Some topics and historical episodes in geomagnetism and aeronomy, *Journal of Geophysical Research*, *99*(A10), 19,113–19,142.

Fukushima, N., and Y. Kamide (1973a), Contribution of magnetospheric field-aligned current to geomagnetic bays and Sq fields: A comment on partial ring-current models, *Radio Science*, *8*(11), 1013–1017.

Fukushima, N., and Y. Kamide (1973b), Partial Ring Current Models for Worldwide Geomagnetic Disturbances, *Reviews of geophysics and space physics*, *11*(4), 795–853.

Gjerloev, J. W. (2009), A Global Ground- Based Magnetometer Initiative, *EOS Transactions*, *90*(27), 230–331, doi:10.1029/2008GL035176.Ripepe.

Gjerloev, J. W. (2012), The SuperMAG data processing technique, *Journal of Geophysical Research*, *117*(A9), A09,213, doi:10.1029/2012JA017683.

Gjerloev, J. W., and R. a. Hoffman (2014), The large-scale current system during auroral substorms, *Journal of Geophysical Research Space Physics*, *119*, 4591–4606, doi:10.1002/2013JA019176.Received.

Gonzalez, W., J. Joselyn, Y. Kamide, H. W. Kroehl, G. Rostoker, B. T. Tsurutani, and V. M. Vasyliunas (1994), What is a geomagnetic storm?, *Journal of Geophysical Research*, *99*(A4), 5771–5792.

Guo, J., H. Liu, X. Feng, T. I. Pulkkinen, E. I. Tanskanen, C. Liu, D. Zhong, and Y. Wang (2014), MLT and seasonal dependence of auroral electrojets: IMAGE magnetometer network observations, *Journal of Geophysical Research*, *119*, 3179–3188, doi:10.1002/2014JA019843.Received.

Haaland, S., et al. (1999), Magnetospheric and ionospheric response to a substorm: Geotail HEP-LD and Polar PIXIE observations, *Journal of Geophysical Research*, *104*(A12), 28,459.

Haaland, S. E., G. Paschmann, M. Förster, J. M. Quinn, R. B. Torbert, C. McMIlwain, H. Vaith, P. Phul-Quinn, and C. A. Kletzing (2007), High-latitude plasma convection from Cluster EDI measurements: method and IMF-dependence, *Annales Geophysicae*, *25*, 239–253.

Iijima, T. (2000), Field-aligned currents in geospace: Substance and significance, *Geophysical Monograph*, *118*.

Iijima, T., and T. A. Potemra (1978), Large-scale characteristics of field-aligned currents associated with substorms, *Journal of Geophysical Research*, *83*(A2), 599–615.

Iyemori, T. (1990), Storm-time Magnetospheric Currents Inferred from Mid-latitude Geomagnetic Field Variations, *Journal of geomagnetism and geoelectricity*, *42*, 1249–1265.

Kamide, Y., and S. Kokubun (1996), Two-component auroral electrojet: Importance for substorm studies, *Journal of Geophysical Research*, *101*(A6), 13,027 – 13,046.

Kamide, Y., A. D. Richmond, and S. Matsushita (1981), Estimation of ionospheric electric fields, ionospheric currents, and field-aligned currents from ground magnetic records, *Journal of Geophysical Research*, *86*(A2), 801–813.

Kamide, Y., W. Sun, and S. Akasofu (1996), The average ionospheric electrodynamics for the different substorm phases, *Journal of Geophysical Research*, *101*(A1), 99–109.

Kaufmann, R. (1987), Substorm currents: Growth phase and onset, *Journal of Geophysical Research*, *92*(A7), 7471–7486.

Kelley, M. C. (2009), *The Earth's Ionosphere: Plasma physics and electro dynamics*, 2 ed., Academic Press.

King, J. H., and N. E. Papitashvili (2005), Solar wind spatial scales in and comparisons of hourly Wind and ACE plasma and magnetic field data, *Journal of Geophysical Research*, *110*(A2), A02,104, doi:10.1029/2004JA010649.

Kivelson, M., and C. T. Russel (1996), *Intoduction to Space Physics*, Cambridge University Press, Los Angeles.

Korth, H. (2014), ampere.jhuapl.edu/code/idl_geopack.html, *IDL GEOPACK DLM*.

Kramer, H. J. (2002), AMPERE - Active Magnetosphere and Planetary Electrodynamics Response Experiment,https://directory.eoportal.org/web/eoportal/satellite-missions/a/ampere.

Laundal, K. M. (2010), Auroral Imaging as a Tracer of Global Magnetospheric Dynamics, Ph.D. thesis, University of Bergen, Norway.

Laundal, K. M., and J. W. Gjerloev (2014), What is the appropriate coordinate system for magnetometer data when analyzing ionospheric currents?, *Journal of Geophysical Research Space Physics*, *119*, 8637–8647, doi:10.1002/2014JA020484. Received.

Laundal, K. M., and N. Østgaard (2009), Asymmetric auroral intensities in the Earth's Northern and Southern hemispheres, *Nature*, *460*(7254), 491–493, doi:10.1038/nature08154.

Laundal, K. M., N. Østgaard, K. Snekvik, and H. U. Frey (2010), Interhemispheric observations of emerging polar cap asymmetries, *Journal of Geophysical Research*, *115*(A7), A07,230, doi:10.1029/2009JA015160.

Lui, A. T. (1984), Characteristics of the cross-tail current in the Earth's magnetotail, *Geophysical Monograph Series*, *28*(Magnetospheric Currents), 158.

McPherron, R. L., C. T. Russell, M. G. Kivelson, and P. J. Coleman (1973), Substorms in space: The correlation between ground and satellite observations of the magnetic field, *Radio Science*, *8*(11), 1059–1076.

Mcpherron, R. L., C. Russel, and M. P. Avbry (1973), Satellite Studies of Magnetospheric Substorms on August 15, 1968 9. Phenomenological Model for Substorms, *Journal of Geophysical Research*, *78*(16).

Mende, S. B., et al. (2000a), Far ultraviolet imaging from the image spacecraft. 2. wideband fuv imaging, *Space Science Reviews*, *91*, 271–285.

Mende, S. B., et al. (2000b), Far Ultraviolet Imaging From The IMAGE Spacecraft. 3. Spectral Imaging of Lyman-α and OI 135.6 nm, *Space Science Reviews*, *91*, 287–318.

Mende, S. B., et al. (2000c), Far ultraviolet imaging from the image spacecraft. 1. system design, *Space Science Reviews*, *91*, 243–270.

Nakano, S. (2005), Storm-time field-aligned currents on the nightside inferred from ground-based magnetic data at midlatitudes: Relationships with the interplanetary magnetic field and substorms, *Journal of Geophysical Research*, *110*(A7), A07,216, doi:10.1029/2004JA010737.

Newell, P. T., and J. W. Gjerloev (2011), Evaluation of SuperMAG auroral electrojet indices as indicators of substorms and auroral power, *Journal of Geophysical Research*, *116*(A12), A12,211, doi:10.1029/2011JA016779.

Newell, P. T., and J. W. Gjerloev (2012), SuperMAG-based partial ring current indices, *Journal of Geophysical Research*, *117*(A5), A05,215, doi:10.1029/2012JA017586.

Newell, P. T., C.-I. Meng, and K. M. Lyons (1996), Suppression of discrete aurorae by sunlight, *Nature*, *381*(6585), 766–767.

NOAA (2015), DMSP home page, http://ngdc.noaa.gov/eog/dmsp.html.

Ohtani, S., S. Wing, G. Ueno, and T. Higuchi (2009), Dependence of premidnight field-aligned currents and particle precipitation on solar illumination, *Journal of Geophysical Research*, *114*(A12), A12,205, doi:10.1029/2009JA014115.

Østgaard, N. (2005), Observations and model predictions of substorm auroral asymmetries in the conjugate hemispheres, *Geophysical Research Letters*, *32*(5), L05,111, doi:10.1029/2004GL022166.

Østgaard, N., and K. M. Laundal (2012), Auroral Phenomenology and Magnetospheric Processes : Earth and Other Planets, *Geophysical Monograph Series*, *197*, 99–111.

Østgaard, N., S. Mende, H. U. Frey, T. Immel, L. A. Frank, J. Sigwarth, and T. Stubbs (2004), Interplanetary magnetic field control of the location of substorm onset and auroral features in the conjugate hemispheres, *Journal of Geophysical Research*, *109*(A7), A07,204, doi:10.1029/2003JA010370.

Østgaard, N., S. Mende, H. Frey, J. Sigwarth, A. Åsnes, and J. Weygand (2007), Auroral conjugacy studies based on global imaging, *Journal of Atmospheric and Solar-Terrestrial Physics*, *69*(3), 249–255, doi:10.1016/j.jastp.2006.05.026.

Parker, E. (2007), *Conversations on Electric and Magnetic Fields in the Cosmos*, Princeton University Press, Princeton.

Potemra, T. A. (1985), Field Aligned (Birkeland) Currents, *Space Science Reviews*, *42*, 295–311.

Pulkkinen, T. I., D. N. Baker, R. J. Pellinen, J. S. Murphree, and L. A. Frank (1995), Mapping of the auroral oval and individual arcs during substorms, *Journal of Geophysical Research*, *100*(A11), 21,987–21,994.

Reistad, J. P. (2012), Non-Conjugate Aurora and Interhemispheric Currents, Master's thesis, University og Bergen, Norway.

Reistad, J. P., N. Østgaard, K. M. Laundal, and K. Oksavik (2013), On the non-conjugacy of nightside aurora and their generator mechanisms, *Journal of Geophysical Research: Space Physics*, *118*(6), 3394–3406, doi:10.1002/jgra.50300.

Reistad, J. P., N. Østgaard, K. M. Laundal, S. Haaland, P. Tenfjord, K. Snekvik, K. Oksavik, and S. E. Milan (2014), Intensity asymmetries in the dusk sector of the poleward auroral oval due to IMF Bx, *Journal of Geophysical Research*, *119*, doi:10.1002/2014JA020216.Received.

Richmond, a. D. (1995), Ionospheric Electrodynamics Using Magnetic Apex Coordinates., *Journal of geomagnetism and geoelectricity*, *47*(2), 191–212, doi:10.5636/jgg.47.191.

Rostoker, G., S. Akasofu, J. Foster, R. A. Greenwald, Y. Kamide, K. Kawasaki, A. T. Y. Lui, R. L. Mcpherron, and C. T. Russell (1980), Magnetospheric substorms; definition and signatures, *Journal of Geophysical Research*, *85*(A4), 1663–1668.

Russel, C. (1986), Solar Wind Control of Magnetosperic Configuration, *Solar Wind-Magnetospheric Coupling*.

Sato, N., T. Nagaoka, K. Hashimoto, and T. Saemundsson (1998), Conjugacy of isolated auroral arcs and nonconjugate auroral breakups, *Journal of Geophysical Research*, *103*(A6), 641–652.

Smith, C. W., J. L'Heureux, N. Ness, M. H. Acuña, L. Burlaga, and J. Scheifele (1998), The ACE magnetic fields experiment, *Space Science Reviews*, *86*, 613–632.

Song, P., and V. M. Vasyliunas (2011), How Is the Ionosphere Driven by the Magnetosphere?, *IEEE Transactions on Magnetics*, *11*, 1–4.

Sonnerup, B. U. O. (1974), Magnetopause reconnection rate, *Journal of Geophysical Research*, *79*(10).

Stenbaek-Nielsen, H. C., and A. Otto (1997), Conjugate auroras and the interplanetary magnetic field, *Journal of Geophysical Research*, *102*(A2), 2223–2232.

Stenbaek-Nielsen, H. C., T. N. Davis, and N. W. Glass (1972), Relative Motion of Auroral Conjugate Points during Substorms, *Journal of Geophysical Research*, *77*(10), 1844–1858.

Stone, E. C., A. M. Frandsen, and R. A. Mewaldt (1998), The advanced composition explorer, *Space Science Reviews*, *86*, 1–22.

Strangeway, R. J. (2009), Space Environment and Scientific Missions: Magnetic Fields in Space, *IEEE transactions on magnetics*, *45*(10), 4486–4492.

Strangeway, R. J., and J. Raeder (2001), On the transition from collisionless to collisional magnetohydrodynamics, *Journal of Geophysical Research*, *106*(A2), 1955–1960, doi:10.1029/2000JA900116.

Sugiura, M. (1964), Dst index 1957-1986, *Annales of the International Geophysics Year 35*, *9*.

Sugiura, M., and T. A. Potemra (1976), Net field-aligned currents observed by Triad, *Journal of Geophysical Research*, *81*(13).

Sun, W., B. Ahn, S. Akasofu, and Y. Kamide (1984), A comparison of the observed mid-latitude magnetic disturbance fields with those reproduced from the high-latitude modeling current system, *Journal of Geophysical Research*, *89*(A12), 10,881–10,889.

Sun, W., L. C. Lee, Y. Kamide, and S. Akasofu (1985), An improvement of the Kamide-Richmond-Matsushita Scheme for the estimation of the three-dimensional current system, *Journal of Geophysical Research*, *90*(A7), 6469–6474.

Tsyganenko, N. (2014), geo.phys.spbu.ru/~tsyganenko/modeling.html, *GEOPACK*.

VanZandt, T., W. L. Clark, and J. Warnock (1972), Magnetic Apex Coordinates: A Magnetic Coordinate System for the Ionospheric F2 Layer, *Journal of Geophysical Research*, *77*(13).

Vasyliunas, V. M. (2005), Relation Between magnetic fields and electric currents in plasma, *Annales Geophysicae*, *23*(7), 2589–2597.

Vasyliunas, V. M. (2007), The mechanical advantage of the magnetosphere: solar-wind-related forces in the magnetosphere-ionosphere-Earth system, *Annales Geophysicae*, *25*, 255–269.

Vasyliunas, V. M., and P. Song (2005), Meaning of ionospheric Joule heating, *Journal of Geophysical Research*, *110*(A2), A02,301, doi:10.1029/2004JA010615.

Wanliss, J. (2005), Fractal properties of SYM-H during quiet and active times, *Journal of Geophysical Research*, *110*(A3), A03,202, doi:10.1029/2004JA010544.

Wanliss, J. a., and K. M. Showalter (2006), High-resolution global storm index: Dst versus SYM-H, *Journal of Geophysical Research*, *111*(A2), A02,202, doi:10.1029/2005JA011034.

Weimer, D. R. (2003), Predicting interplanetary magnetic field (IMF) propagation delay times using the minimum variance technique, *Journal of Geophysical Research*, *108*(A1), 1026, doi:10.1029/2002JA009405.

Weimer, D. R. (2005), Improved ionospheric electrodynamic models and application to calculating Joule heating rates, *Journal of Geophysical Research*, *110*(A5), A05,306, doi:10.1029/2004JA010884.

Weimer, D. R., C. R. Clauer, M. J. Engebretson, T. L. Hansen, H. Gleisner, I. Mann, and K. Yumoto (2010), Statistical maps of geomagnetic pertubations as a function of the interplanetary magnetic field, *Journal of Geophysical Research*, *115*(10).

Wing, S., P. T. Newell, D. G. Sibeck, and K. B. Baker (1995), A Large Statistical Study of the Entry of Interplanetary Magnetic Field Y-Component Into the Magnetosphere, *Geophysical Research Letters*, *22*(16), 2083–2086.

Zmuda, A. J., and J. C. Armstrong (1974a), The diurnal flow pattern of field-aligned currents, *Journal of Geophysical Research*, *79*(31), 4611–4619.

Zmuda, A. J., and J. C. Armstrong (1974b), The diurnal variation of the region with vector magnetic field changes associated with field-aligned currents, *Journal of Geophysical Research*, *79*(16), 1–2.

Zmuda, A. J., F. Heuring, and J. Martin (1967), Dayside Magnetic Disturbances at 1100 Kilometers in the Auroral Oval, *Journal of Geophysical Research*, *72*(3), 1115–1117.